ROTOR ICE SHEDDING AND TRAJECTORY ANALYSES IN HOVER AND FORWARD FLIGHT

Morris Julian Anthony

Department of Mechanical Engineering

McGill University

Montreal, Quebec

August 2018

A thesis submitted to McGill University in partial fulfillment of the requirements of the degree of Master of Engineering

Abstract

In-flight ice accretion on aircraft surfaces pose extremely dangerous conditions to operate in. The decline in stall angle, increase in drag and ingestion of shed-ice can result in incidents and fatal accidents. Lately, numerical methods have been developed to predict ice formation on aircraft wings which assist in the design of Ice Protection Systems (IPS). However, rotorcraft ice accretion simulation techniques lag far behind. For example, to the author's knowledge, a complete ice trajectory analysis for rotorcraft applications have not been conducted prior to this.

For rotorcraft, while the high centrifugal forces on the blades may serve as a natural de-icing mechanism, it could also lead to uneven ice shedding, causing rotor imbalances and vibrations. Ice shedding from a rotor blade can also result in ice hitting other blades, the fuselage or tail rotor, with a significant impact on the structural integrity of a helicopter. Therefore, the simulation of ice shedding and subsequent ice trajectories are important.

This thesis provides a comprehensive review of existing ice shedding and trajectory techniques and proposes a methodology to determine ice shed location, time of shed and impact zones. A trajectory procedure involving 3-D stitching and Reduced Order Modeling CFD techniques is developed, and applied to hover and forward flight test cases

The goal of this thesis is to develop a computationally inexpensive system to determine ice shedding time and location and analyze the possible areas of impact in hover and forward flight.

Résumé

Le cumul de glace en vol sur les surfaces d'avions pose des conditions extrêmement dangereuses. La diminution de l'angle de décrochage, l'augmentation de la traînée et l'ingestion de glace peuvent causer des incidents ainsi que des accidents mortels. Des méthodes de simulation numérique ont été mises au point récemment pour prévoir la formation de glace sur les ailes des aéronefs, ce qui facilite la conception des systèmes d'antigivrage. Cependant, les simulations d'accrétion de glace sur les hélicoptères trainent de l'arrière. Par exemple, aux meilleures connaissances de l'auteur, une méthode complète d'analyse de la trajectoire des blocs de glace pour les applications d'hélicoptères n'existe pas.

Pour les hélicoptères, alors que les forces centrifuges sur les pales sont en quelque sorte un mécanisme de dégivrage naturel, elles peuvent également entraîner une formation de glace inégale, causant des déséquilibres de rotor et des vibrations. Le délestage de glace à partir d'une pale de rotor peut soit frapper d'autres pales, le fuselage ou le rotor de queue, affectant l'intégrité structurelle d'un hélicoptère. Par conséquent, la simulation de délestage de glace et des trajectoires subséquentes est importante pour éviter tout endommagement.

Cette thèse passe en revue les techniques existantes de délestage de glace et de trajectoires et propose une méthodologie pour déterminer la zone et l'instant de délestage ainsi que les points d'impact. Le calcul de trajectoires est effectué sur un maillage à zones multiples (dit stitching) en utilisant des modèles de CFD à ordre réduit (dites Reduced Order Modeling) et est appliqué au cas de vol et de planage.

Le but de cette thèse est de développer un système efficace pour déterminer la zone et l'instant de délestage de glace, et d'analyser les zones possibles d'impact en vol et en vol planage.

Acknowledgments

Firstly, I would like to express my immense gratitude to my primary thesis supervisor, Professor Wagdi G. Habashi for his mentorship. This project would not have been possible without his devotion to the McGill Computational Fluid Dynamics Laboratory (McGill CFD Lab). His years of experience together with his passion, have provided me with a vast amount of knowledge in the aero-icing field and has taught me valuable traits which would be very beneficial in my career. It has been an honour to work under his supervision on this extremely challenging and fulfilling project.

I would also like to acknowledge my secondary thesis supervisor, Dr. Marco Fossati. He created the foundation for this project and his initial direction was incredibly valuable. His encouragement and assistance in all projects have been important factors in the advancement of research at the McGill CFD Lab.

It has been extremely pleasant working with everyone at the CFD Lab. I would like to especially extend my appreciation to Dr. Zhao Zhan and Dr. Ahmed Bakkar, post doctorate fellows during my time at the CFD Lab. Their expertise in the field along with their strong problem-solving skills have helped me unravel major issues faced during the research conducted. Furthermore, I would like to thank Munir Nathoo and Maged Yassin, colleagues at the CFD Lab, for their collaborative efforts in my project.

I also wish to thank Dr. Guido Baruzzi, Dr. Habib Fouladi and Mr. Shezad Nilamdeen for their insight during the development phase of my research project. Their advice helped save massive amounts of time. The financial support for this project has been crucial. For that, I would like to extend my appreciation to Natural Sciences and Engineering Research Council of Canada (NSERC) / Lockheed Martin / Bell Helicopter Research Chair for Multi-Disciplinary Analysis and Design of Aerospace Systems. The computational resources provided by CLUMEQ and Calcul Quebec were vital in completing this project in a timely manner, which I am very thankful for.

Finally, I would like to express thanks to my family and friends for their continuous support and provision of encouragement throughout my studies. Their emotional care has been a tremendously important part of this journey.

Dedication

I dedicate this thesis to my parents, who have provided me with emotional, financial support and unconditional love on all aspects of my life. I am forever grateful. Thank you.

List of Figures

List of Tables

Table of Contents

1 Introduction

1.1 Background

In-flight icing takes place when supercooled water droplets freeze on impact with the structure of an aircraft or rotorcraft. This can lead to adverse aerodynamic effects, blockage of Pitot tubes and static vents, radio communication problems and ice shedding hazards [1]. Figure 1-1 illustrates an example of ice buildup on an aircraft wing.

Figure 1-1 – Ice buildup on an aircraft wing

The presence of ice on a lifting surface such as an aircraft wing, helicopter blades or propeller blades can significantly alter the airflow patterns. As a result, the airplane experiences a loss in lift, rise in drag and a helicopter loses thrust and undergoes a torque rise. The schematic represented by Figure 1-2 highlights this difference in flow pattern between a clean and an iced wing, which could eventually lead to detrimental effects.

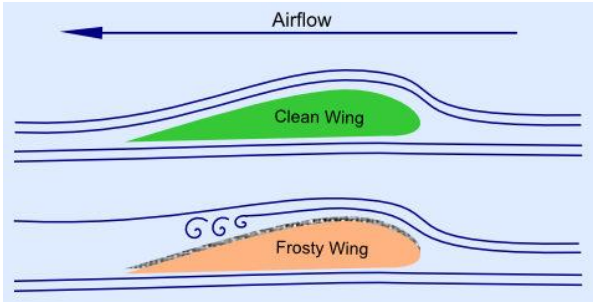

Figure 1-2 – Schematic of variation of flow pattern between a clean and iced wing

In the case of a rotorcraft, the high centrifugal forces experienced on a rotor blade may serve as a natural de-icing mechanism [2]. However, this may lead to uneven ice shedding, and consequently can cause rotor imbalances and severe vibrations of the fuselage. This is

represented by Figure 1-3 which illustrates an iced blade with a segment of ice shed near the tip, leaving behind another section of ice.

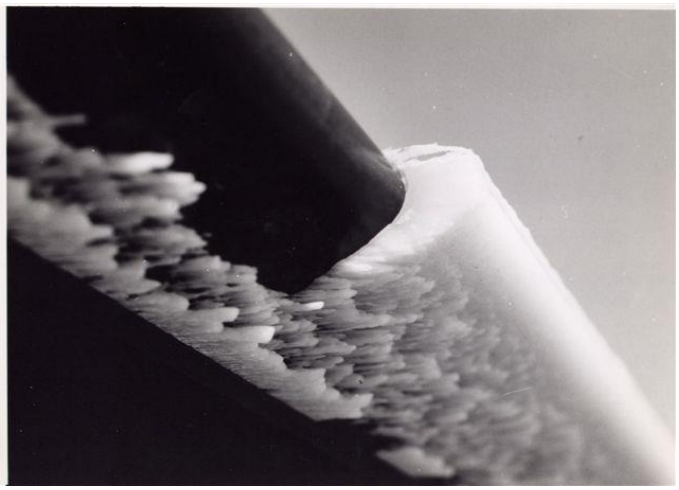

Figure 1-3 – Ice shed from helicopter rotor tip, leaving behind a section of ice

Ice shedding from rotorcraft is governed by the interaction of multiple forces that impose stresses within the ice and between the metal-ice interface. Subsequently, these affect ice-ice bonding and metal-ice bonding and are known as Cohesive Tensile stresses and Adhesive Shear stresses, respectively. The forces that contribute to the development of these stresses are:

- The bending of the blade due to aerodynamic forces and structural vibrations
- Aerodynamic pressure forces acting on the ice directly
- Centrifugal forces due to the high rotational speed of rotors
- Thermal stresses because of the phase changes in the accreted ice

The interaction of these forces determines the shape of ice that is eventually shed. Several approaches have been identified to compute the resulting shed-ice piece. These include very detailed, computationally expensive, frameworks such as finite element analyses involving crack propagation routines to less detailed, quicker approaches such as sectional forces analyses.

The subsequent ice trajectories, whether from rotorcraft or from aircraft, are dictated by the shed-ice shape and the interaction of the ice piece with the flow field. Depending on the configuration of the rotorcraft, ice shed from the blades may also result in ice hitting other blades, the fuselage or the tail rotor. Hence, ice trajectories prediction is important, to prevent damage to the rotorcraft due to the impact energies of shed-ice pieces. Similar to ice shedding, researchers have also modelled trajectories with varying levels of complexities. Methods

involving one-way interaction, coupled with a Monte Carlo approach, have been investigated for fixed wing applications. This looks at the effect of the flow field on the trajectory of the ice piece, but not on the effect of the ice piece on the flow. On the other hand, computationally intensive two-way interaction frameworks have also been studied, taking into account the interactive effect of the ice piece with the flow field.

A comprehensive literature review was conducted and is reported in the second chapter of this thesis, with several techniques for ice shedding and trajectories being discussed. Chapter 3 details the proposed methodology to model the phenomena. It also briefly discusses the 3-D stitching methodology used to provide the iced blade and rotor flow field for ice shedding and trajectory analyses. Validation and test case results are presented in chapter 4, for hover and forward flight. Finally, this thesis is completed with a conclusions section.

1.2 Contributions

The following were produced as a result of this thesis:

- AERTS model rotor was meshed for aero-icing simulations and can be re-used for other projects.
- An ice shedding methodology including aerodynamic force calculation was developed and validated.
- An ice trajectory routine based on Reduced Order Modelling (ROM), capable of conducting multiple trajectories with various ice shapes has been produced.
- Rectangular plate and semi-circular ice pieces meshes were created and their respective databases generated to model ice trajectories. Databases for arbitrary shapes can from this point on easily be added and modelled.
- Post-processing codes have been developed to visualize trajectories relative to a specific helicopter.

2 Literature Review

2.1 Ice shedding techniques

Zhang and Habashi [3] developed 2D and 3D Finite Element flow and structural analyses of ice breakup on wings and rotors. The 2-D flow solution, the clean grid and the iced grid were utilized for the 2-D analysis. Each node of the clean grid had a corresponding node in the iced grid. The ice shape was determined by evaluating the difference in positions of every node in the two grids. The pressure from the flow solution was then extracted and applied as the only force on the extracted ice shape. A 2D crack propagation package was developed from which the shape of the shed-ice piece was computed. A similar process was used to extract the 3D shape of ice from a helicopter blade. Here, the net aerodynamic force was assumed to be negligible compared to the centrifugal force. At each crack propagation step, the principal and von Mises stresses were computed. The interface between the ice and blade delaminated if either of the stresses exceeded a critical value. During this process, if the maximum principal stress in the ice reached a critical value (cohesive strength) then a crack was initiated. At this point, a tiny 3D crack was inserted into the ice perpendicular to the principal stress. A 3D algorithm was then used to follow the crack propagation. Once the crack tips reached both sides of the ice shape, the shed-ice shape became evident. This is a very detailed and relatively expensive method in comparison to the subsequent methods. A more straightforward approach that results in a reasonably accurate prediction of the crack location is still needed.

Bennani, Villedieu and Salaun [4] discussed the governing equations behind the anti-icing/de-icing modelling numerical tool (MAD/now renamed to INUIT) in one of their papers. This was an addition to the ONERA class of icing codes. The code simulated the functionality of an electro-thermal de-icing system. The adhesion model used was based on continuum damage mechanics. Experimental values describing the elastic properties of natural ice were used and assumed initially to be independent of temperature. The ice adhesion model that was first implemented in MAD was empirical and stated that if the ratio between water film length and total ice block length became greater than a user-defined value (80% was recommended), then the ice was shed. A variant of this based on water film height was also implemented. The motivation behind the linear elastic damage model used was the following: when a solid is

deformed by action of external forces it internally stores elastic deformation energy. If, locally, this energy exceeds a certain critical energy, it will lead to an increase in crack surface. Therefore, if a crack nucleates and/or propagates, a possible mechanism (from a macroscopic point of view) could be a process of energy transfer from the applied forces, to elastic deformation energy, to crack surface energy. The sequence in which the ice shedding analysis was performed was as follows: a flow field and an ice shape were obtained from the flow and ice solvers, respectively. A part of the ice at the leading edge was suppressed to imitate a parting strip. Thermal computations were then performed to determine the melted regions of the ice/surface interface. Aerodynamic loads were then applied, and the crack propagation predicted using the linear elastic damage model. This methodology was only applied to aircraft, as only the adhesion and aerodynamic loads were evaluated.

Scavuzzo, Chu and Kellackey [5] presented a simplified method to Zhang and Habashi's [3] work, coupled with a statistical analysis. A uniform layer of ice was added to the inside of a rotating aluminum beam. Therefore, the ice was of constant thickness and height along the blade. The ice and the blade were modeled using 8-node elements, and a finite element analysis was carried out by imposing a centrifugal force on the ice. It was assumed that shear and tensile stresses act simultaneously as a result. Cracks of different lengths were imposed near the tips, and the shear and tensile stress distributions were studied. Next, given a shear stress distribution for an ice profile, a normal distribution for the calculated shear stress values, along with a Weibull distribution for the shear strength distribution, were used. Ice shedding was then determined as a probability that depended on the difference between the shear strength and the shear stress due to the centrifugal force. Since this method used a statistical distribution for the shear stress distribution and assumed a uniform thickness of ice accumulated on the blade, it does not simulate the real-life situation. Furthermore, this approach used a similar methodology to Zhang's work in terms of computing the stresses using a finite element analysis, hence was not further considered.

Brouwers, Palacios, Peterson, and Smith [6] developed the AERTS Rotor Icing, Shedding and Performance (ARISP) model. Here, a sectional approach was taken to calculate rotor performance and ice accretion at various stations along the blade. The rotor performance was

calculated via a Blade Element Momentum Theory (BEMT) routine. This was integrated with LEWICE to determine the ice accretion on a rotor blade. At sections of the rotor blade, the centrifugal, shear and cohesive forces of the sectional ice were determined. The aerodynamic forces were approximated to be around 20% of the centrifugal forces and were neglected for simplicity. This methodology proved to be computationally inexpensive and therefore met the objective of the approach required for this project.

As seen in the above methods, researchers generally assume that aerodynamic forces are negligible relative to the high centrifugal forces experienced by rotorcraft blades. Scavuzzo, Chu, and Ananthaswamy [7] looked at the significance of modelling aerodynamic forces during ice shedding. A 2-D Navier-Stokes solver was used to obtain the flow field data around an airfoil. This was then used to calculate the pressure coefficients which were correlated with experimental measurements and were found to be in good agreement. The pressure coefficients were then used to calculate the pressure field around the airfoil by:

$$P = \frac{1}{2}\rho V^2 C_P \tag{2-1}$$

It was found that the stresses produced at Mach numbers below 0.45 were not significant enough to contribute to shedding. However, higher Mach numbers and higher angles of attack resulted in significant stresses due to aerodynamic loading and it was concluded that it should be considered for ice shedding.

Following the thorough literature review done on the ice shedding methodologies, it was concluded that a similar approach to [6] proved to be ideal. The importance of modelling aerodynamic forces was demonstrated in [7] and it was considered as a vital force to be modelled in this thesis. In addition, a fully 3-D approach was used to accrete the ice, as opposed to the quasi-3D method used by Brouwers et al.

2.2 Ice trajectory techniques

Beaugendre, Morency, Gallizio, and Laurens [8] proposed a vortex method to predict the interaction of an incompressible flow with rigid bodies. Hybrid vortex methods were used to simulate unsteady incompressible viscous flows. These methods are based on a combination of Lagrangian mesh-free schemes and Eulerian grid-based schemes. The Navier-Stokes equations were recast in terms of a vortex formulation. A particle discretization was used to calculate the vortex field. Here, a Lagrangian scheme was used to solve the nonlinear advective part, whereas an Eulerian scheme was used to solve the diffusive part and the velocity term. A penalization was then used to enforce the no-slip boundary condition inside the solid wall boundaries, and level set functions were used to track interfaces and calculate the rigid motions of the solid bodies. Considering that a flow solver has already been developed by the authors' group, this method seemed very complex and computationally expensive. A simpler, more straightforward approach was preferred.

Baruzzi, Lagacé, Aubé and Habashi [9] presented a shed-ice trajectory methodology that used a hole cutting and stitching method. This method consisted of a stationary mesh and a moving mesh. Initially holes were created in the stationary domain to remove any overlapping portion of it from the moving domain. The moving mesh was then translated and rotated according to the integration of the Newton and Euler equations. Finally, the gap between the two domains were bridged using a stitching algorithm, creating a single continuous unstructured hybrid mesh and thus eliminated the need to interpolate between domains. As a result, fluxes were ensured to be fully conserved across the entire grid. An efficient parallel iterative matrix solver and a domain decomposition method was utilized to partition the computational domain into equal-sized domains. This method is computationally intensive even though it represents the most accurate image of the phenomenon. Hence, a computationally cheaper method, with reasonable accuracy, was sought after in the current thesis.

Khurram and Minhas [10] studied the effects of ice impact on the helicopter body and other materials such as the human skull. To perform this analysis, an ice trajectory model was implemented. Firstly, FENSAP-ICE was used as the simulation package for ice accretion. The Caradonna hover test case [11] was then used to obtain the flow solution for helicopter blades.

The ice breakup analysis solution was then used from Zhang's work [3] to acquire a cracked ice shape. Only the drag force, momentum of the ice piece and the gravity effects on the particle were considered. Since the point of impact was not considered as the most important aspect of analysis, a simple 1-D ice trajectory model was used, making the method extremely inexact for a complex flow field such as that of a helicopter.

Yapalparvi, Beaugendre and Morency [12] implemented the method of Proper Orthogonal Decomposition (POD) to compute ice piece trajectories. Initially, snapshots of varying density ratios of the ice piece to the ambient fluid were obtained. This was accomplished by solving the unsteady incompressible Navier-Stokes equations on Cartesian grids involving penalization and level set methods. POD was then used to interpolate for cases in which the density ratios were not computed using the solver. This analysis was performed on two test cases – iced airfoil and iced cylinder and showed remarkable agreement. The error norms were also shown to be in the order of O (10^{-5}) and a significant decrease in computation time was recorded.

Kohlman and Winn [13] simulated ice trajectories in a uniform flow field from an aircraft using square plates. The initial orientation, width and thickness of these plates were varied to obtain a probabilistic map of high areas of impact. A 4-DOF model was used where the linear displacements in the x, y and z directions were computed. The pitch angle was also calculated to consider the angular displacements of the plate as it traversed through a uniform velocity field. These were calculated by obtaining the lift and drag coefficients and pitching moments which were represented as functions of angle of attack. A similar method to Kohlman and Winn was proposed by Santos, Papa, and Ferrari [14]. However, this time, ice particles were released into a non-uniform flow field. Square shaped flat plates were released from the leading edge with varying initial positions and velocities to study the highly likely areas of ice impact. Papadakis, Yeong and Suares [15] also studied the trajectories of shed-ice particles from aircraft surfaces using a similar approach. The aerodynamic characteristics were obtained experimentally from wind tunnel tests and a trajectory analysis was performed using a 6-DOF model. Trajectories of two ice shapes were studied: a flat plate and a glaze ice horn. These two ice pieces were simulated to be shed from various locations of the wing and fuselage, different initial orientations and at different angles of attack of the aircraft. With these varying parameters, a Monte Carlo

analysis was done to produce probability maps of trajectories at the engine inlet plane of business aircrafts. The method proposed by the three groups proved to be computationally fast, easily parallelizable and considered the aerodynamics effects of the relevant shape of ice. However, it does not account for the effect of the ice piece on the flow field which was assumed to be minimal. The 4-DOF model appears to be suitable for trajectories in a fixed wing flow field as the effects are predominately about one axis. However, this is not the case in a rotor flow field where significant effects are seen about all three axes. Therefore, the 6-DOF model is the only valid model for this case. Hence, a similar framework was developed in this thesis with, however, important variances which are highlighted in the proposed methodology for ice trajectory section.

3 Methodology

3.1 Ice accretion approach

This thesis utilized FENSAP-ICE coupled with a mesh manipulation technique to conduct aero-icing calculations on a rotor. The FENSAP-ICE sequence can be summarized through Figure 3-1.

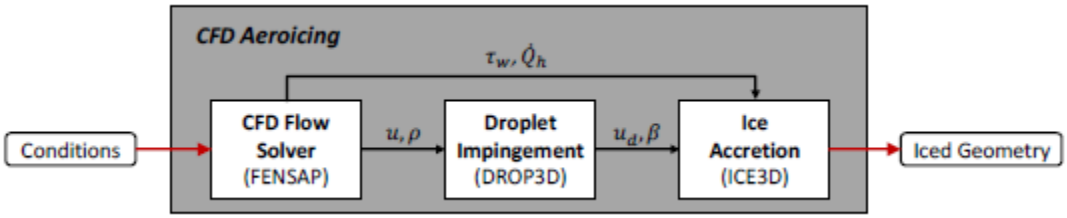

Figure 3-1 – FENSAP-ICE analysis sequence (Figure obtained from *[16]*)

Firstly, the Finite Element Navier-Stokes solver (FENSAP) was used to obtain the flow field around a body. Steady and unsteady compressible flows were solved with turbulence via Reynolds-Averaged Navier Stokes (RANS) models. In this case, the Spalart-Allmaras turbulence model was used.

DROP3D uses an Eulerian framework to calculate the motion of water droplets due to airflow. Fine-grain partial differential equations (PDEs) were solved to obtain particle velocity and water concentration [17]. This resulted in catch efficiency distributions, water concentration, droplet velocity, impingement and shadow zones for a body. A thin liquid film was used to describe surface contamination due to droplet impingement. A so-called Shallow Water Icing Model (SWIM) was applied to consider the path of the water film driven by aerodynamic shear stress [18]. Finally, ICE3D conducted a multi-phase thermal analysis consisting of air, water and ice on the rotor blade surface via conservation laws [19].

A mesh manipulation technique known as the 3-D stitching method, developed at the McGill CFD Lab, was used to handle the altering computational domain for the unsteady numerical simulation of rotorcraft [20]. Initially, two meshes were created: a large stationary mesh describing the surrounding air and a rotating domain consisting of the rotor blades. These two grids were non-overlapping and were separated by empty gap spaces. At every time step of the simulation, these meshes were stitched together with tetrahedral elements via the gap. This technique is also capable of mesh deformation due to rigid and elastic blade motions and ice

accretion. Geometric quality was shown to be conserved through the stitching process and therefore eliminated the need to re-mesh. Since a single grid was created at each time step, the need to interpolate between the domains was removed, therefore improving accuracy for helicopter aerodynamics simulations.

3.2 Ice shedding proposed approach

The iced blade is divided up into elements as shown in Figure 3-2. Starting from the tip, elements are added sequentially inboard, making at every step a "combined" element as illustrated by Figure 3-3. At each step of the analysis, the centrifugal, aerodynamic, critical shear adhesion and critical tensile cohesion forces were evaluated for every combined element. If the summation of the aerodynamic and centrifugal force exceeded the critical cohesion force, then a crack was determined to be formed at that location. That combined element is shed if the summation was greater than the critical adhesion force. The directions of these forces are illustrated in Figure 3-4.

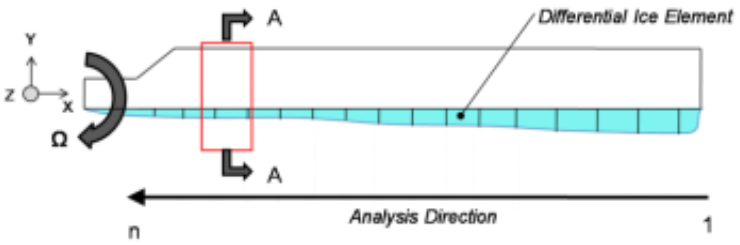

Figure 3-2 – Sectional division of ice accumulated on a rotor blade (Figure obtained from *[6]*)

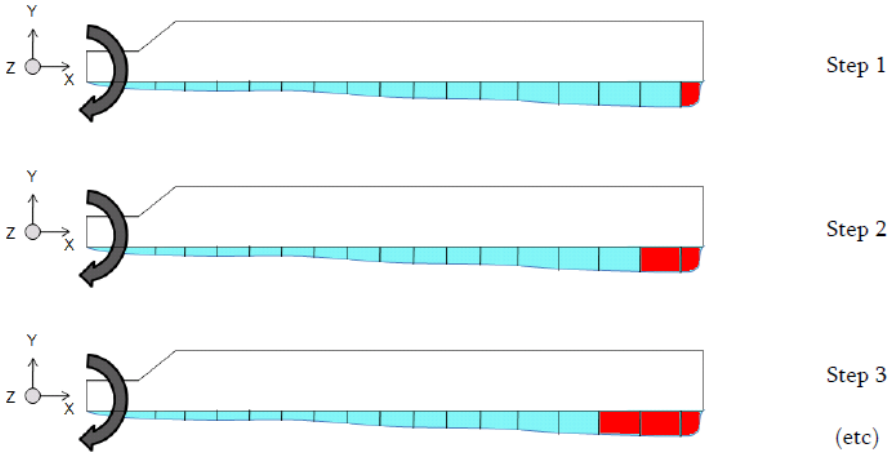

Figure 3-3 – Ice shedding analysis sequence (Figure obtained from *[6]*)

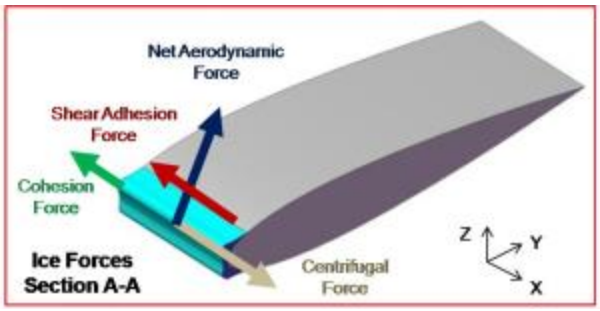

Figure 3-4 – Forces acting on a combined ice element (Figure obtained from *[6]*)

The centrifugal force is generated due to the rotational motion of the blades. The centrifugal force for a differential ice element is calculated by:

$$F_{cent} = m_{ice} r \Omega^2 \tag{3-1}$$

$$m_{ice} = \sum_{elem=1}^{nelem} Growth^{elem} A^{elem} \tag{3-2}$$

The tensile cohesion force, F_C is the force formed due to the tensile stresses experienced by the ice-ice bonds because of the centrifugal forces. This is calculated as follows:

$$F_C = \sigma A_{C_{ice}} \tag{3-3}$$

The tensile strength is temperature dependent and varies according to Figure 3-5.

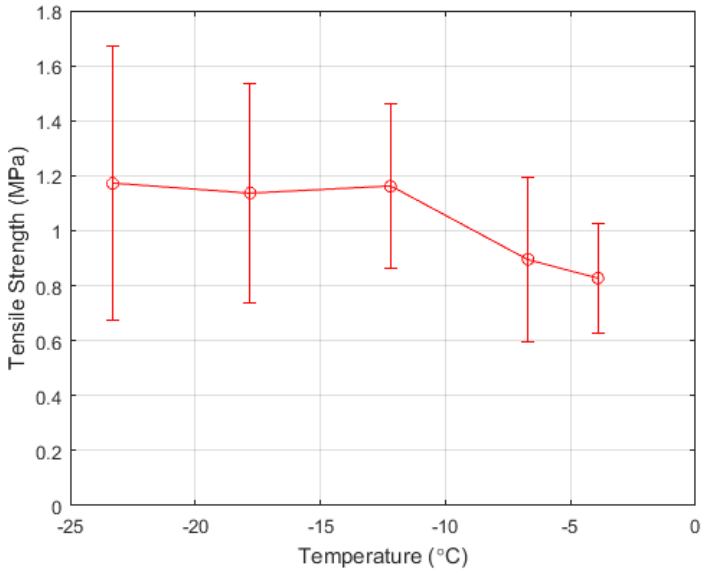

Figure 3-5 – Variation of ice tensile strength with temperature (Figure extracted from *[21]*)

The shear adhesion force, F_S is created due to the shearing of ice on the metal blade. This is also a result of the centrifugal forces experienced by the ice. The shear force on the ice can be calculated by:

$$F_S = \tau A_{a_{ice}} \tag{3-4}$$

The shear adhesion strength is also temperature dependent and varies according to Figure 3-6.

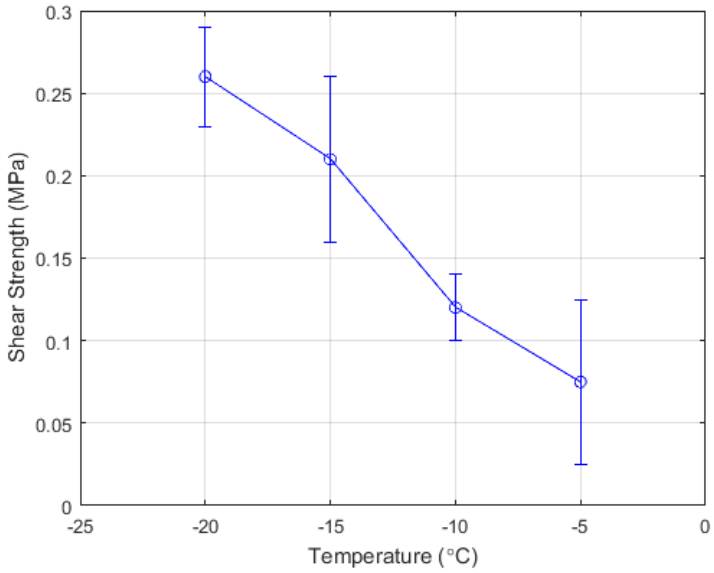

Figure 3-6 – Variation of adhesive shear strength with temperature (Figure extracted from *[22]*)

The areas $A_{C_{ice}}$ and $A_{a_{ice}}$ illustrated in the equations to calculate the shear and cohesive forces are highlighted in

Figure 3-7. These areas were computed by summing up the elemental areas that make up the respective areas.

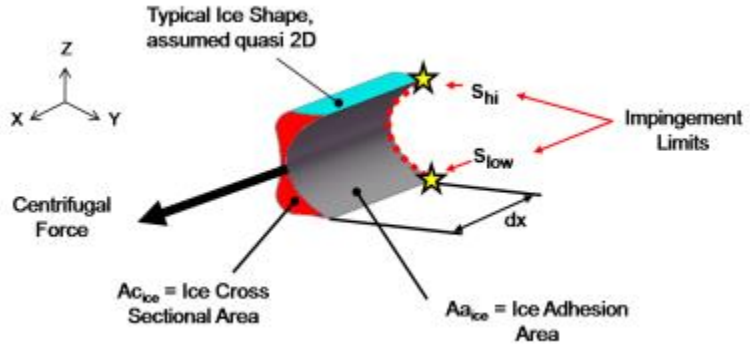

Figure 3-7 – Areas involved in the calculation of forces for ice shedding (Figure from [6])

The 3D aerodynamic force is a summation of the pressure and viscous forces acting on the ice piece due to the flow of air over it. These are a function of average pressure (wall pressure) or shear stresses on the ice, area and unit normal of the element:

$$\vec{F}_{pressure} = \sum_{elem=1}^{nelem} P_w^{elem} A^{elem} \hat{n}^{elem} \tag{3-5}$$

$$\vec{F}_{viscous} = \sum_{elem=1}^{nelem} SS_w^{elem} A^{elem} \hat{n}^{elem} \tag{3-6}$$

$$\vec{F}_{aero} = \vec{F}_{pressure} + \vec{F}_{viscous} \tag{3-7}$$

3.3 Ice trajectory proposed approach

The ice trajectory module consists of several sub-modules. The sequence in which these are run is shown by the flowchart in Figure 3-8.

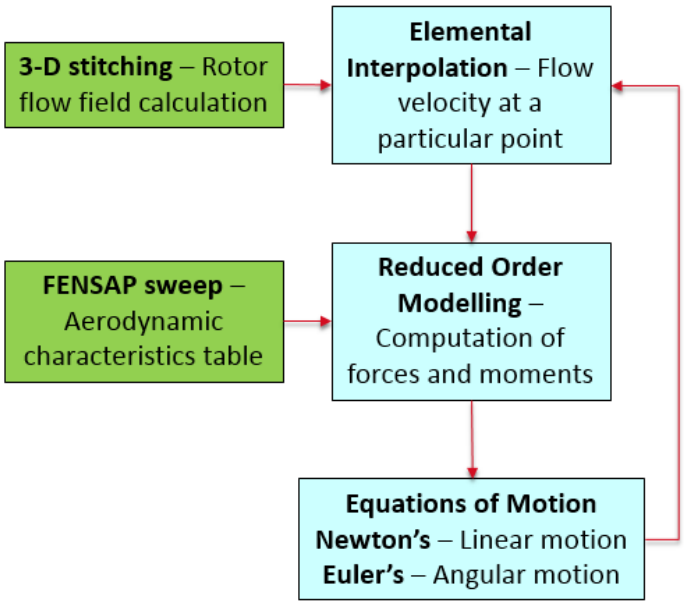

Figure 3-8 – Ice trajectory framework

Firstly, the 3-D stitching methodology was used to compute the rotor flow field into which the ice piece was released. The rotor field was continuously updated according to the azimuth angle of the blades. Secondly, for a shape of ice, an aerodynamics characteristics table was constructed using the sweep feature in FENSAP. As Figure 3-9 displays, at varying combinations of yaw angle and angle of attack, FENSAP simulations were run to obtain the normal, axial, side forces, and

the pitching, yawing, rolling moments for the ice piece. This step was easily parallelized. Although this was the most expensive step, it was carried out very efficiently.

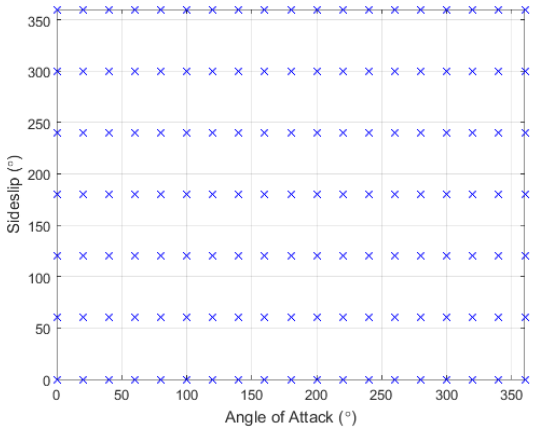

Figure 3-9 – ROM design space of solutions at known orientations

Depending on the location of the ice piece in its trajectory, elemental interpolation was conducted to obtain the flow field velocity at the center of mass ($\vec{V}_{\text{flow}}^{\text{COM}}$) of the ice piece according to:

$$\vec{V}_{flow}^{COM} = \frac{\sum_{i=1}^{n} \frac{v_i}{d_i}}{\sum_{i=1}^{n} \frac{1}{d_i}} \tag{3-8}$$

Where v_i and d_i are the velocities and distances from the center of mass of this ice piece to the nodes encompassing the element it is in, respectively.

By calculating the difference of the ice and the flow field velocities, the relative velocity vector was found. This was used to compute the angle of attack and side slip angle of the ice piece at any instant by:

$$\alpha = \frac{v_{rel}^{b}}{u_{rel}^{b}} \tag{3-9}$$

$$\beta = \frac{w_{rel}^{b}}{u_{rel}^{b}} \tag{3-10}$$

Note that the ‘b’ superscript signifies the body reference system which aligns with the axial, side, and normal directions. The conversion from the inertial to the body reference frame is defined in the quaternion section.

The trajectory of shed-ice from a rotor blade is a 3D problem. Hence a 6-DOF model was developed to compute the resultant angular and linear displacements of the shed-ice piece based on its aerodynamic characteristics. The 6-DOF model allowed translation and rotation in all three directions and about all three axes. It used three body forces (normal, axial and side forces) and three moments (pitching, yawing, rolling) to compute the translational and angular acceleration of the ice particle. Figure 3-10 illustrates the inertial and body axes and the resultant force due to the three forces and three moments acting on the ice piece.

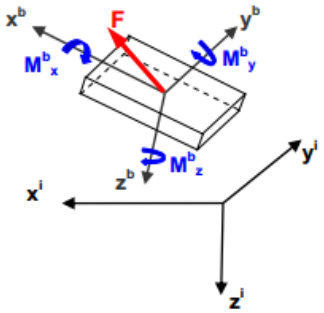

Figure 3-10 – Illustration of Inertial and Body reference axes (Figure obtained from [23])

ROM [24] was then used to compute the forces and moments pertinent to the orientation of the ice piece. ROM uses many snapshots, which are complete solutions obtained at known operating conditions and extracts a basis of vectors, also known as modes, that describe the physical features of a problem. Here, Proper Orthogonal Decomposition (POD) was employed to extract the modes from the snapshots. Then, a multi-dimensional interpolation and a linear combination of the POD modes were used to compute solutions at uncalculated operating conditions. In brief, ROM is a non-linear interpolation technique that uses solutions at known conditions to very quickly compute the solution at an unknown condition.

The decision to use ROM was based on two factors: accuracy and savings on computation time. Considering the variation of an aerodynamic parameter with angle of attack and side slip angles to be highly non-linear, non-linear interpolation is the most suitable for such estimations. To utilize the simpler linear interpolation method, more snapshots would need to be generated to accommodate for this non-linear behavior. Fewer the snapshots used, the quicker the run time, as the code has to go through fewer data points during the interpolation routine.

Considering millions of iterations were performed due to the small timesteps involved in trajectory simulations, this save on run time is vital.

Figure 3-11 compares the solutions generated by ROM with varying number of snapshots and FENSAP solutions for a rectangular plate. As depicted, the 19-snapshot FENSAP plot is very well matched by ROM by only using 10 snapshots. Here, 10 snapshots were used to populate the rest of the data points. On the other hand, only a slight variation from the FENSAP graph is seen when ROM used 7 snapshots. However, the 5-snapshot ROM solution is seen to stray far from the FENSAP solution. Table 3-1 quantifies the difference and shows the savings on pre-processing computation time. This was calculated for the four quadrants by considering two hours per simulation. Insignificant percentage differences relative to the 19-snapshot case and substantial time savings are seen in the 10-snapshot and 7-snapshot cases. Although the 5-snapshot case illustrates the highest in time saved, the lack of accuracy dismissed it. Hence, it was concluded that 7 snapshots were sufficient to represent a shape's characteristics from 0° - 90°.

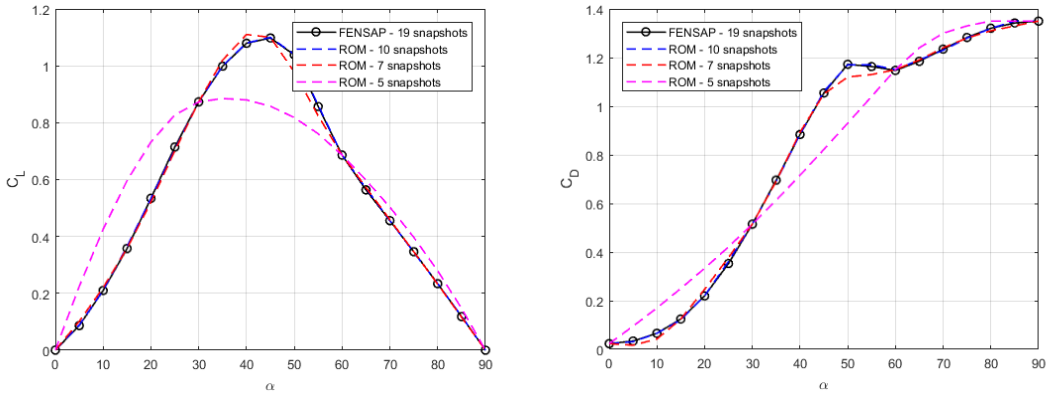

Figure 3-11 – (Left) C_L comparison between FENSAP and ROM generated solutions using varying number of snapshots. (Right) C_D comparison between FENSAP and ROM generated solutions using varying number of snapshots.

Table 3-1 – Maximum percentage difference and pre-processing time savings relative to the 19-snapshot case

Number of snapshots	Maximum percentage difference (%)		Pre-processing time savings (hours)
	CL	CD	
10	1.2	2.4	72
7	5.8	4.4	96
5	22	21	112

Subsequently, using the forces and moments computed by ROM, Newton's and Euler's equations of motion were integrated to obtain the translational and angular displacements, respectively. Newton's equation of motion in the general form is given by:

$$\ddot{x}^b = \frac{1}{m_{ice}}(F^b) \tag{3-11}$$

This can be expanded in the three directions:

$$\ddot{x}^b_{adn} = \frac{1}{m_{ice}}(F_{axial}) \tag{3-12}$$

$$\ddot{y}^b_{adn} = \frac{1}{m_{ice}}(F_{normal}) \tag{3-13}$$

$$\ddot{z}^b_{adn} = \frac{1}{m_{ice}}(F_{side}) \tag{3-14}$$

Considering gravitational acceleration:

$$\begin{Bmatrix} g_{x^b} \\ g_{y^b} \\ g_{z^b} \end{Bmatrix} = \begin{Bmatrix} g_{x^i} \\ g_{y^i} \\ g_{z^i} \end{Bmatrix} [R] \tag{3-15}$$

$$\begin{Bmatrix} \ddot{x}^b \\ \ddot{y}^b \\ \ddot{z}^b \end{Bmatrix} = \begin{Bmatrix} \ddot{x}^b_{adn} \\ \ddot{y}^b_{adn} \\ \ddot{z}^b_{adn} \end{Bmatrix} + \begin{Bmatrix} g_{x^b} \\ g_{y^b} \\ g_{z^b} \end{Bmatrix} \tag{3-16}$$

The Newton's equation of motion was then integrated using a first order forward difference scheme to obtain the linear velocities:

$$u^b_{n+1} = u^b_n + \left(\frac{F_{axial}}{m_{ice}} + g_{y^b}\right)\Delta t \tag{3-17}$$

$$v^b_{n+1} = v^b_n + \left(\frac{F_{normal}}{m_{ice}} + g_{z^b}\right)\Delta t \tag{3-18}$$

$$w^b_{n+1} = w^b_n + \left(\frac{F_{side}}{m_{ice}} + g_{x^b}\right)\Delta t \tag{3-19}$$

A second integration was followed to obtain the linear displacements:

$$x^b_{n+1} = x^b_n + u^b_n \Delta t + \frac{1}{2}\left(\frac{F_{axial}}{m_{ice}} + g_{y^b}\right)(\Delta t)^2 \tag{3-20}$$

$$y^b_{n+1} = y^b_n + v^b_n \Delta t + \frac{1}{2}\left(\frac{F_{normal}}{m_{ice}} + g_{z^b}\right)(\Delta t)^2 \tag{3-21}$$

$$z^b_{n+1} = z^b_n + w^b_n \Delta t + \frac{1}{2}\left(\frac{F_{side}}{m_{ice}} + g_{x^b}\right)(\Delta t)^2 \tag{3-22}$$

On the other hand, the angular displacement of the particle at every timestep was determined through the integration of the Euler equation which in full-form is given by:

$$\frac{d}{dt}(\omega^b) = [I]^{-1}[M^b - (\omega^b \times [I]\omega^b) \tag{3-23}$$

Where

$\frac{d}{dt}(\omega^b) = \begin{Bmatrix} \dot{P}^b \\ \dot{Q}^b \\ \dot{R}^b \end{Bmatrix}$ = angular acceleration in body reference frame

$M^b = \begin{Bmatrix} M_x^b \\ M_y^b \\ M_z^b \end{Bmatrix}$ = moment acting about the body reference frame

$\omega^b = \begin{Bmatrix} P^b \\ Q^b \\ R^b \end{Bmatrix}$ = angular velocity in body reference frame

$[I]$ = the inertia matrix

Considering a simple ice shape where the off-diagonal terms are zero, the equations can be written out as follows:

$$\dot{P}^b = \frac{M_x^b + (I_{yy} - I_{zz})Q^b R^b}{I_{xx}} \rightarrow e(t, P^b, Q^b, R^b) \tag{3-24}$$

$$\dot{Q}^b = \frac{M_y^b + (I_{zz} - I_{xx})R^b P^b}{I_{yy}} \rightarrow f(t, P^b, Q^b, R^b) \tag{3-25}$$

$$\dot{R}^b = \frac{M_z^b + (I_{xx} - I_{yy})P^b Q^b}{I_{zz}} \rightarrow g(t, P^b, Q^b, R^b) \tag{3-26}$$

This system of equations was integrated to obtain the angular velocities in the body reference frame using a 4-stage Runge-Kutta scheme. This integration is detailed in Appendix A. Quaternions, an alternative way of representing an orientation, were then used to obtain angular displacements. They are simpler to form and avoid the gimbal lock issue compared to Euler angles. In a three-dimensional, three-gimbal mechanism, gimbal lock is the loss of one degree of freedom when two of the three axes are driven into a parallel configuration and thereby "locking" the system. They are also more compact, more numerically stable and more efficient in comparison to rotation matrices. They are used in a variety of applications including robotics,

molecular dynamics and flight dynamics. The quaternion (q) representing the orientation of the ice piece at a time t can be expressed as:

$$q = [q_1 \ q_2 \ q_3 \, q_4 \,] \tag{3-27}$$

The quaternion q can be computed from the Euler angles (ψ, θ and φ) which are yaw, pitch and roll by:

$$q_1 = cos\left(\frac{\phi}{2}\right) cos\left(\frac{\theta}{2}\right) cos\left(\frac{\psi}{2}\right) + sin\left(\frac{\phi}{2}\right) sin\left(\frac{\theta}{2}\right) sin\left(\frac{\psi}{2}\right) \tag{3-28}$$

$$q_2 = cos\left(\frac{\phi}{2}\right) sin\left(\frac{\theta}{2}\right) sin\left(\frac{\psi}{2}\right) - sin\left(\frac{\phi}{2}\right) cos\left(\frac{\theta}{2}\right) cos\left(\frac{\psi}{2}\right) \tag{3-29}$$

$$q_3 = -cos\left(\frac{\phi}{2}\right) sin\left(\frac{\theta}{2}\right) cos\left(\frac{\psi}{2}\right) - sin\left(\frac{\phi}{2}\right) cos\left(\frac{\theta}{2}\right) sin\left(\frac{\psi}{2}\right) \tag{3-30}$$

$$q_4 = sin\left(\frac{\phi}{2}\right) sin\left(\frac{\theta}{2}\right) cos\left(\frac{\psi}{2}\right) - cos\left(\frac{\phi}{2}\right) cos\left(\frac{\theta}{2}\right) sin\left(\frac{\psi}{2}\right) \tag{3-31}$$

As mentioned earlier, the rotation matrix [R] was used to change from the inertial reference from to the body reference frame of the ice piece:

$$[R] = 2\begin{bmatrix} q_1^2 + q_2^2 - 0.5 & q_2q_3 - q_1q_4 & q_2q_4 + q_1q_3 \\ q_2q_3 + q_1q_4 & q_1^2 + q_3^2 - 0.5 & q_3q_4 - q_1q_2 \\ q_2q_4 - q_1q_3 & q_3q_4 + q_1q_2 & q_1^2 + q_4^2 - 0.5 \end{bmatrix} \tag{3-32}$$

The quaternion rates were computed from the angular velocity vector (ω^b) using:

$$\dot{q_1} = -\frac{1}{2}(q_2P^b + q_3Q^b + q_4R^b) + \lambda q_1 \tag{3-33}$$

$$\dot{q_2} = \frac{1}{2}(q_1P^b + q_3R^b - q_4Q^b) + \lambda q_2 \tag{3-34}$$

$$\dot{q_3} = \frac{1}{2}(q_1Q^b + q_4P^b - q_2R^b) + \lambda q_3 \tag{3-35}$$

$$\dot{q_4} = \frac{1}{2}(q_1R^b + q_2Q^b - q_3P^b) + \lambda q_4 \tag{3-36}$$

$$\lambda = 1 - (q_1^2 + q_2^2 + q_3^2 + q_4^2) \tag{3-37}$$

The quaternion rates were numerically integrated using the same 4-stage Runge-Kutta scheme to obtain the quaternion for time t+Δt, describing the new orientation of the body. The Euler angles were then computed from the quaternion elements to make it easier to visualize the orientation of the particle in the inertial axis system:

$$\psi = \cos^{-1}\left(\frac{q_1^2 + q_2^2 - q_3^2 - q_4^2}{\cos\theta}\right).(\text{sign}[2(q_2q_3 + q_1q_4)]) \tag{3-38}$$

$$\theta = sin^{-1}[-2(q_2q_4 - q_1q_3)] \tag{3-39}$$

$$\varphi = cos^{-1}\left(\frac{q_1^2 - q_2^2 - q_3^2 + q_4^2}{cos\theta}\right).(sign[2(q_3q_4 + q_1q_2)]) \tag{3-40}$$

4 Results

4.1 Ice shedding

Brouwers, Palacios, Peterson, and Smith [6] studied ice accretion on rotors numerically and experimentally through the Adverse Environment Rotor Test Stand (AERTS) setup at Penn State. It represented a hover test case with ice accretion experiments performed on a model rotor in a refrigerated whirl stand. Table 4-1 summarizes the rotor's technical specifications.

Table 4-1 – AERTS Experimental setup specifications

AERTS – Experimental Setup	
Experiments	Penn State
Airfoil	NACA 0015
Chord	0.173 m
Solidity	0.092
Rotor radius	1.17 m
Twist	-2.1°
Collective pitch	2.5°
Rotational speed	600 RPM
LE material	2024-T3 Aluminum
Weight	1.98 kg/m

A rotational velocity of 600 RPM corresponds to a tip velocity of 74 m/s (Mach 0.23). This is lower than what is usually seen in full-scale helicopters where the tip Mach numbers range from 0.5 to 0.7. However, the availability of data, makes this an important test case. Two runs were simulated with the proposed approach. Run 44 is the only run with published sectional ice shapes. This run was conducted to validate the ice shapes produced. Then, Run 31 was carried out to validate the ice shedding module.

The AERTS test rotor was meshed by the author of this thesis in ANSYS ICEM. To utilize the 3-D stitching algorithm, a specialized mesh as shown in Figure 4-1 had to be created for this test case.

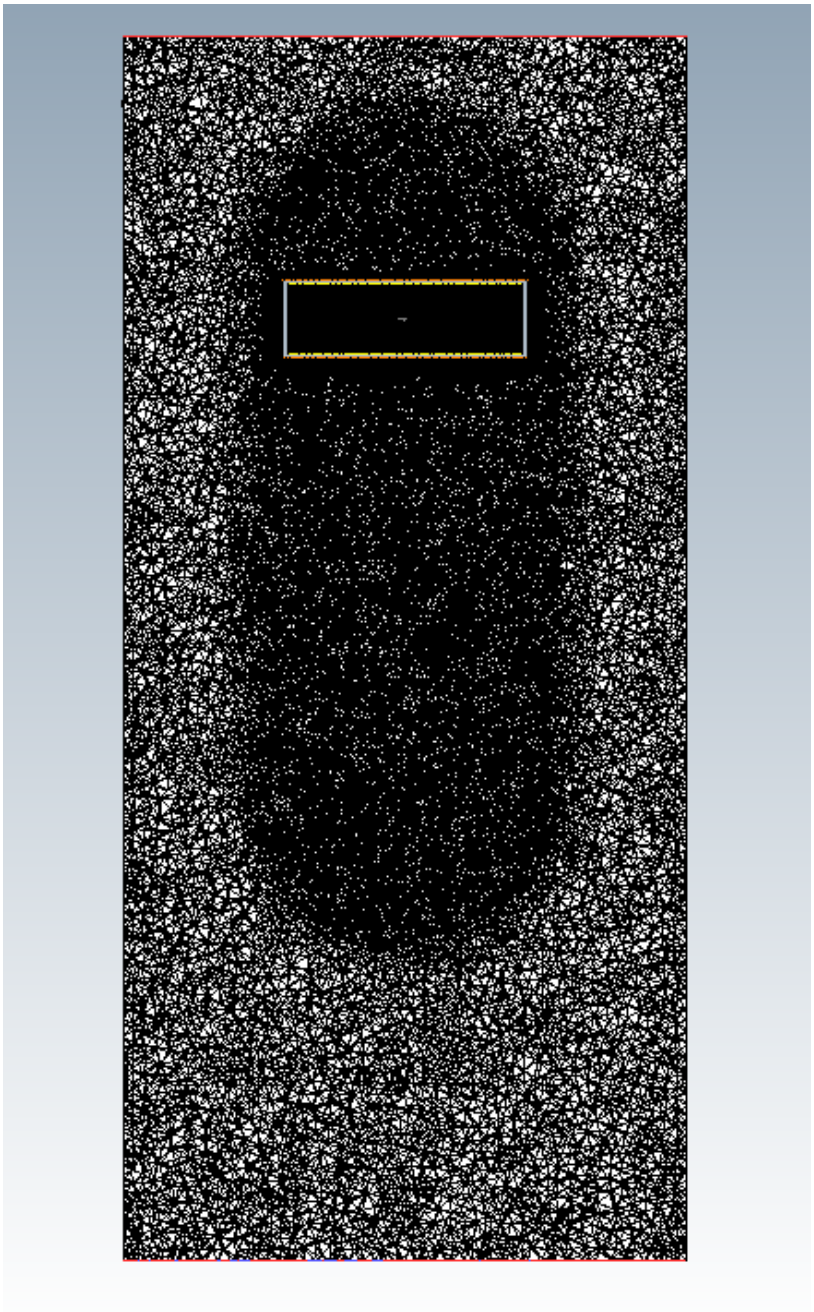

Figure 4-1 – 3-D stitching mesh for the AERTS case, including the stationary and rotating domains

The unstructured mesh included a rotating domain and a stationary domain separated by a gap as highlighted in Figure 4-2 and Figure 4-3. The rotating domain described the rotor

according to the specifications emphasised in Table 4-1. The stationary domain encompassed the surrounding air.

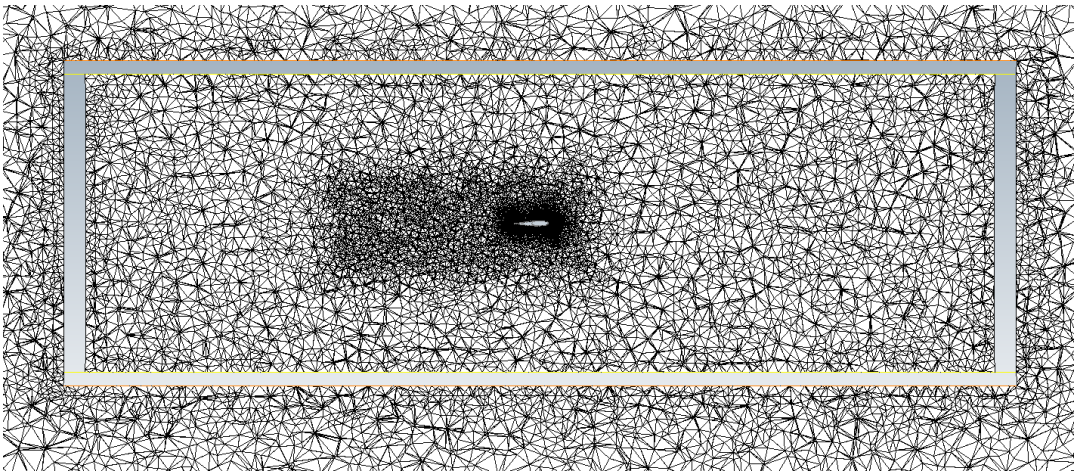

Figure 4-2 – Close-up of the rotational domain showing a cross-section of the blade and highlighting the mesh elements around the blade

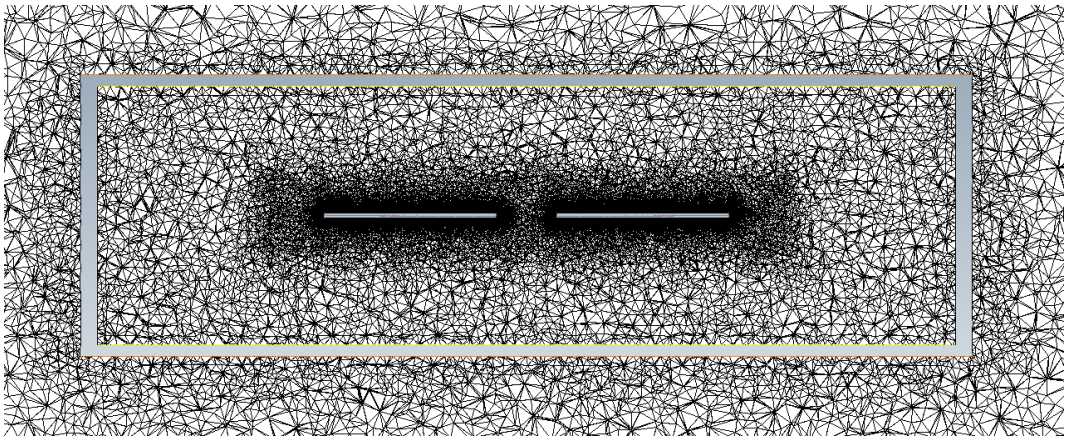

Figure 4-3 – Close-up of the rotational domain showing both blades and highlighting the mesh elements around the blades

An Octree mesh was initially used to generate the elements of the rotational domain. The body elements were then deleted, leaving only the surface elements. After that, the blade elements were extruded to the cylinder describing the ends of the rotational domain using Delaunay triangulation. 32 prism layers were then added in the boundary layer. This is depicted in Figure 4-4. The stationary mesh was generated by extruding the surface elements of the rotational mesh using an Advancing Front formulation. The Delaunay and Advancing Front techniques were employed to ensure a smooth transition in element sizes throughout the two

domains. The rotational mesh contained 10.4 million elements and the stationary mesh contained 2.8 million elements, summing up to 13.2 million elements.

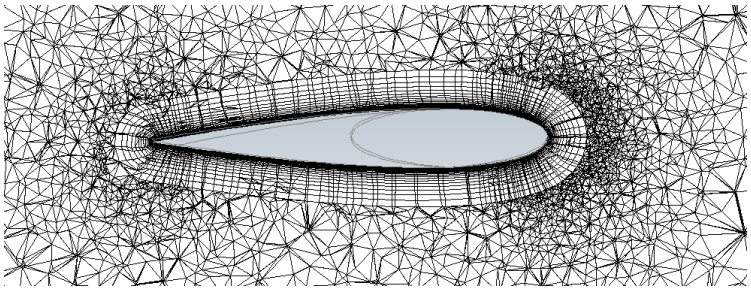

Figure 4-4 – Extreme close-up of the rotational domain, showing a cross-section of the blade and highlighting the prism layers around it

4.1.1 AERTS Run 44 – Ice Accretion Validation

The proposed method applied the 3-D stitching algorithm to obtain the flow and droplet solutions. The Navier-Stokes equations were solved. To validate this technique, AERTS Run 44 was conducted since experimental sectional ice shapes are published. Table 4-2 highlights the conditions pertaining to this run.

Table 4-2 – AERTS run 44 simulation conditions

AERTS – Run 44 – Ice shape validation	
Temperature	-10.1 °C
MVD	15 µm
LWC	1.3 g/m^3
Ice accretion time	180 s
Ice shedding	No

Figure 4-5 compares the ice shapes computed by the 3-D stitching methodology with the experimental ice shapes and with the Quasi 3-D methodology developed by Kelly [16]. Similar to the methodology developed by Brouwers et al., Kelly implemented an approach at the McGill CFD Lab (author's laboratory). Flow and droplet simulations were conducted in a 2-D manner at various sections along the blade using FENSAP. These solutions were then combined to form a 3-

D solution and fed into ICE-3D, thus making it a Quasi-3D approach. The Quasi-3D approach is unable to trace the complex ice shapes seen in experiments. It appears to predict the ice shapes in the form of simple shapes with rounded edges. Furthermore, it under predicts the ice thickness at all sections of the blade. On the other hand, the fully 3-D approach better computes the thickness of the ice shapes at the respective blade sections. In addition, it is capable of better capturing the complex features of the ice shapes seen in the experiments and thus better represents it.

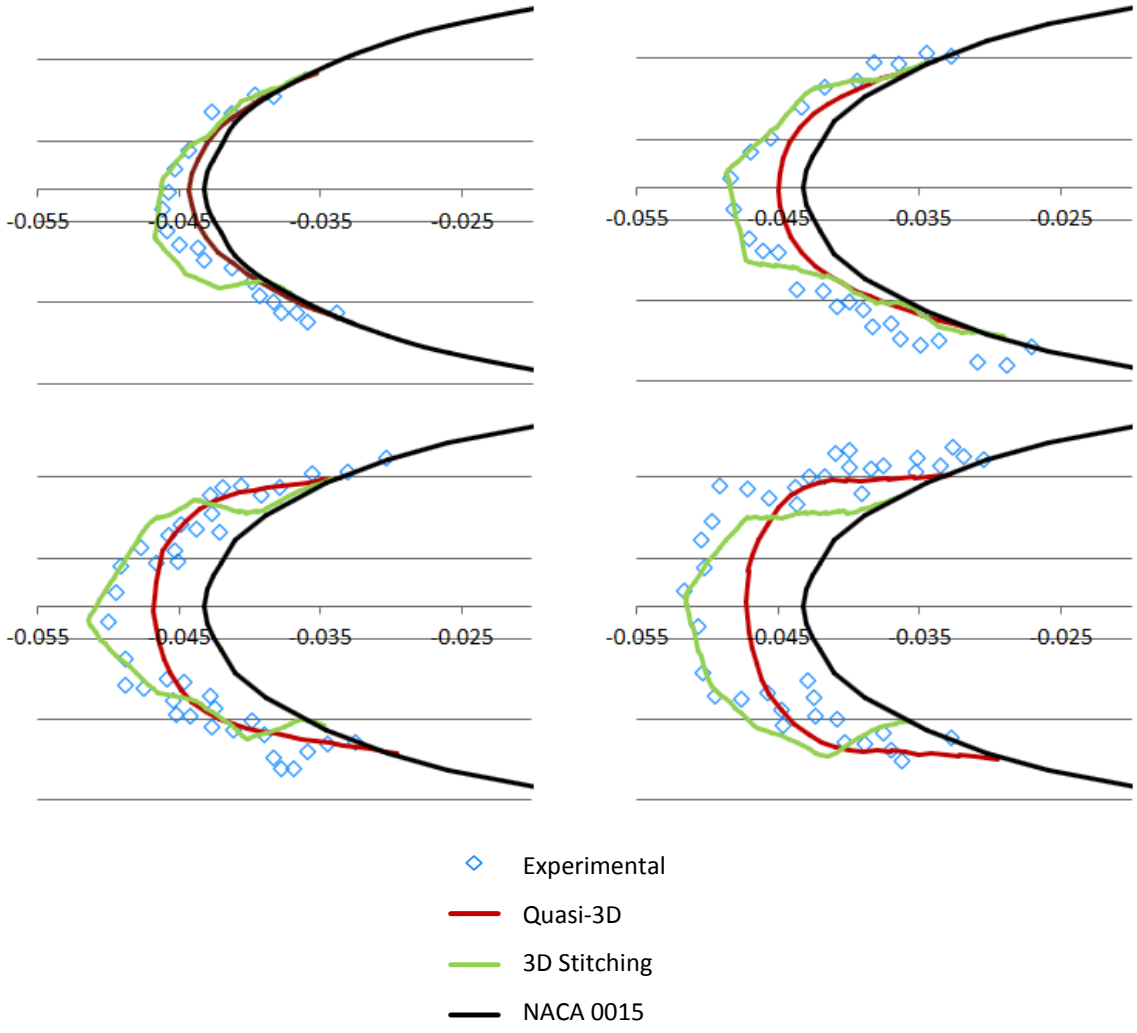

Figure 4-5 – AERTS Case 44 Sectional ice shapes – (Top left) At 60% span. (Top right) At 70% span. (Bottom left) At 80% span. (Bottom right) At 90% span.

4.1.2 Ice Shedding in Hover – AERTS Run 31 – Ice Shedding Validation

The simulation of Run 44 concluded that the fully 3-D approach produced reasonable ice shapes. The next step was to validate the ice shedding module. Run 31 was then simulated since ice shedding was observed to occur after 215 seconds of icing at 82% of the blade span. Ice was accreted in 30 second intervals and the forces contributing to ice shedding were analyzed. Table 4-3 highlights the run conditions.

Table 4-3 – AERTS run 31 simulation conditions

AERTS – Run 31 – Ice Shedding Validation	
Temperature	-5.8 °C
MVD	35 µm
LWC	3.0 g/m^3
Shed Location	0.82 R
Shed Time	215 s

Figure 4-6 – Figure 4-12 demonstrate the development of the forces leading to ice shedding, the growth of ice along the blade and the change in ice shape at 90% of the blade. The x-axis represents the size of the combined element analyzed at an instant. For instance, at 90% of the blade span, the combined element being studied is the ice piece from 90% to the tip of the blade.

The figures depict an increase in centrifugal force from the tip to about 40% of the blade, followed by a decline towards the root. Although the radial location of the center of mass of the combined element is decreasing from tip to root, its mass is increasing leading to an increase in centrifugal force near the tip. Near the root, the increase in mass is not as high as near the tip. Here, the radial location component dominates and results in a decrease in centrifugal force. The critical tensile force is seen to have a general decrease from tip to root. This is because of the decline in ice thickness, which leads to a decrease in area the combined element makes with its neighbouring ice element. The contact area of the combined element and the blade increases

which consequently leads to an increase in critical shear force from tip to root. The aerodynamic force is illustrated to be negligible for this case. This complies with what is seen in literature. The tip Mach number for this case is 0.23, however, aerodynamic forces only become significant when tip Mach numbers exceed 0.45.

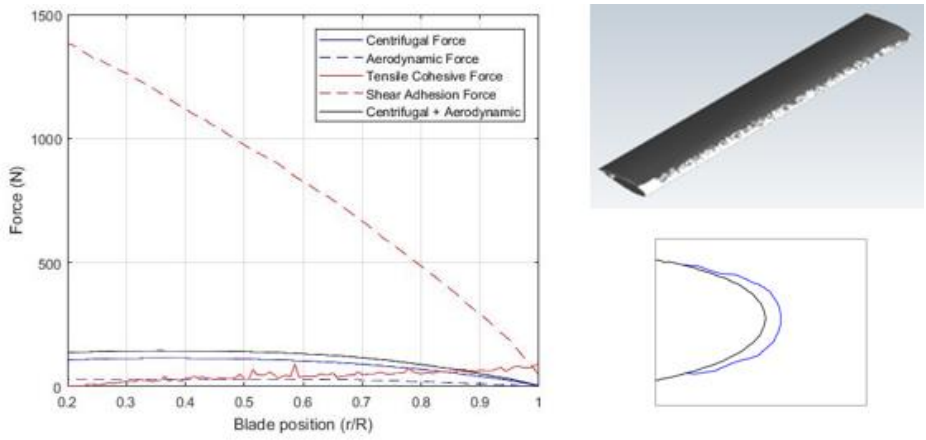

Figure 4-6 – AERTS Case 31 – (Left) Forces contributing to ice shedding after 30 s. (Top right) Iced blade after 30 s. (Bottom right) Ice shape at 0.9 R after 30 s.

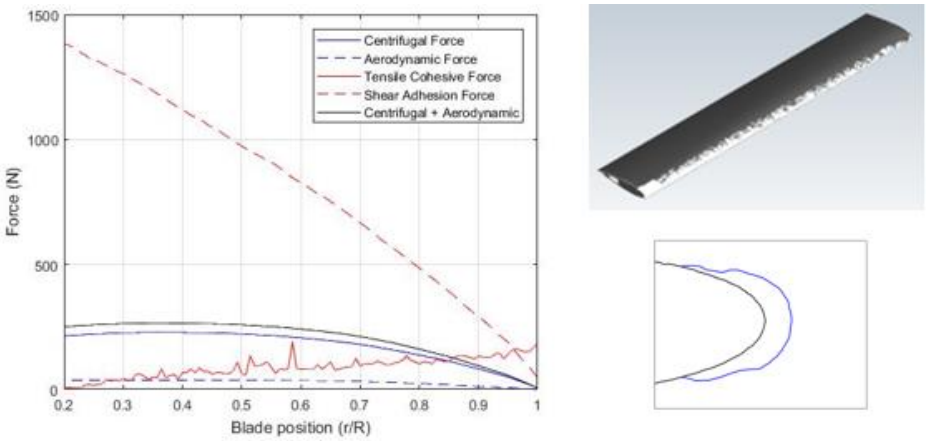

Figure 4-7 – AERTS Case 31 – (Left) Forces contributing to ice shedding after 60 s. (Top right) Iced blade after 60 s. (Bottom right) Ice shape at 0.9 R after 60 s.

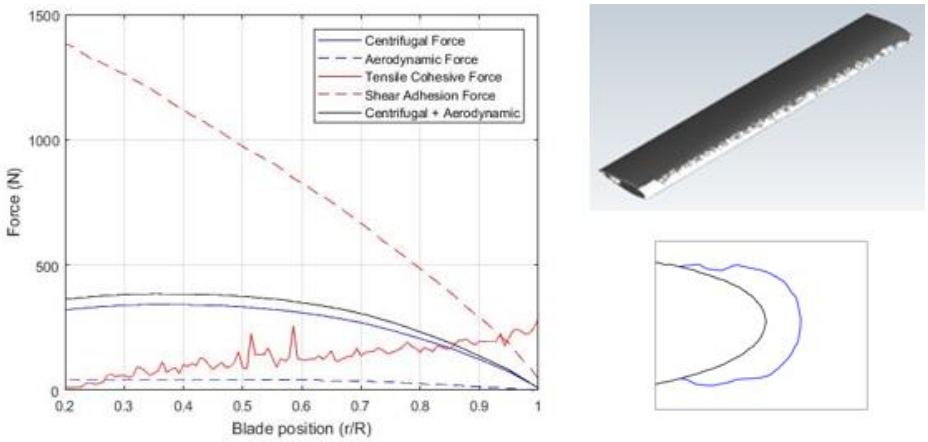

Figure 4-8 – AERTS Case 31 – (Left) Forces contributing to ice shedding after 90 s. (Top right) Iced blade after 90 s. (Bottom right) Ice shape at 0.9 R after 90 s.

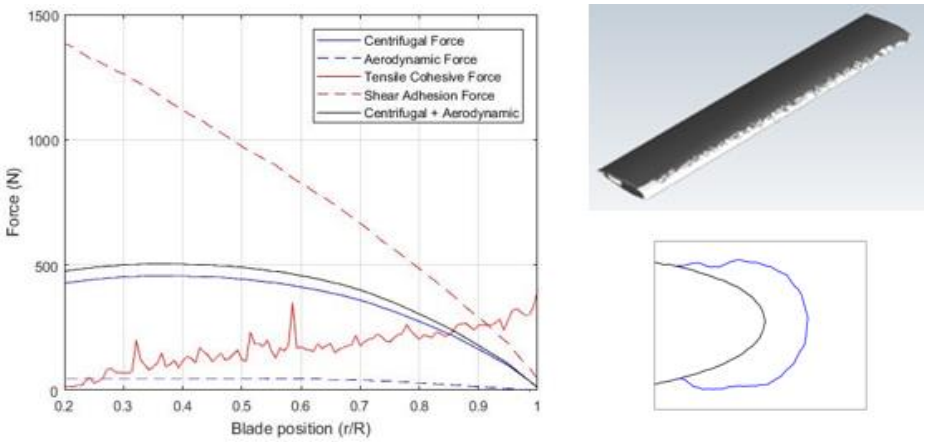

Figure 4-9 – AERTS Case 31 – (Left) Forces contributing to ice shedding after 120 s. (Top right) Iced blade after 120 s. (Bottom right) Ice shape at 0.9 R after 120 s.

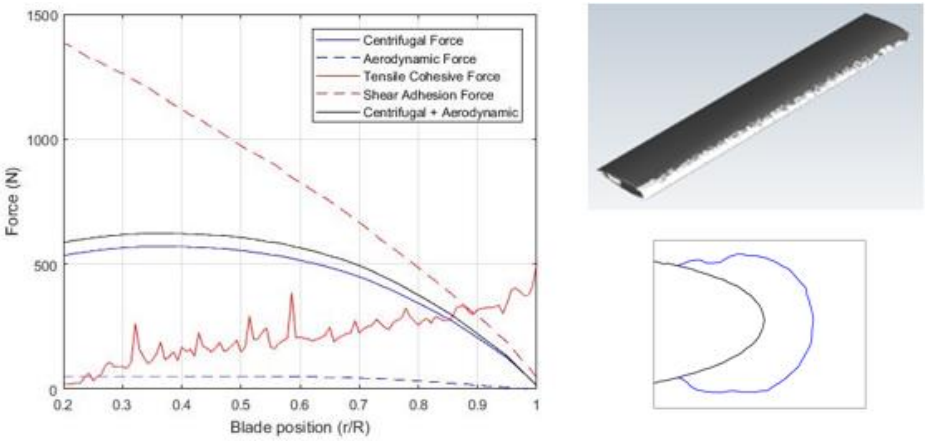

Figure 4-10 – AERTS Case 31 – (Left) Forces contributing to ice shedding after 150 s. (Top right) Iced blade after 150 s. (Bottom right) Ice shape at 0.9 R after 150 s.

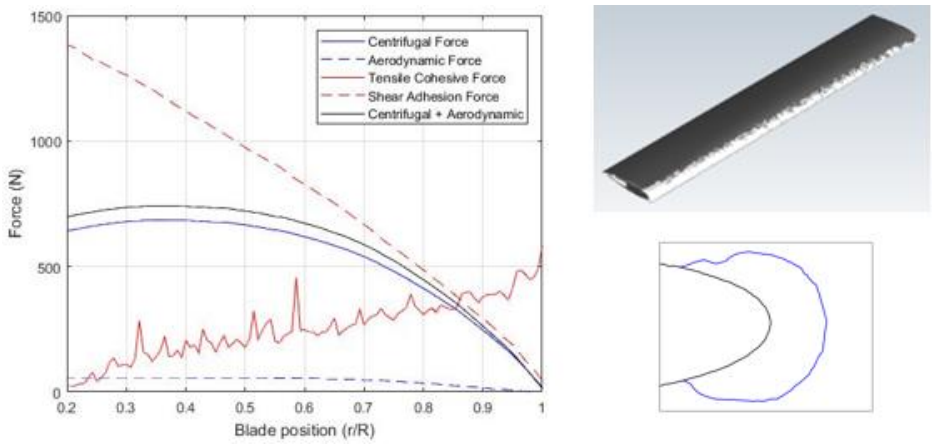

Figure 4-11 – AERTS Case 31 – (Left) Forces contributing to ice shedding after 180 s. (Top right) Iced blade after 180 s. (Bottom right) Ice shape at 0.9 R after 180 s.

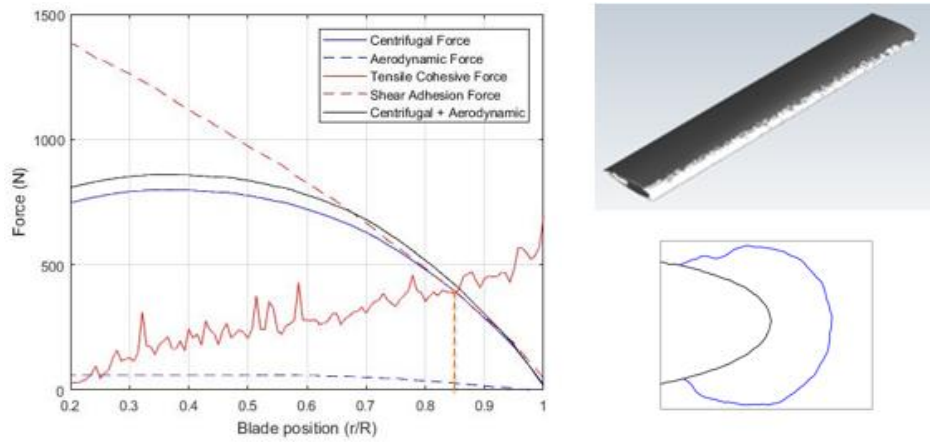

Figure 4-12 – AERTS Case 31 – (Left) Forces contributing to ice shedding after 210 s. (Top right) Iced blade after 210 s. (Bottom right) Ice shape at 0.9 R after 210 s.

With an increase in ice accretion time, more ice is added to the blade. Since the mass of ice is increasing, the centrifugal forces rise from one instant of analysis to another. Added mass of ice also means that the thickness of the ice grows and this is seen in the increase in tensile forces in Figure 4-6 to Figure 4-12. The shear is observed to be unaltered because ice is being added to an already existing layer of ice. Hence, the area the ice makes with the blade changes insignificantly. After 210 s of icing, the summation of the centrifugal and aerodynamic forces at the 85% mark along the blade exceeds the critical tensile force leading to a crack in the ice. This crack then propagates, and eventually leads to ice shed as the summation is also greater than the critical shear force at this point. Table 4-4 summarizes the shedding time and location as observed in the experiments and what is calculated numerically. Finally, Figure 4-13 represents

shed-ice piece geometry. The proposed approach is judged to be able to accurately compute the shed time and location, therefore validating the ice shedding module.

Table 4-4 – Comparison of shedding time and location between experimental and developed numerical model

Method	Shedding Time (seconds)	Shed location (%R)
Experimental	215	82
Numerical	210	85

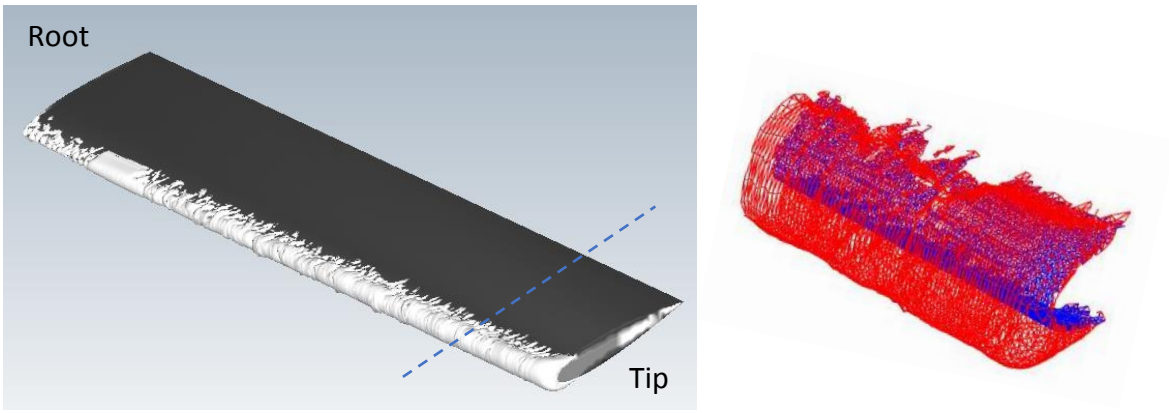

Figure 4-13 – AERTS Case 31 – (Left) Ice shed location. (Right) Shed-Ice geometry.

4.1.3 Ice Shedding in Forward Flight – Georgia Tech

Georgia Tech conducted experiments on a two-bladed rotor in axial flight [25]. Experiments were performed to study the aerodynamic interactions between a rotor and a cylindrical airframe with a hemispherical nose in low speed forward flight. Codes were also built to predict the effect of rotor's wake on the fuselage. These forward flight experiments were performed in the Georgia Tech 2.13 x 2.74 m wind tunnel. Table 4-5 highlights the technical specifications of the experimental rotor.

Table 4-5 – Georgia Tech Experimental setup specifications

Georgia Tech – Experimental Setup	
Experiments	Georgia Tech.
Airfoil	NACA 0015
Chord	0.086 m
Rotor radius	0.457 m
Forward flight speed	10 m/s
Collective pitch	10°
Twist	0°
Rotational speed	2100 RPM
Longitudinal shaft angle	4.06°
Lateral shaft angle	2.03°
Fuselage diameter	0.134 m

The mesh was created as part of a thesis from the McGill CFD Lab by Nathoo [26]. Flow and droplet solutions were reported and compared to experimental measurements. The Euler equations were solved to compute the flow field around the rotor-fuselage body. Again, a specialized mesh with a gap between the rotating and stationary as shown in Figure 4-14 was created to calculate the flow field. The rotational domain consisted of the blades, and the stationary domain contained the fuselage and the surrounding air, as illustrated in Figure 4-15.

Since the Euler equations were solved, no prism layers were added as evident in Figure 4-16. The unstructured mesh consisted of 5 million tetrahedral elements.

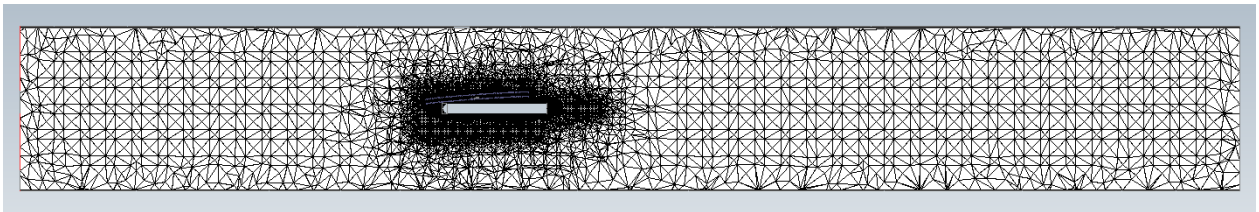

Figure 4-14 – Georgia Tech mesh, highlighting the rotational and stationary domains

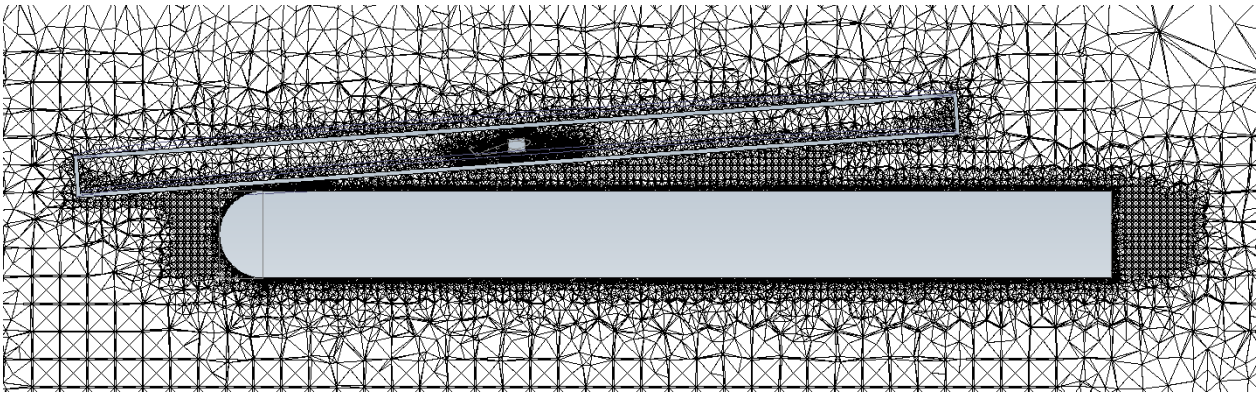

Figure 4-15 – Close-up of the Georgia Tech mesh, showing the rotational and stationary domains

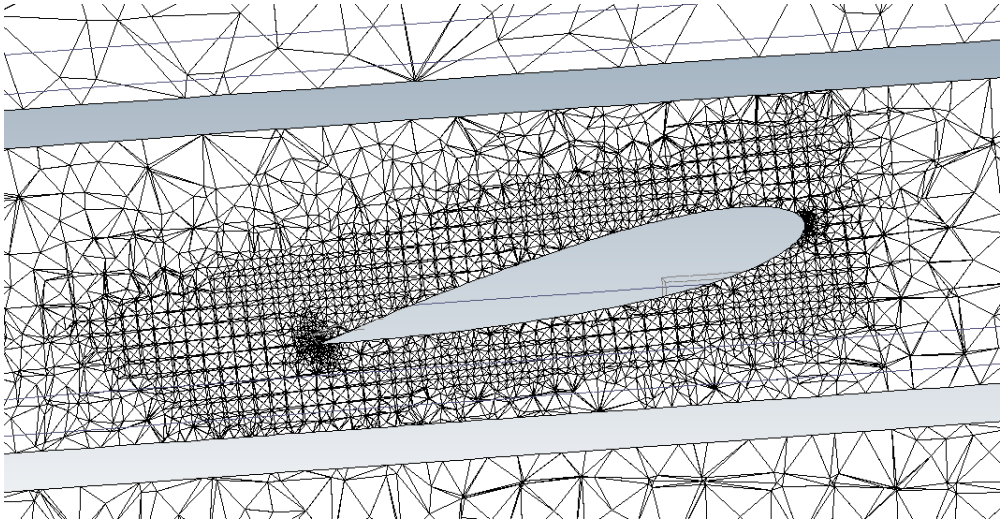

Figure 4-16 – Extreme close-up of the rotational domain illustrating the mesh around the blade

The author of this thesis simulated the forward flight test case in icing conditions as a numerical experiment, to test the application of the ice shedding module. Table 4-6 summarizes the droplet conditions used for this simulation.

Table 4-6 – Georgia Tech numerical simulation parameters

Georgia Tech – Ice Shedding Numerical Experiment	
Temperature	-5.8 °C
MVD	35 µm
LWC	3.0 g/m^3

Ice shedding analyses were conducted at 20 s intervals. Figure 4-17 to Figure 4-19 illustrate the development of the forces contributing to ice shedding at these intervals. Extremely high centrifugal forces are experienced by the rotor because of the high rotational speed. Consequently, the ice is shed much earlier than the hover case. As Figure 4-19 depicts, ice is found to shed at 73% of the blade span after 60 s of ice accretion. Again, due to the low Mach number (M = 0.29), the aerodynamic forces are almost insignificant. Finally, Figure 4-19 shows the shed ice piece.

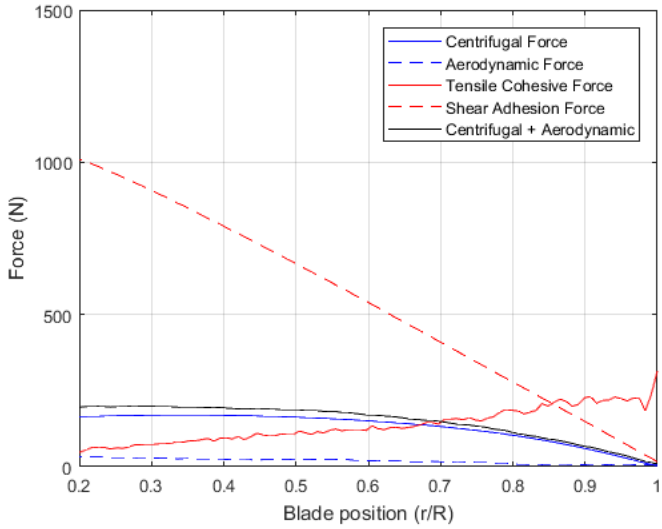

Figure 4-17 – Georgia Tech case – Forces contributing to ice shedding after 20 s

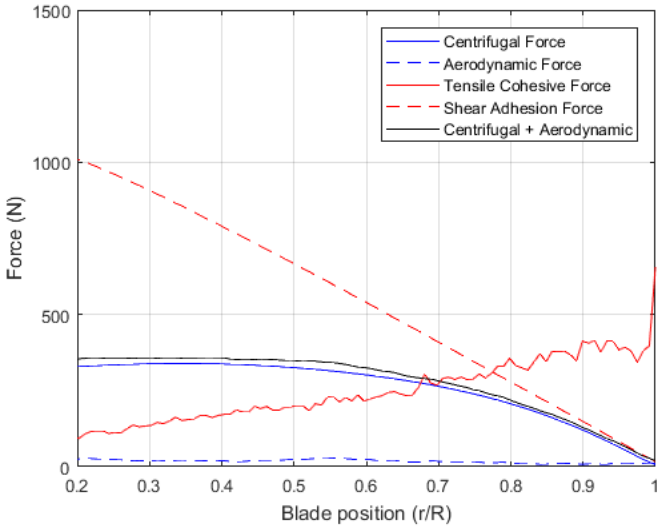

Figure 4-18 – Georgia Tech case – Forces contributing to ice shedding after 40 s

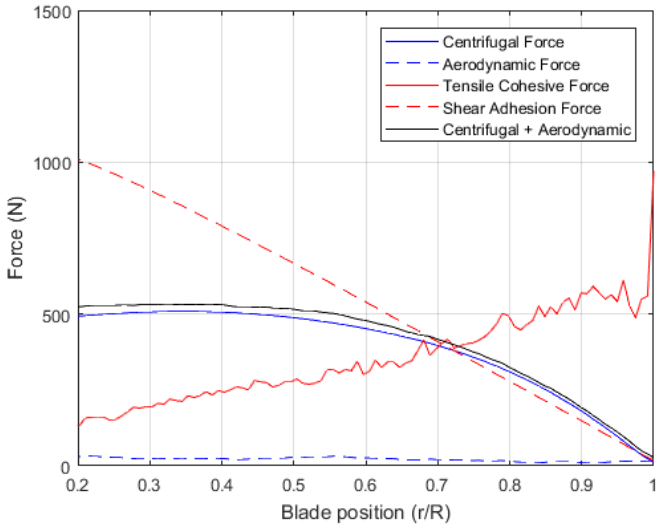

Figure 4-19 – Georgia Tech case – Forces contributing to ice shedding after 60 s

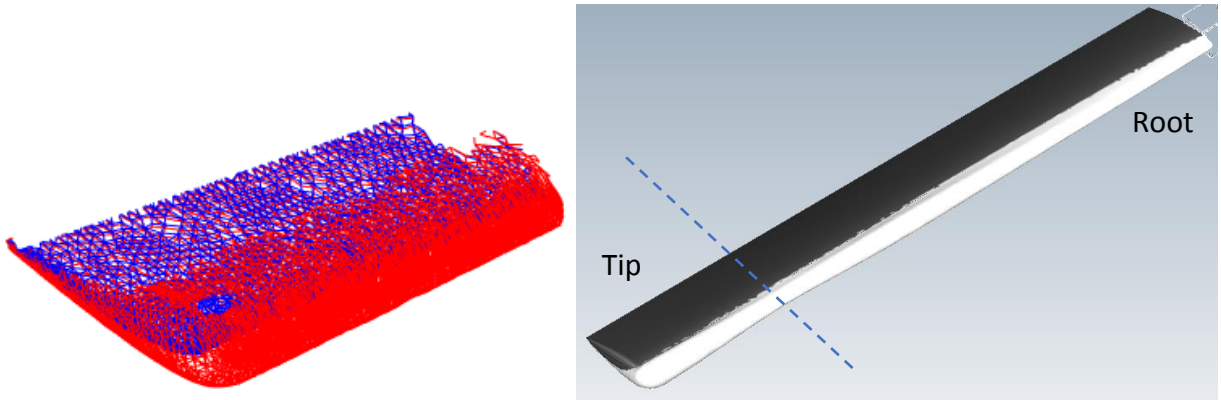

Figure 4-20 – Georgia Tech case – (Left) Shed-Ice geometry. (Right) Ice shed location.

4.2 Ice trajectory

4.2.1 6-DOF Verification

Ice trajectories are composed of two components – the linear and angular motion. Verification tests were performed for both mechanisms.

The linear trajectory was verified by computing the linear motion of a sphere initialized at (4,2,1) m/s in a flow field with velocity (2,1,0) m/s under the influence of drag only. This was analyzed with and without gravity. A sphere of radius 0.1 m and density 917 kg/m^3 was given a mass of 0.75 kg and C_D of 0.5. Figure 4-21 – Left shows that the drag causes a drop in the initial velocity of the ice piece to the flow field velocity as would be expected. With gravity, Figure 4-21 – Right shows that the z-component of the ice velocity declines to the respective terminal velocity which equates to 1.02 m/s. The terminal velocity is calculated by,

$$u_\infty = \sqrt{\frac{2mg}{C_D \rho S}} \tag{4-1}$$

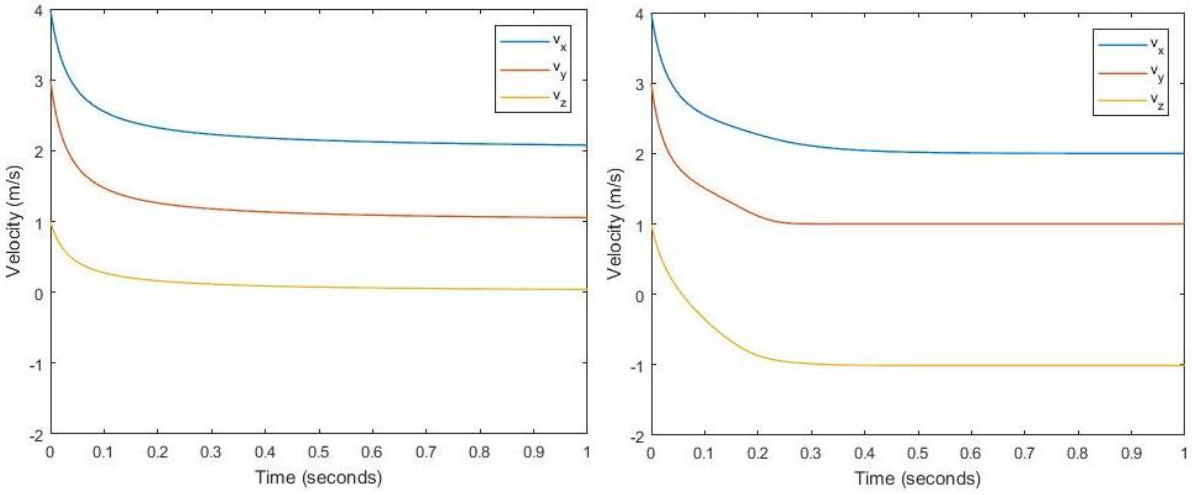

Figure 4-21 – Change in linear velocity with time – (Left) No gravity. (Right) With gravity.

The integration of the Euler equations was verified through three test cases involving a tumbling cylinder [27]. These test cases are summarized in Table 4-7.

Table 4-7 – Summary of Euler verification test cases

	Test Case 1	Test Case 2	Test Case 3
Inertia	$I_1 = 1.0, I_2 = 1.0, I_3 = 0.5$	$I_1 = 1.0, I_2 = 10.0, I_3 = 100.0$	$I_1 = 1.0, I_2 = 10.0, I_3 = 100.0$
Initial angular velocity	(1.0, 0.0, 0.5)	(0.0, 0.0, 1.0)	(0.0, 1.0, 0.0)
Initial Moment	(0.0, 0.0, 0.0)	(0.01, 0.0, 0.0) for 0.1 s	(0.01, 0.0, 0.0) for 0.1 s
Time step	1.0 s		

The system was initialized by an angular velocity about two of the axes in Test Case 1. Figure 4-22 illustrates the response of the system relative to the analytical solution of the problem described by the equations below:

$$\omega_1 = acos(\lambda t) \tag{4-2}$$

$$\omega_2 = bsin(\lambda t) \tag{4-3}$$

$$\omega_3 = c \tag{4-4}$$

The coefficients were set to the following: a=1.0, b=-1.0, c=0.5, λ=0.25. The computed angular motion about the two axes of the system are seen to follow the analytical solutions very closely, therefore successfully modelling this simple case.

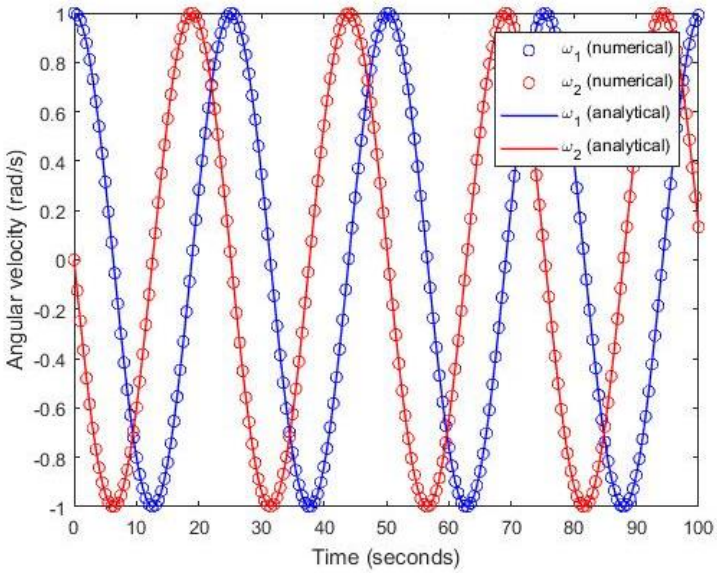

Figure 4-22 – Euler verification test case 1 results – Angular velocity vs Time

For Test Cases 2 and 3, an instantaneous perturbation was applied to the system in the form of a moment for a certain duration. In the case of Test Case 2, when a time step of 0.1 s was used, angular velocities about two axes were induced and the response to the system as seen in [27] can be observed in Figure 4-23 – Left. However, the system of equations is undamped and therefore a decaying response should not be seen. Nevertheless, with a smaller time step (Δt = 0.001 s or less), a periodic change in angular velocity is observed. This complies with what is computed in [9], where the same test cases were implemented.

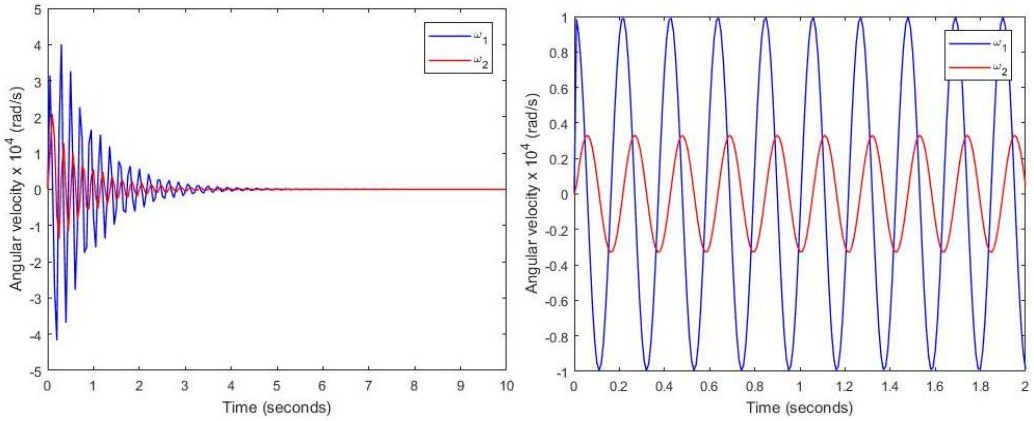

Figure 4-23 – Euler verification test case 2 results – (Left) Angular Velocity vs Time where Δt = 0.1 s. (Right) Angular Velocity vs Time where Δt = 0.001 s.

In Test Case 3, angular movement was initialized around the semi-major axis. This resulted in angular motion about all three axes, where the rates are proportional to the moments of inertia about the respective axes as shown by Figure 4-24. Since the system is undamped, the angular velocities do not dampen out. Following the successful completion of the three test cases, it was verified that the 6-DOF was implemented correctly.

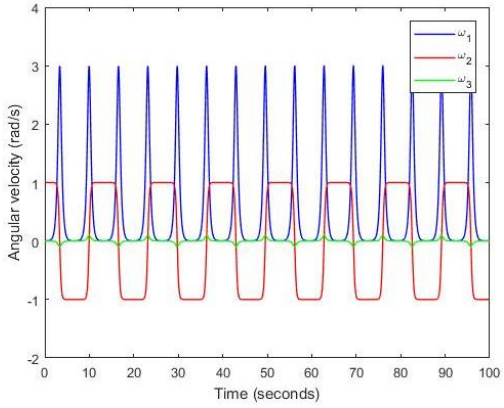

Figure 4-24 – Euler verification test case 3 results – Angular Velocity vs Time

4.2.2 Aerodynamics Database Validation – Rectangular Plate

The rectangular plate geometry was chosen as one of the shapes to model ice detachments from helicopter blades. This is a simple shape and a wide range of data is available to validate its aerodynamic properties. Results from experiments and numerical simulations in FLUENT are presented in [15]. These were used to validate the aerodynamics characteristics table generated by FENSAP.

A computational grid of 1.5 million elements was created. The geometry of the rectangular plate corresponded to that in [15]. An Octree mesh was first used to generate the surface meshes and then an Advancing Front mesh was used to fill the domain with smooth transitioning elements. Lastly, prism layers were added in the boundary layer. Figure 4-25 and Figure 4-26 illustrate the full view and a close-up view of the grid.

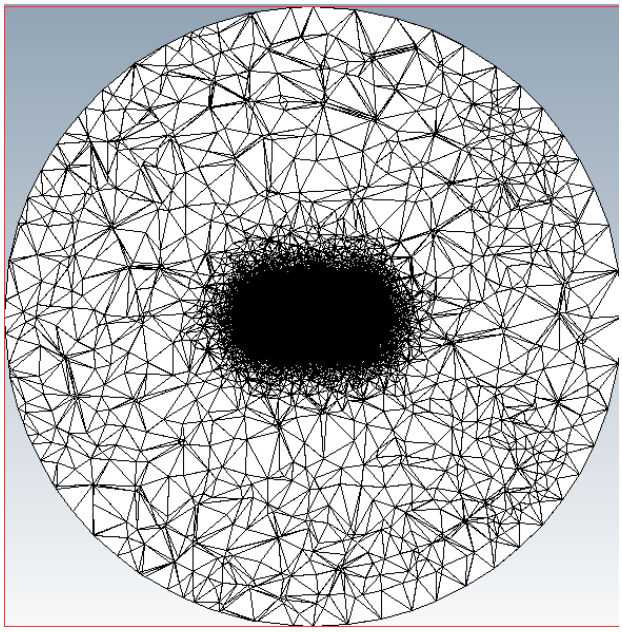

Figure 4-25 – Full view of rectangular plate mesh

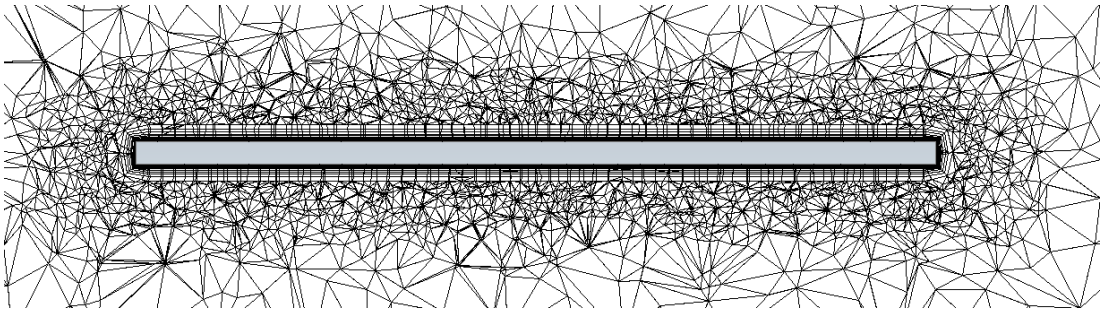

Figure 4-26 – Close-up view of rectangular plate mesh, highlighting the prism layer

The aerodynamics characteristics table was created using the FENSAP sweep feature. A code was developed to extract the forces and moments from the respective output files. Figure 4-27 – Left and Right show, respectively, the variation of lift and drag coefficients with angle of attack at $\beta = 0°$. These figures compare the FENSAP results with that obtained experimentally and using FLUENT. As illustrated, FENSAP's lift and drag coefficients are very similar to what is seen in experiments and, interestingly, are more accurate than FLUENT. This validates the rectangular plate aerodynamics produced through FENSAP. Force and Moment coefficients at all side slip angles are demonstrated in Appendix B.

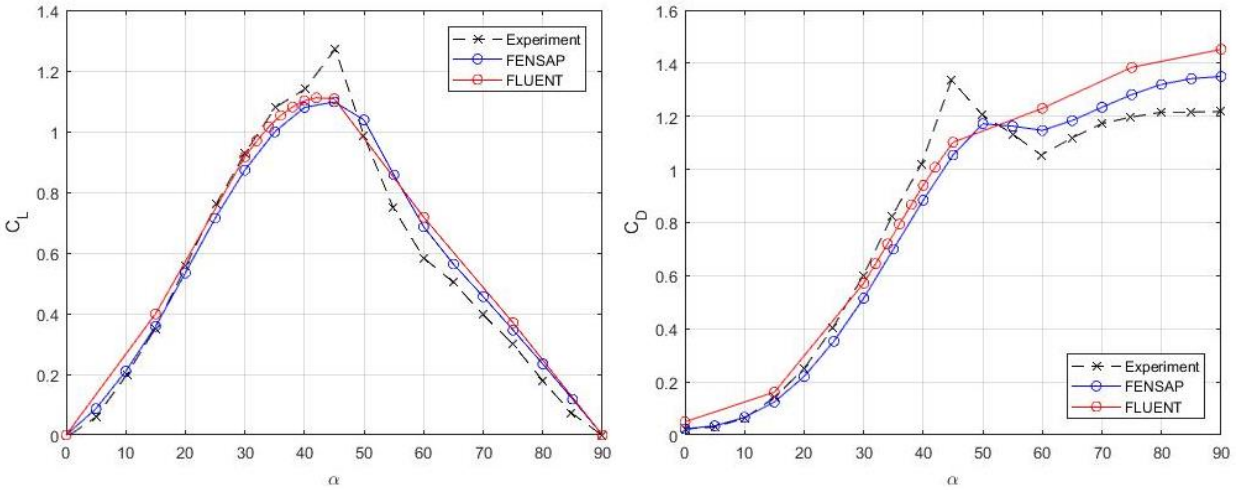

Figure 4-27 – Validation of aerodynamic characteristics of the rectangular plate geometry – (Left) C_L comparison with experiments and Fluent. (Right) C_D comparison with experiments and Fluent.

4.2.3 Aerodynamics Database Validation – Semi-Circular Shell

An aerodynamics database for a Semi-Circular Shell (SCS) geometry was also generated. The SCS represents more closely ice shapes shed from helicopter blades. A similar procedure to the rectangular plate was used to create the SCS mesh but with 3 million elements to better map the more complex shape of the SCS. Figure 4-28 and Figure 4-29 show the full view and a close-up view of the grid.

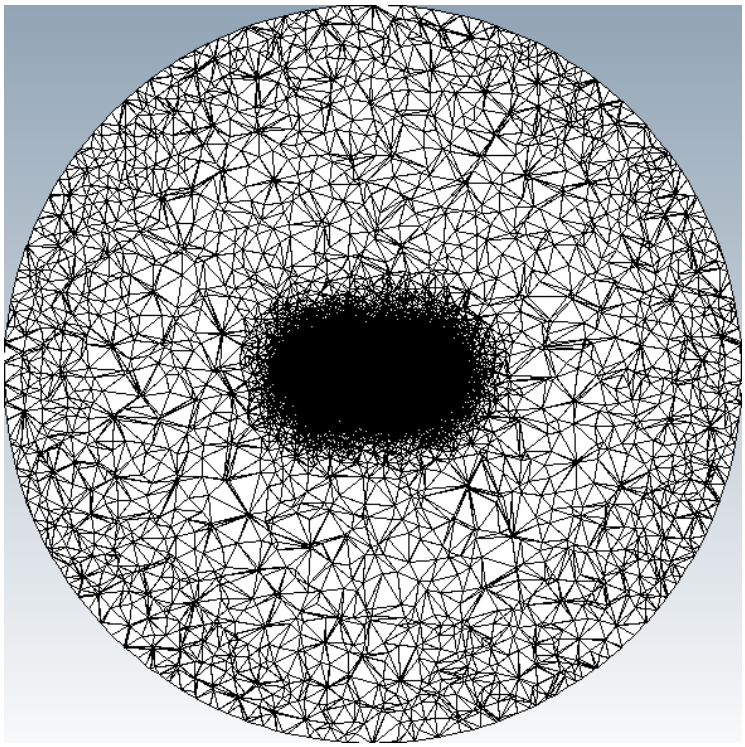

Figure 4-28 – Full view of SCS mesh

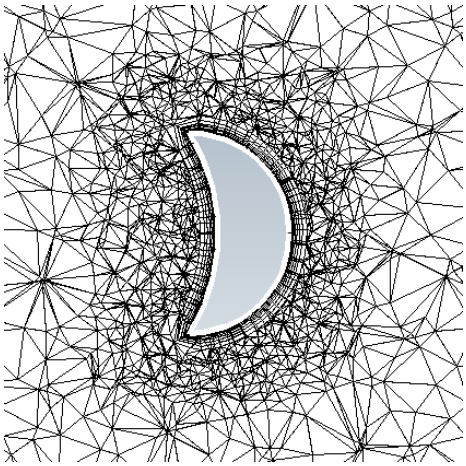

Figure 4-29 – Close-up view of SCS mesh highlighting the prism layer

Figure 4-30 – Left and right show the variation of the lift and drag coefficients, respectively, with angle of attack at β = 0°. These figures compare the FENSAP results with experiments and with FLUENT. Only a few cases were simulated in FLUENT in [15]. FLUENT is seen to slightly over-predict the lift and drag coefficients in these cases. On the other hand, FENSAP slightly under-predicts the magnitude of the lift coefficient. In the case of drag coefficient, FENSAP and FLUENT over-predict at very small and very large angles of attack but FENSAP slightly under-predicts at angles of attack in between. However, the trends are captured remarkably well by FENSAP. In fact, FENSAP incredibly captures the flow change from the convex to the concave side of the SCS as seen by the sudden increase in lift coefficient from 90° to 95°. However, the experiments curiously do not appear to highlight this. Force and moment coefficients at all side slip angles are demonstrated in Appendix C.

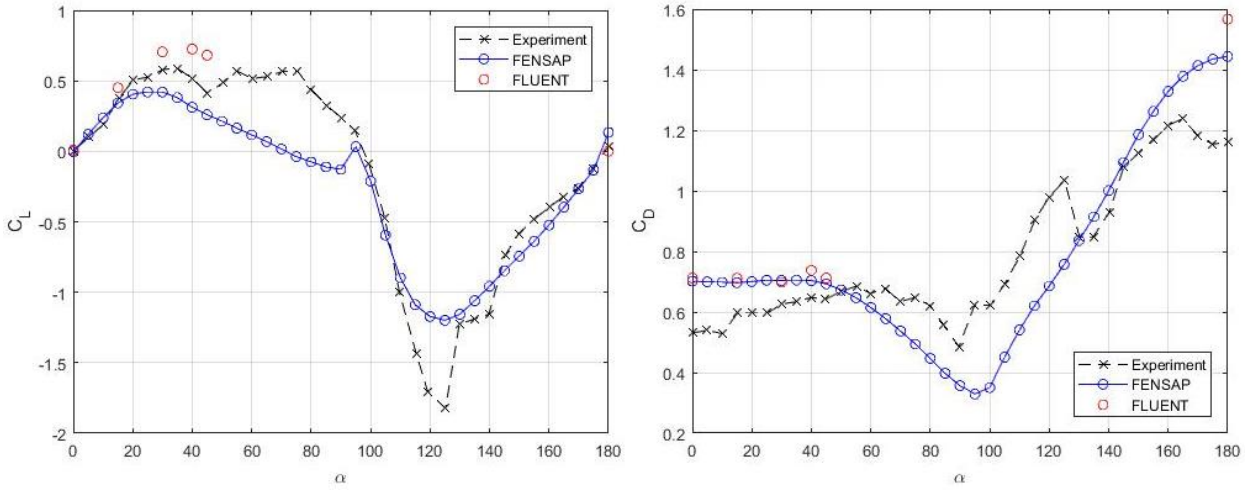

Figure 4-30 – Validation of aerodynamic characteristics of the semi-circular shell geometry – (Left) C_L comparison with experiments and Fluent. (Right) C_D comparison with experiments and Fluent.

4.2.4 Ice Trajectory in Hover – AERTS

4.2.4.1 Rectangular plate trajectories in Hover – Details

The aerodynamics database of the rectangular plate was used to perform trajectories on the AERTS flow field that was previously computed. The rectangular ice piece, sized according to the shedding results, was released at an azimuth angle of 90°. The spanwise, tangential and normal axes made at the point of release were used as the inertial reference frame axes. This is depicted in Figure 4-31.

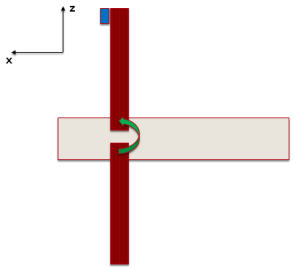

Figure 4-31 – Inertial reference frame of AERTS trajectory

At the point of release, the ice piece is travelling at the tip speed in the tangential direction (x-direction) as shown at t = 0 in Figure 4-32 – Left. The ice piece is released into a zone where the flow field is affected in all three directions as shown in Figure 4-32 – Right. This, together with the forces and moments experienced by the ice piece, induce velocities in the other two directions. Drastic changes in velocities are experienced by the ice piece initially as a result. However, the ice piece soon enters a zone where the flow field is almost zero as seen in Figure 4-33. The flow fields were updated at 30° intervals to save up on computation time.

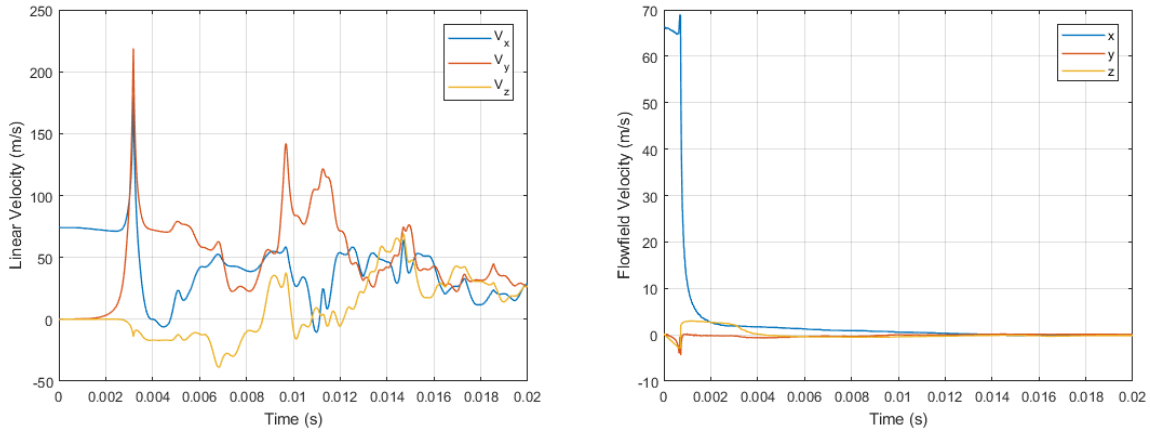

Figure 4-32 – Plate trajectory in hover – 0 – 0.02 s – (Left) Linear velocity vs Time. (Right) Flow field velocity vs Time.

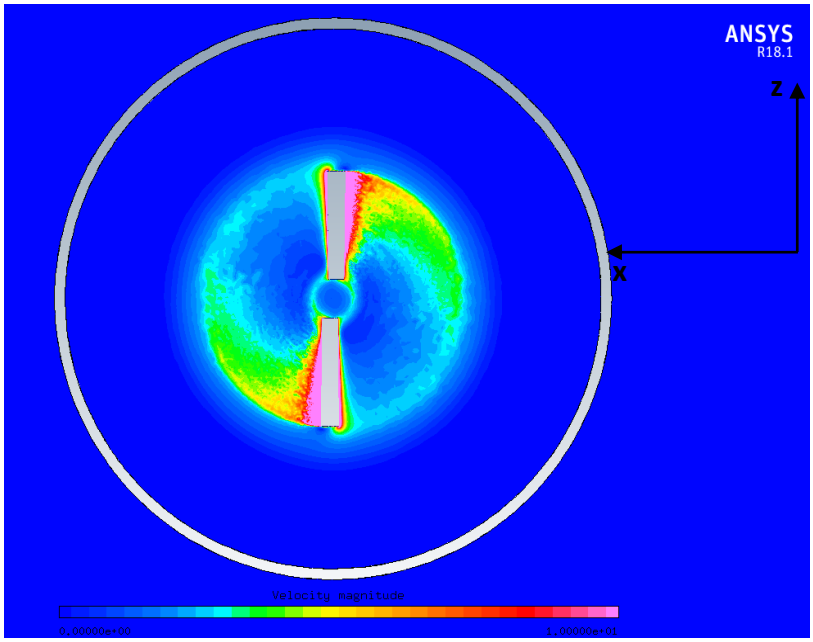

Figure 4-33 – Flow field at azimuth = 90°

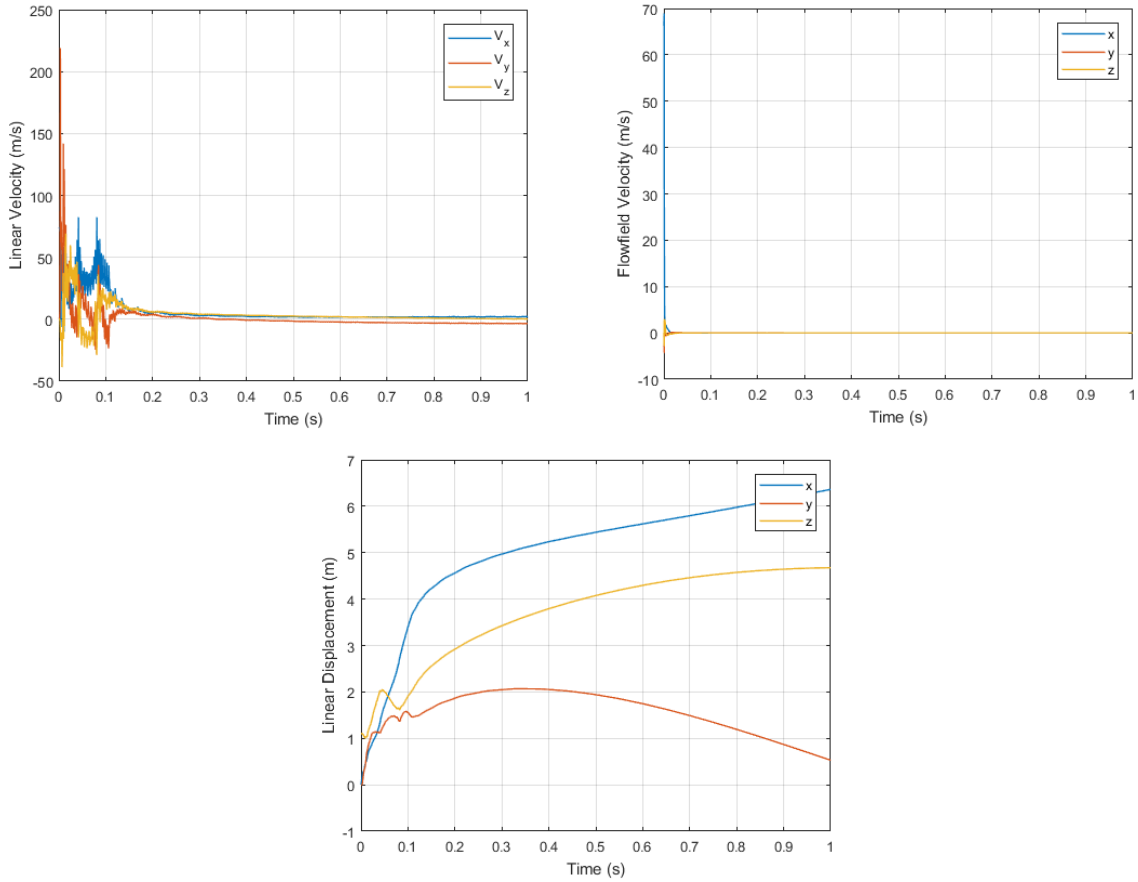

Figure 4-34 – Plate trajectory in hover – 0 – 1 s – (Top left) Linear velocity vs Time. (Top right) Flow field velocity vs Time. (Bottom) Linear Displacement vs Time.

Figure 4-34 illustrates the trajectory of the ice piece in the first second. After going through the intense fluctuations initially, the velocity of the ice piece in the x and z directions converge towards the still flow field velocity due to drag between the ice piece and the flow field. However, they still have very small magnitudes which leads to slight displacements in their respective directions. The velocity in the y-direction reaches terminal speed thus leading to the descending of the ice piece after its initial rise.

Figure 4-35 demonstrates the trajectory of the ice piece over 5 s. The ice piece reaches a steady-state condition with very slight velocities in all three directions.

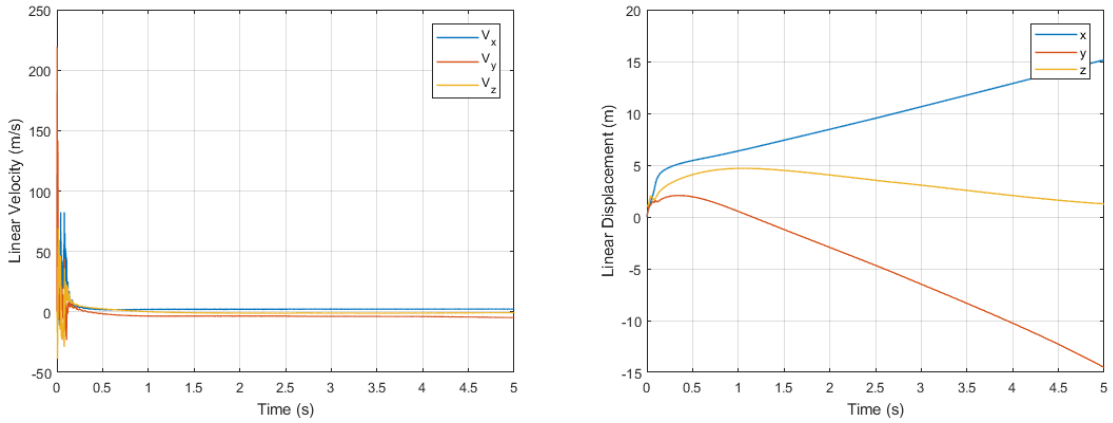

Figure 4-35 – Plate trajectory in hover – 0 – 5 s – (Left) Linear velocity vs Time. (Right) Linear Displacement vs Time.

The ice piece is initialized to zero angular velocity about all three axes as shown in Figure 4-36 – Left. However, when released into the flow field, the ice piece experiences moments acting on it due to its orientation. This results in the ice piece rotating about all three axes as shown in Figure 4-36 – Right. Like the linear motion, the angular motion is very noisy in the beginning.

However, during its trajectory, the ice piece eventually reaches a steady-state angular motion. Figure 4-37 illustrates this steady-state behavior in the final 0.5 s of the trajectory. Periodic changes in velocities which result in periodic changes in angular displacements can be seen. Figure 4-38 focuses on the final 0.05 s of the trajectory highlighting this periodicity. Since there is no rotational damping introduced, the periodicity continues.

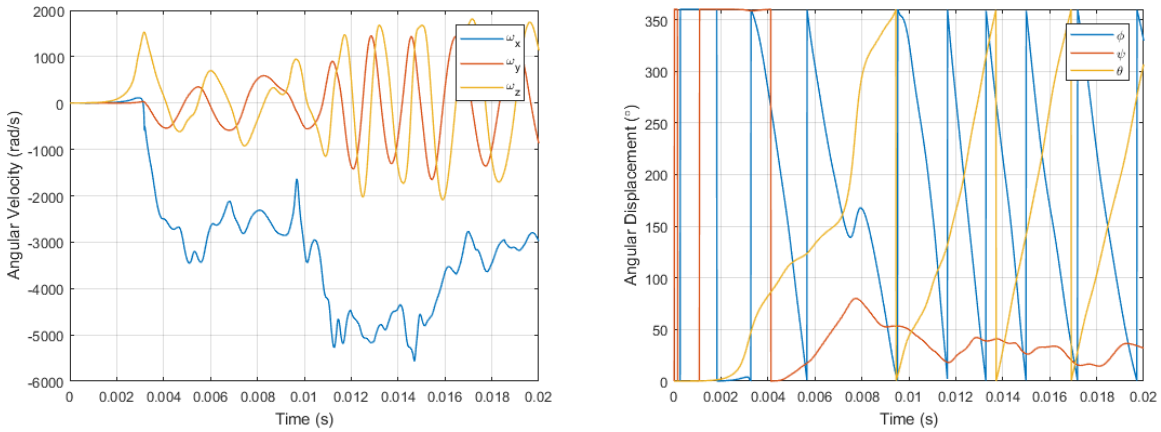

Figure 4-36 – Plate trajectory in hover – 0 – 0.02 s – (Left) Angular velocity vs Time. (Right) Angular Displacement vs Time.

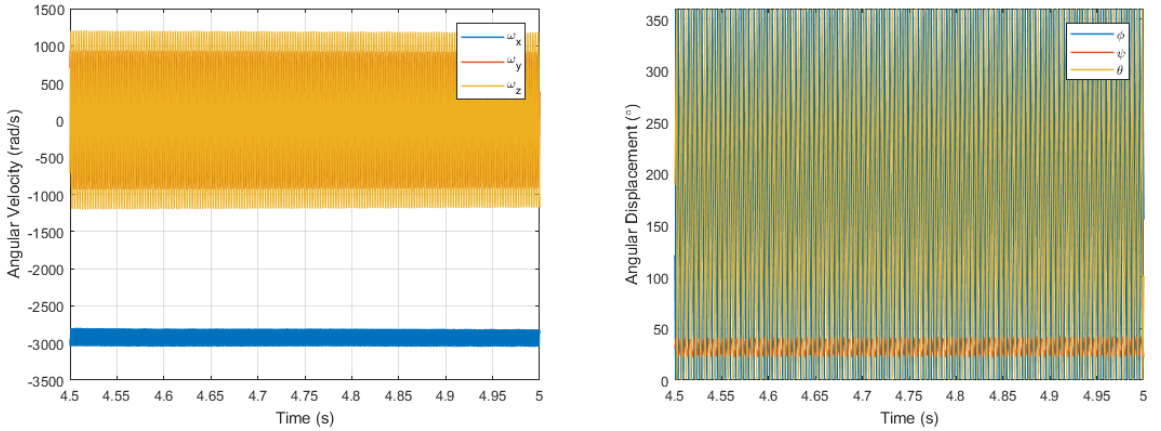

Figure 4-37 – Plate trajectory in hover – 4.5 – 5 s – (Left) Angular velocity vs Time. (Right) Angular Displacement vs Time.

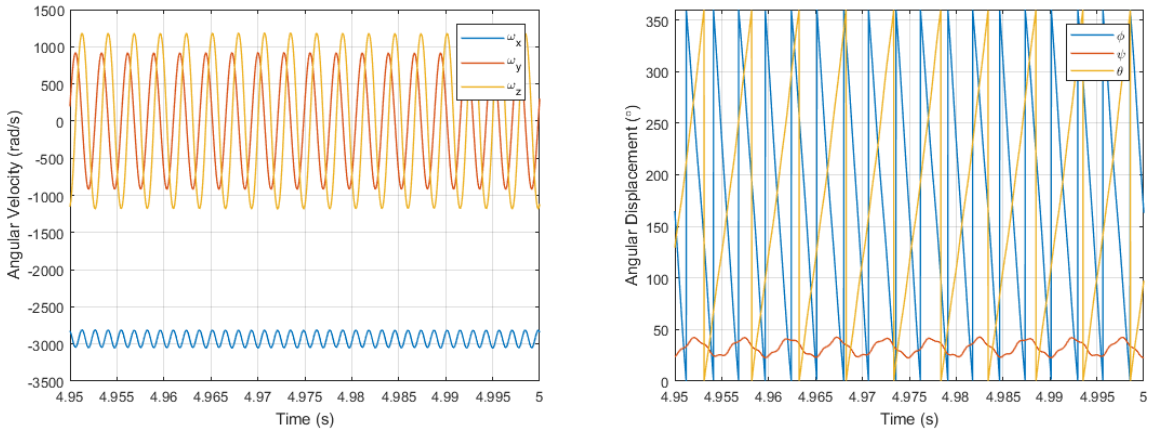

Figure 4-38 – Plate trajectory in hover – 4.95 – 5 s – (Left) Angular velocity vs Time. (Right) Angular Displacement vs Time.

4.2.4.2 Rectangular plate trajectories in Hover – Possible impact zones

The flow fields computed for the trajectory simulations only consisted of the two blades. Therefore, for a hover case, the flow field at steady-state at a particular azimuth angle is the flow field at azimuth = 0° rotated by the particular azimuth angle. For instance, the flow field at azimuth = 30°, is the flow field at azimuth = 0° rotated by 30°. For a trajectory in hover, this means that a trajectory at a particular azimuth can be found by rotating the trajectory at azimuth = 0° by the respective azimuth angle.

In order to model a more realistic scenario, a fuselage and tail rotor were made up to analyze the possible impact zones for this hover case. Figure 4-39 - Figure 4-45 illustrate the trajectories of the ice piece released at 30° intervals. Due to the initial rise in the plate trajectory, the rectangular ice piece is found to miss all components of the model helicopter at all release points.

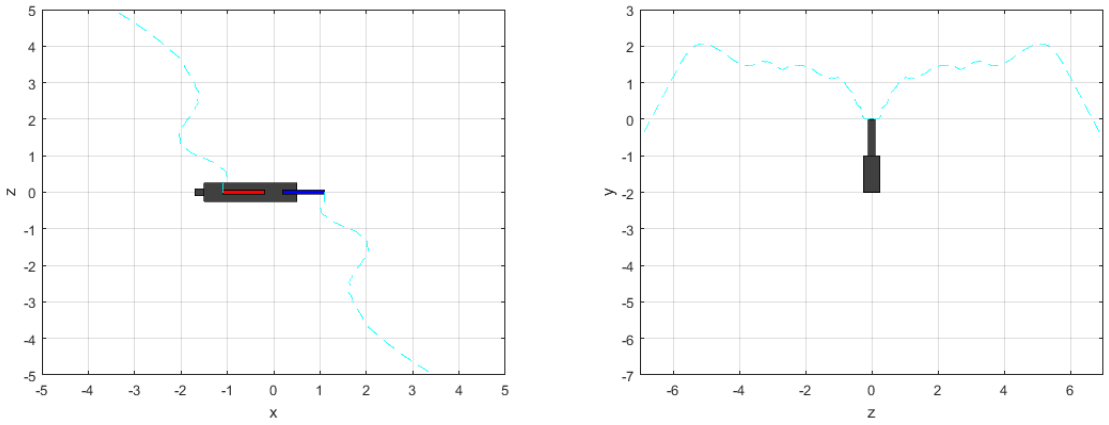

Figure 4-39 – AERTS plate trajectories at azimuth release = 0° & 180° - (Left) Top view. (Right) Front view.

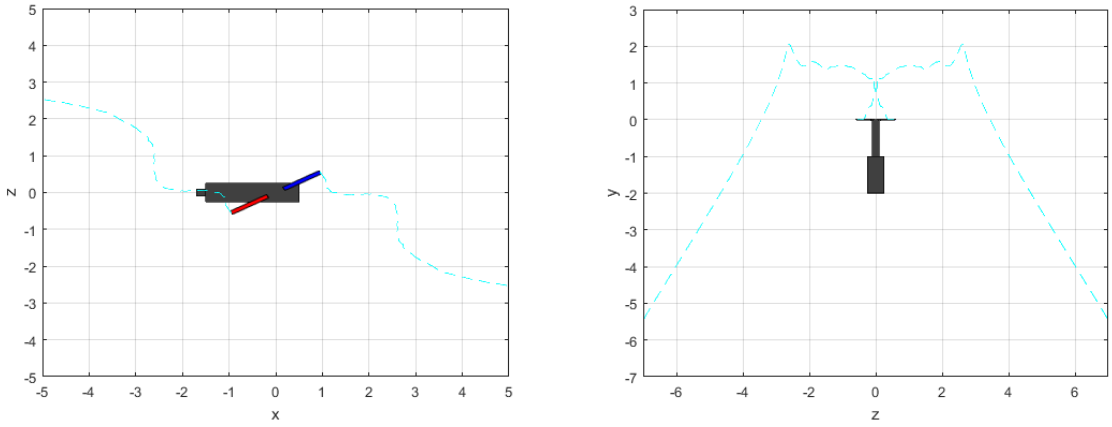

Figure 4-40 – AERTS plate trajectories at azimuth release = 30° & 210° - (Left) Top view. (Right) Front view.

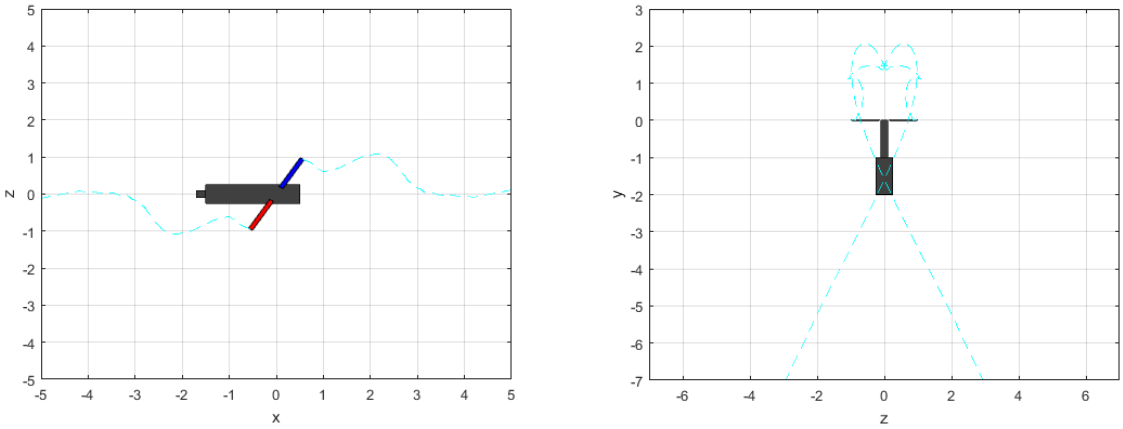

Figure 4-41 – AERTS plate trajectories at azimuth release = 60° & 240° - (Left) Top view. (Right) Front view.

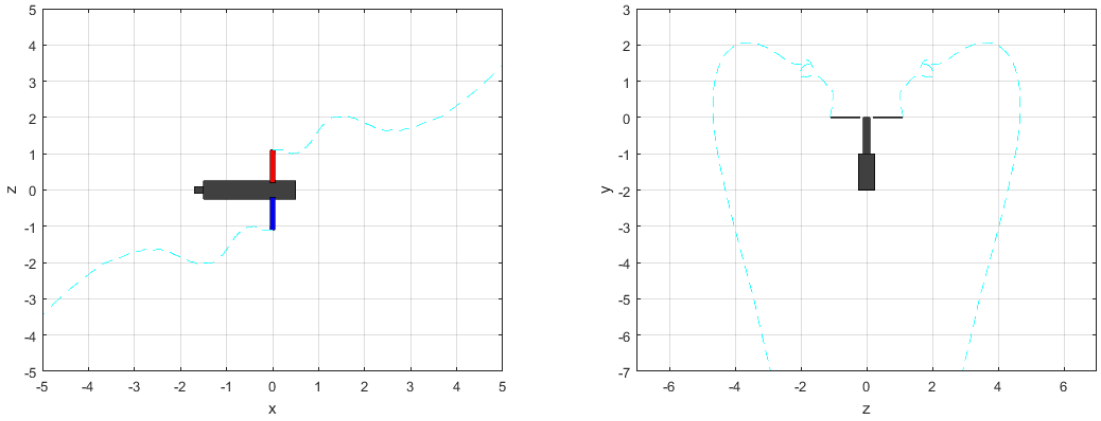

Figure 4-42 – AERTS plate trajectories at azimuth release = 90° & 270° - (Left) Top view. (Right) Front view.

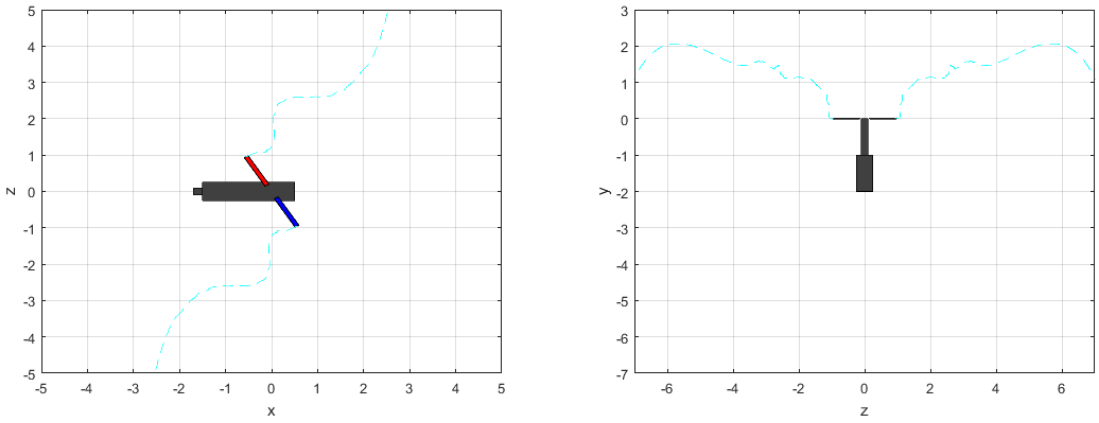

Figure 4-43 – AERTS plate trajectories at azimuth release = 120° & 300° - (Left) Top view. (Right) Front view.

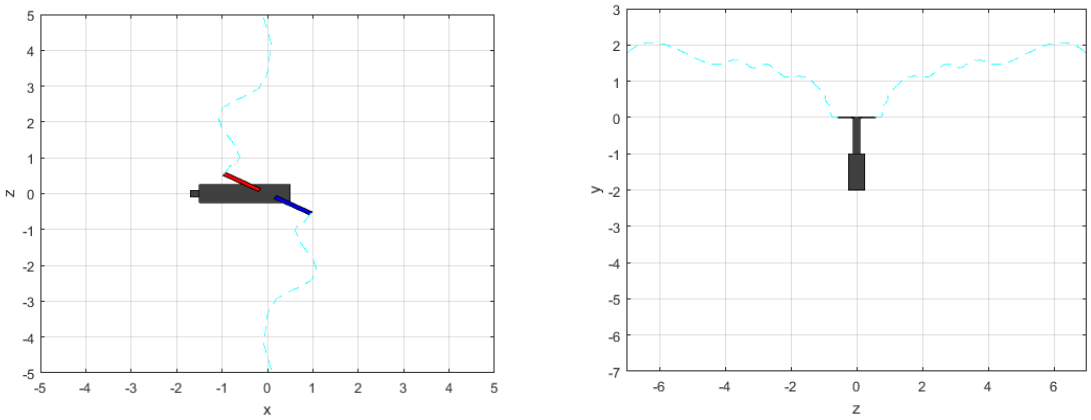

Figure 4-44 – AERTS plate trajectories at azimuth release = 150° & 330° - (Left) Top view. (Right) Front view.

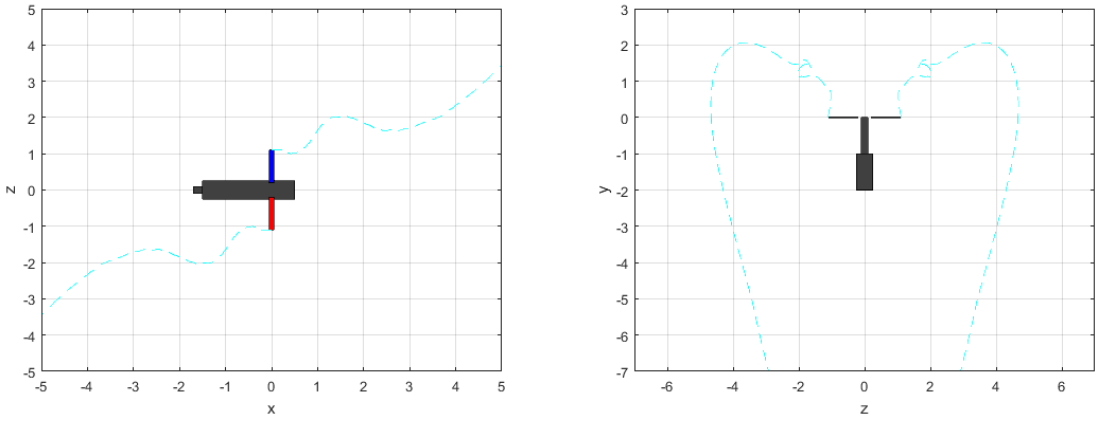

Figure 4-45 – AERTS plate trajectories at azimuth release = 180° & 360° - (Left) Top view. (Right) Front view.

4.2.4.3 Semi Circular Shell trajectories in Hover – Details

Similar to the plate's trajectory, a full trajectory simulation of the SCS was conducted to illustrate the capability of the code to handle different geometries successfully. As in the detailed plate trajectory case, the SCS ice piece is released into the flow field at azimuth = 0° at the tip speed of 74 m/s. As seen in the plate's trajectory, the initial trajectory is very noisy leading to fluctuating ice velocities illustrated in Figure 4-46 – Left. However, unlike the plate's trajectory, the unsteady behaviour of the ice piece lasts a longer time. This is due to the more complex aerodynamics of the SCS. Nevertheless, the ice piece soon reaches the steady section of the hover flow field as shown in Figure 4-46 – Right. Similar to the plate's trajectory, the ice piece reaches the steady flow field velocity in the x and z directions and terminal velocity in the y-direction as demonstrated in Figure 4-47 – Left. The resulting displacement is depicted n Figure 4-47 – Right.

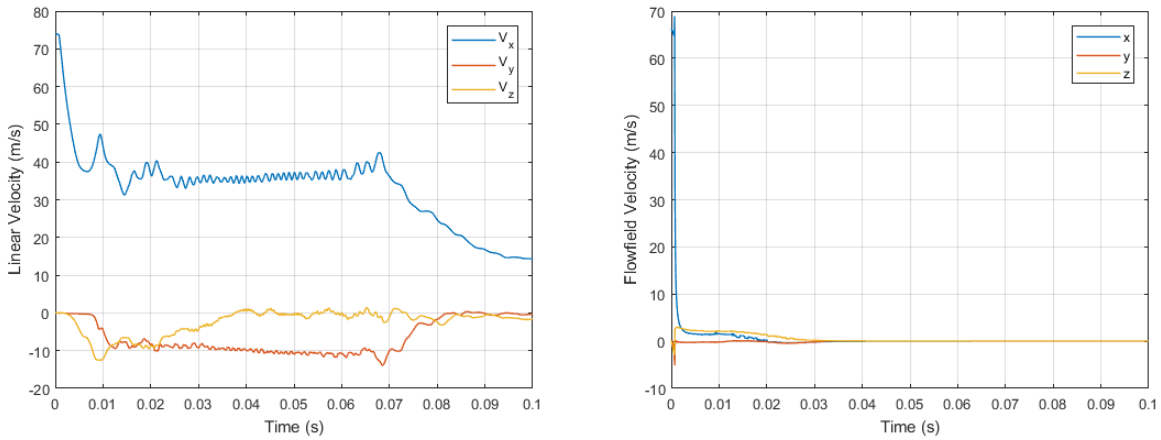

Figure 4-46 – SCS trajectory in hover – 0 – 0.1 s – (Left) Linear velocity vs Time. (Right) Flow field velocity vs Time.

The angular velocities are initialized to zero. However, due to the induced moments on the ice piece, angular motion develops. This is demonstrated in Figure 4-48 during the initial part of the trajectory. Following the transient section of the trajectory, the ice piece eventually attains a steady-state behavior. Figure 4-49 illustrates this steady-state characteristic of the trajectory. Like the plate's trajectory, the SCS ice piece's angular motion becomes periodic which results in periodic angular changes in angular velocities and displacements.

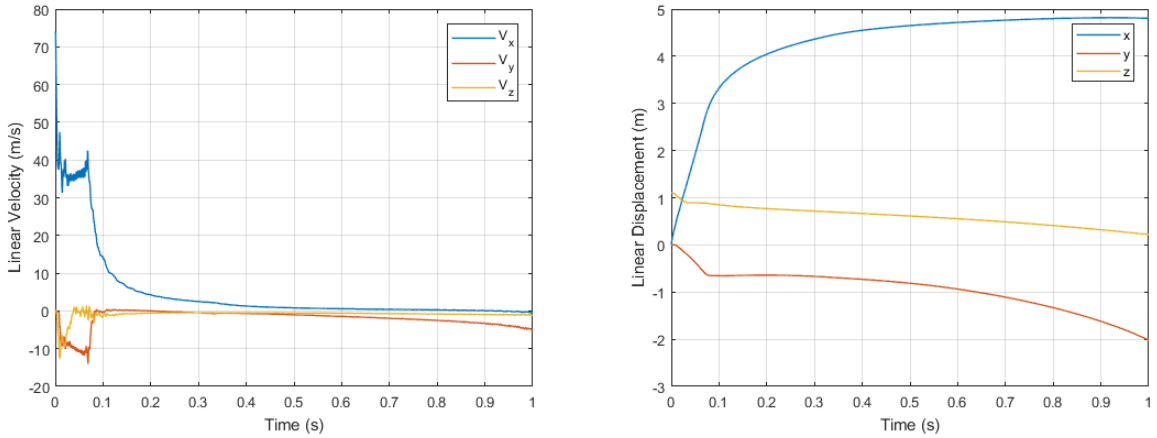

Figure 4-47 – SCS trajectory in hover – 0 – 1 s – (Left) Linear velocity vs Time. (Right) Linear displacement vs Time.

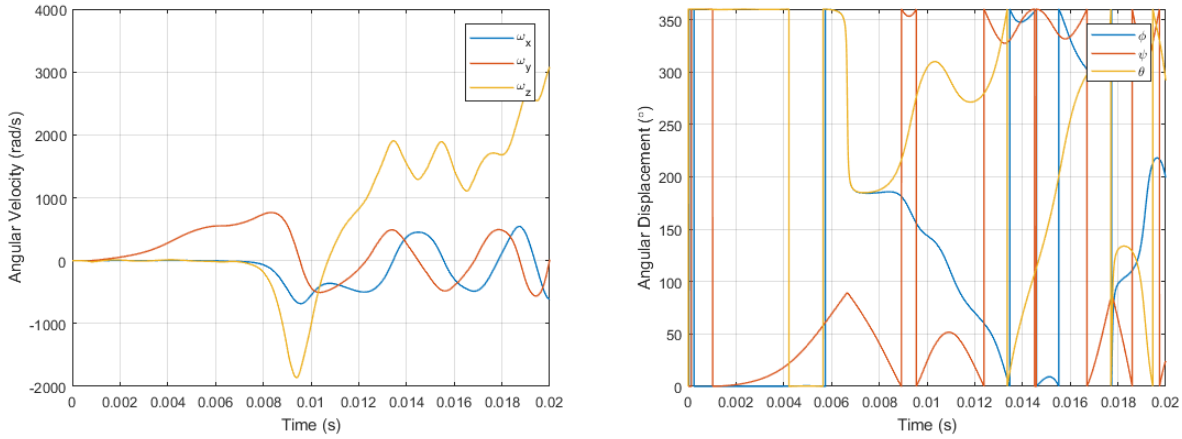

Figure 4-48 – SCS trajectory in hover – 0 – 0.02 s – (Left) Angular velocity vs Time. (Right) Angular displacement vs Time.

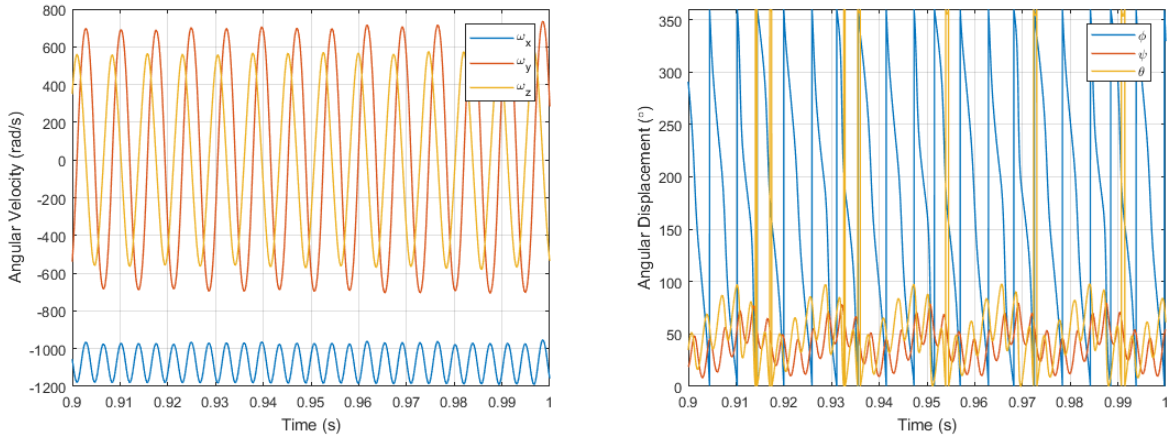

Figure 4-49 – SCS trajectory in hover – 0.9 – 1 s – (Left) Angular velocity vs Time. (Right) Angular displacement vs Time.

4.2.4.4 Semi Circular Shell trajectories in Hover – Possible impact zones

A similar analysis to that conducted with the plate trajectories was carried out using the aerodynamics of the SCS geometry. Again, this analysis was conducted at one azimuth angle and then mapped around the rotor. Figure 4-50 - Figure 4-52 illustrate the impact zones of this hover case at 30° intervals.

Significant differences can be seen in the paths of the SCS in comparison to that of the plate's. Firstly, the SCS's path is seen to be steadier with only little deviation from the initial release direction. From the previous section, the ice piece is seen to descend immediately when released in to the flow field. Hence, unlike the plate trajectories in hover, the likelihood of the ice impacting the fuselage or tail rotor increases. At release points 120° to 150° shown in Figure 4-50 – Right and Figure 4-51 – Left highlight this. At all other release points in hover, the SCS ice shape is viewed to miss all components of the AERTS model helicopter.

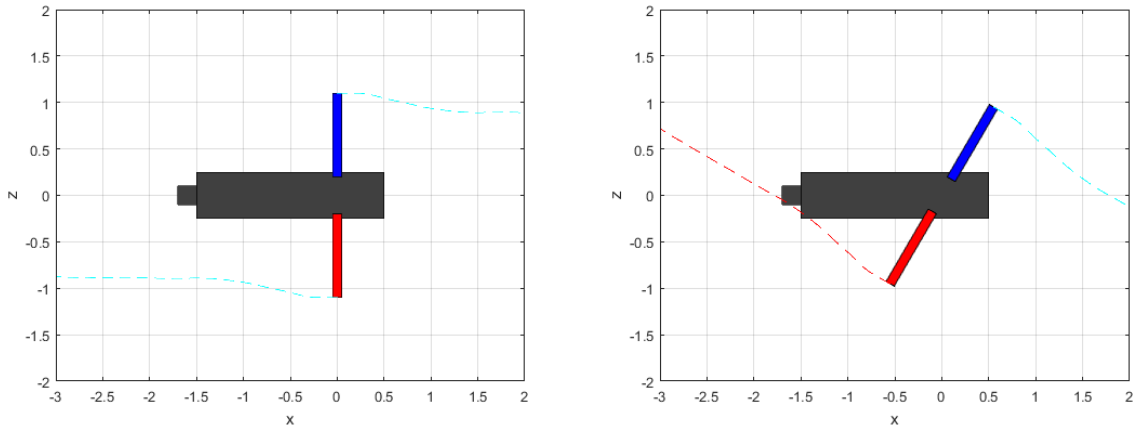

Figure 4-50 – AERTS SCS trajectories at azimuth release = 90° & 270° (Left). 120° & 300° (Right).

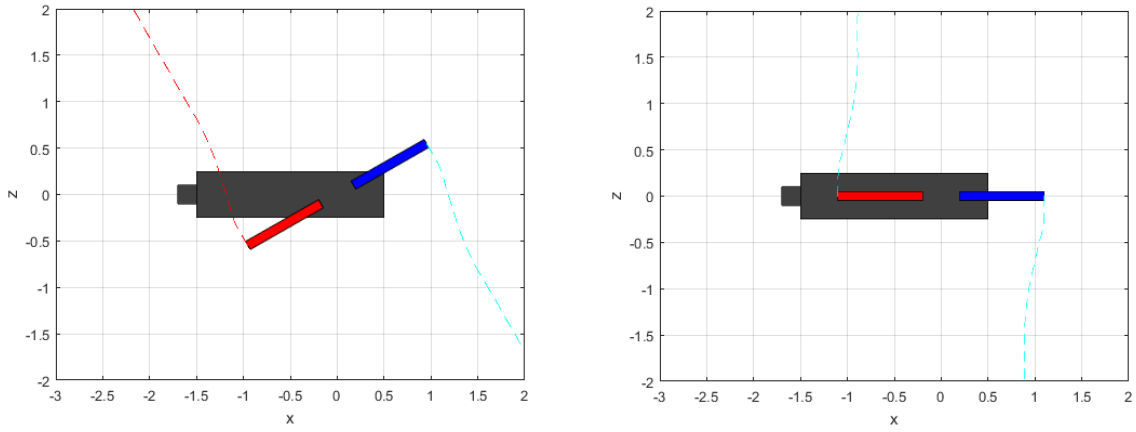

Figure 4-51 – AERTS SCS trajectories at azimuth release = 150° & 330° (Left). 180° & 0° (Right).

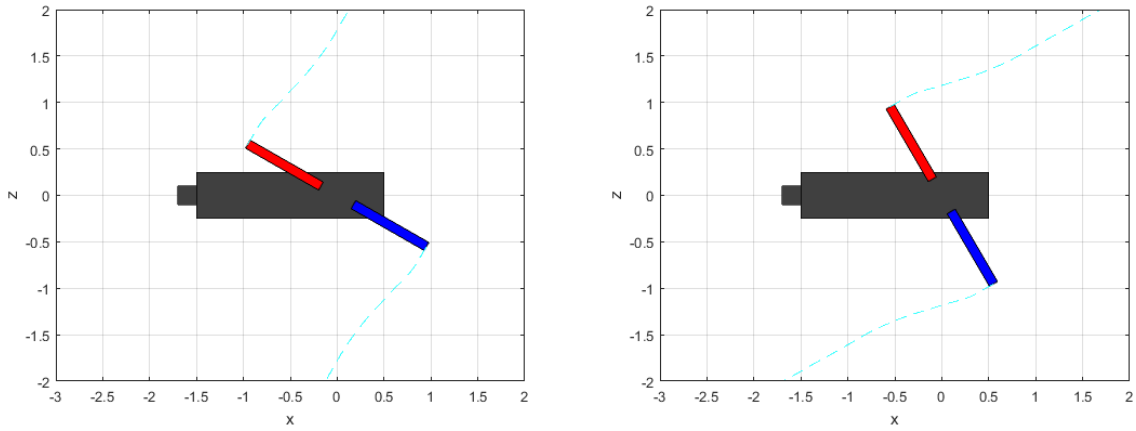

Figure 4-52 – AERTS SCS trajectories at azimuth release = 210° & 30° (Left). 240° & 60° (Right).

4.2.5 Ice trajectory in Forward Flight – Georgia Tech.

4.2.5.1 Rectangular plate trajectories in Forward Flight – Details

The velocity flow field of the Georgia Tech case was more complex than the AERTS case. The velocity flow field was continuously updated every 15° change in the blade's azimuth angle. Since the mesh size was smaller than the AERTS case, the reading of the grid and solution files was achieved inexpensively. Figure 4-53 illustrates the reference axes utilized for this case. Figure 4-54 – Figure 4-58 explain the trajectory of a rectangular ice piece in forward flight.

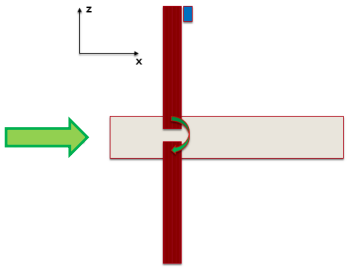

Figure 4-53 – Inertial reference frame of Georgia Tech trajectory

Like the hover case, the ice piece is thrown into a zone with significant velocity oscillations as shown in Figure 4-54 – Right. For instance, a spike in flow field velocity is experienced in the ice piece's trajectory in the y-direction. This together with the slight upward velocity due to the lateral shaft angle of the Georgia Tech case causes a sudden rise in the ice piece's y-velocity can be seen. Unlike the hover case, significant flow field velocities in all three directions are seen, leading to the complex variations of the ice piece's velocity during its initial trajectory.

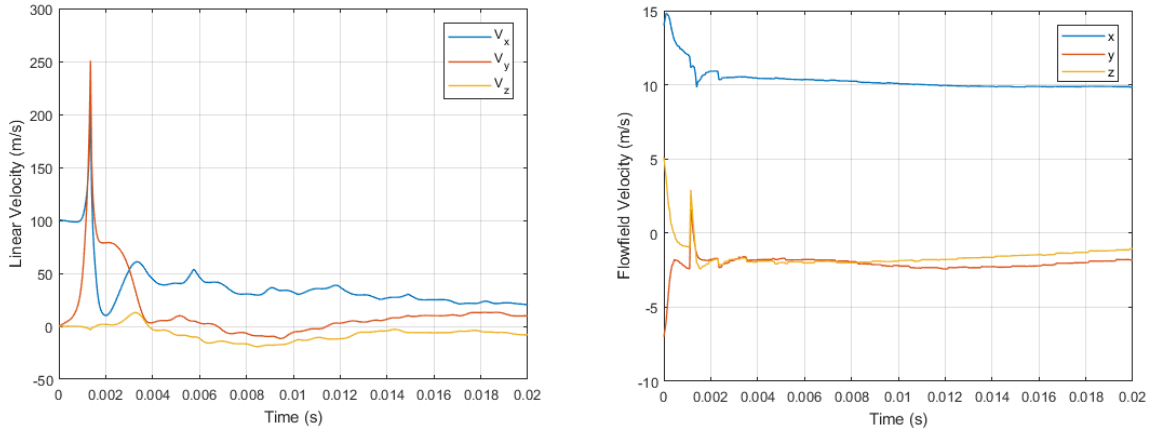

Figure 4-54 – Plate trajectory in forward flight – 0 – 0.02 s – (Left) Linear velocity vs Time. (Right) Flow field velocity vs Time.

After 0.2 s of trajectory, the ice piece reaches a zone where the flow field hardly changes. Since this simulation is done with the rotor-fuselage system stationary and the air moving at the forward flight speed of 10 m/s, the steady flow field velocity in the x-direction is 10 m/s. Subsequently, the displacements shown in Figure 4-55 are relative to the position of the helicopter.

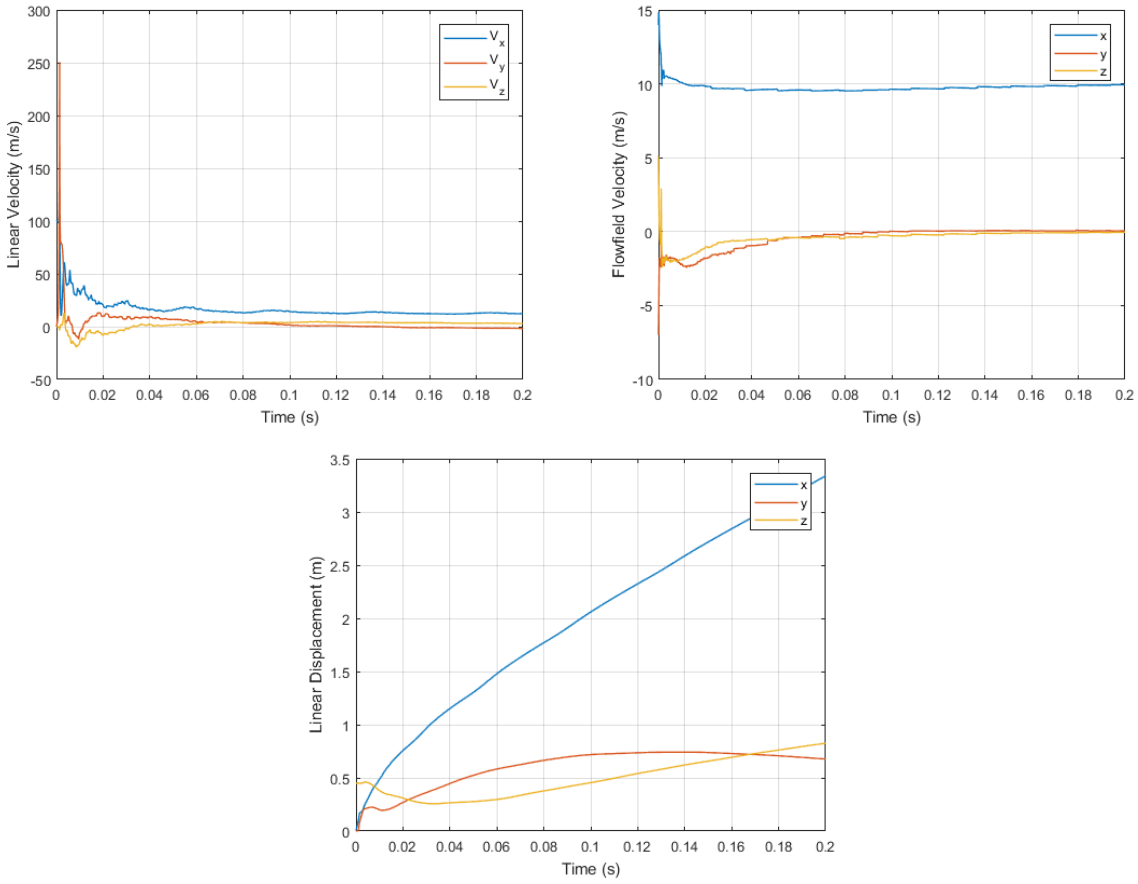

Figure 4-55 – Plate trajectory in forward flight – 0 – 0.2 s – (Top left) Linear velocity vs Time. (Top right) Flow field velocity vs Time. (Bottom) Linear Displacement vs Time.

Figure 4-56 illustrates the trajectory of rectangular plate ice piece over 2 s. The ice piece eventually reaches a steady-state behavior with minor velocity fluctuations in the x and z directions. Terminal velocity is reached in the y-direction leading to the descent in the ice piece.

Like the hover case, the angular velocities of the ice piece are initialized to zero about all three axes. However, due to the initial orientation of the ice piece, moments are induced about all three axes leading to the variation in angular displacements as shown in Figure 4-57. The ice

piece eventually reaches steady-state changes in angular velocities and displacements as illustrated in Figure 4-58.

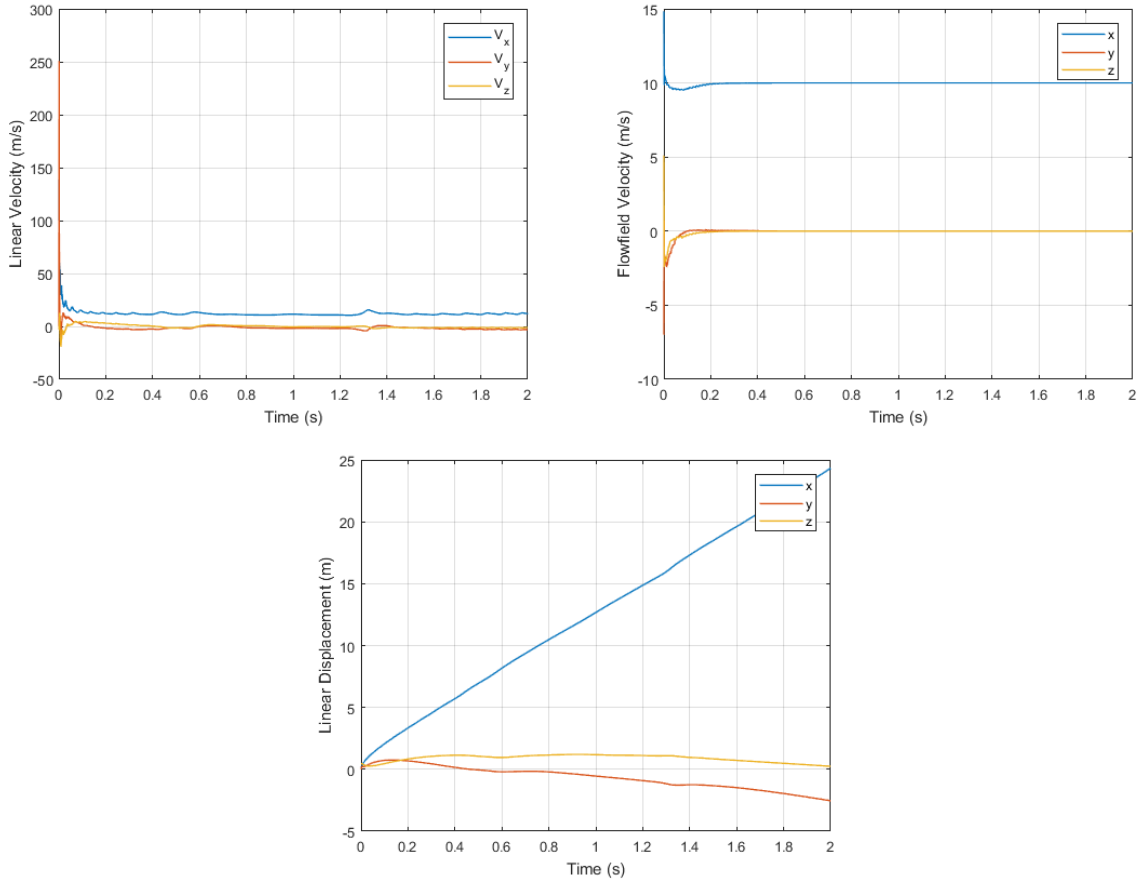

Figure 4-56 – Plate trajectory in forward flight – 0 – 2 s – (Top left) Linear velocity vs Time. (Top right) Flow field velocity vs Time. (Bottom) Linear Displacement vs Time.

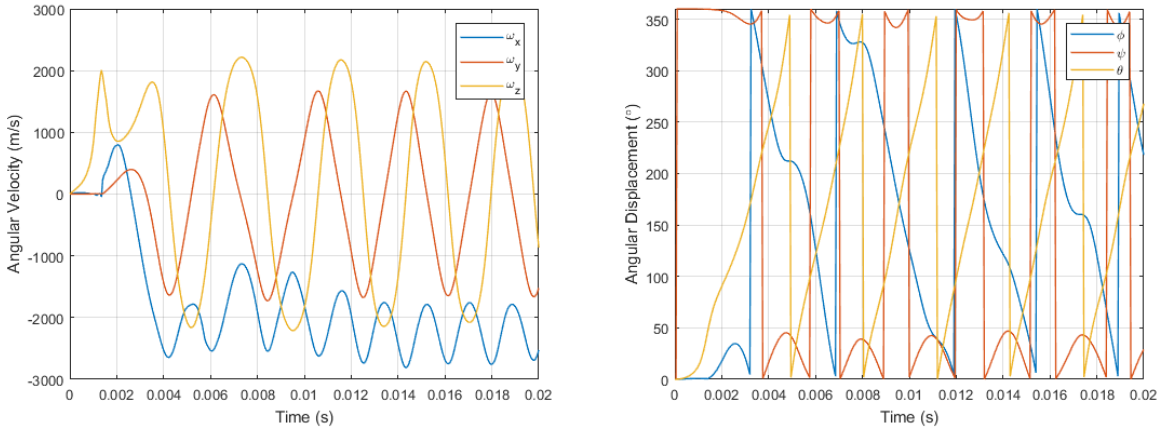

Figure 4-57 – Plate trajectory in forward flight – 0 – 0.02 s – (Left) Angular velocity vs Time. (Right) Angular Displacement vs Time.

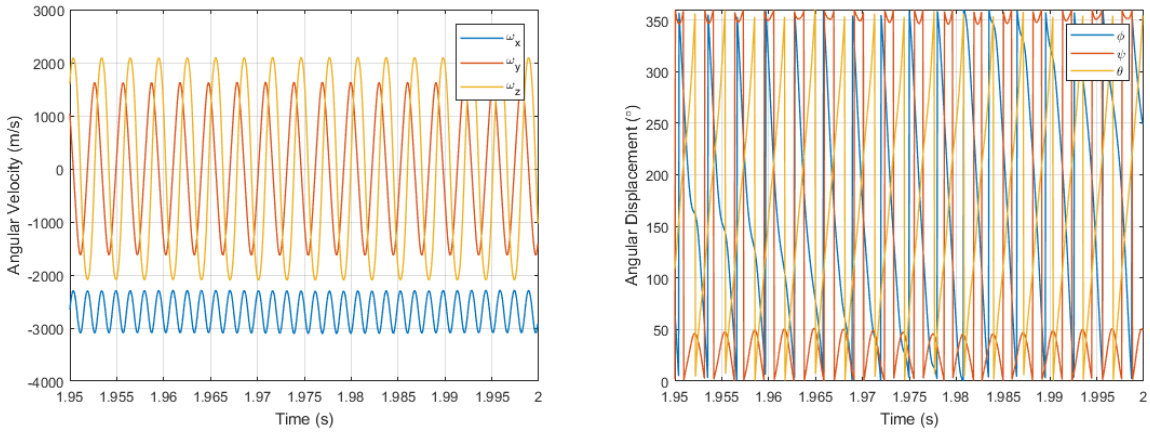

Figure 4-58 – Plate trajectory in forward flight – 1.95 – 2 s – (Left) Angular velocity vs Time. (Right) Angular Displacement vs Time.

4.2.5.2 Rectangular plate trajectories in Forward Flight – Possible Impact Zones

Unlike the hover case, where the trajectory from one azimuth release can be mapped at all azimuth releases points, the trajectories in forward flight needed to be conducted independently. Due to the forward velocity vector the environment experienced by the blades at every azimuth angle varies. Hence trajectories needed to be evaluated individually. Trajectories were conducted at 30° release intervals and the flow field was continuously updated at 30° intervals. This component was easily parallelizable and therefore was carried out very efficiently. Figure 4-59 - Figure 4-64 illustrate these trajectories. Note that the Georgia Tech case consists only of a rotor and fuselage. A tail rotor was modelled to investigate the possibilities of being hit.

In the first set of release points (270°, 300°, 330°, 0°) the ice piece rises slightly due to the lateral shaft angle of the Georgia Tech rotor. The effect of the forward velocity is seen to displace the ice piece in the longitudinal direction (x-axis). Due to these two effects, shed-ice released at 270°, 330° and 0° results in the ice piece missing the tail or fuselage of the helicopter. However, at an azimuth release point of 300°, the ice plate has a likely chance of impacting the tail rotor.

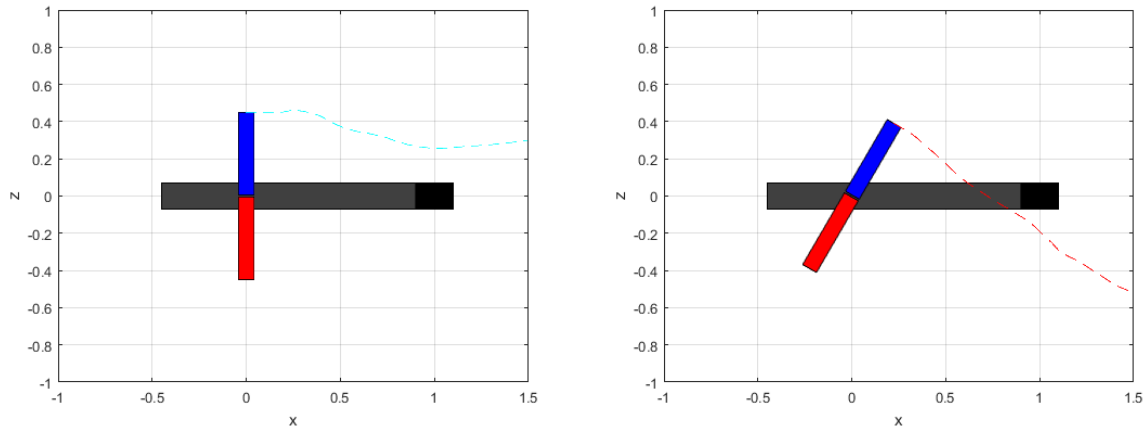

Figure 4-59 – Georgia Tech plate trajectories at azimuth release = 270° (Left) & 300° (Right)

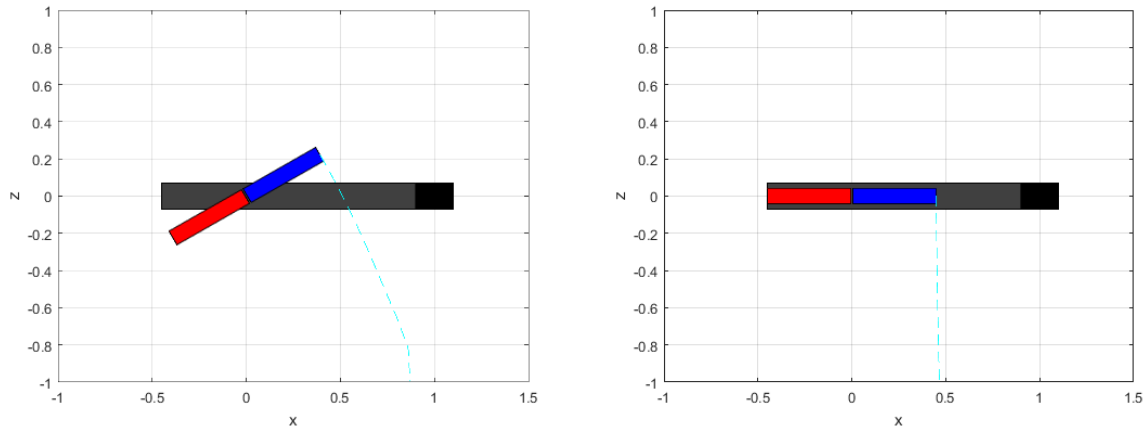

Figure 4-60 – Georgia Tech plate trajectories at azimuth release = 330° (Left) & 0° (Right)

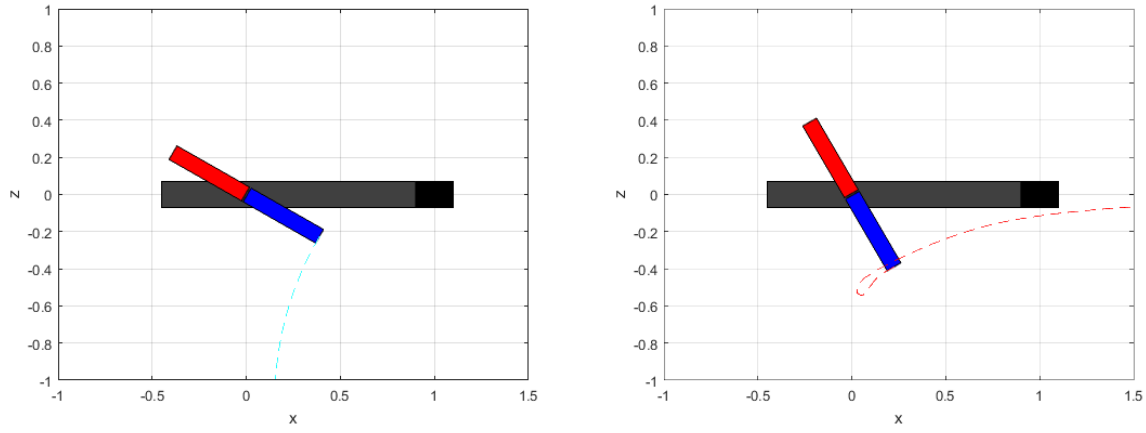

Figure 4-61 – Georgia Tech plate trajectories at azimuth release = 30° (Left) & 60° (Right)

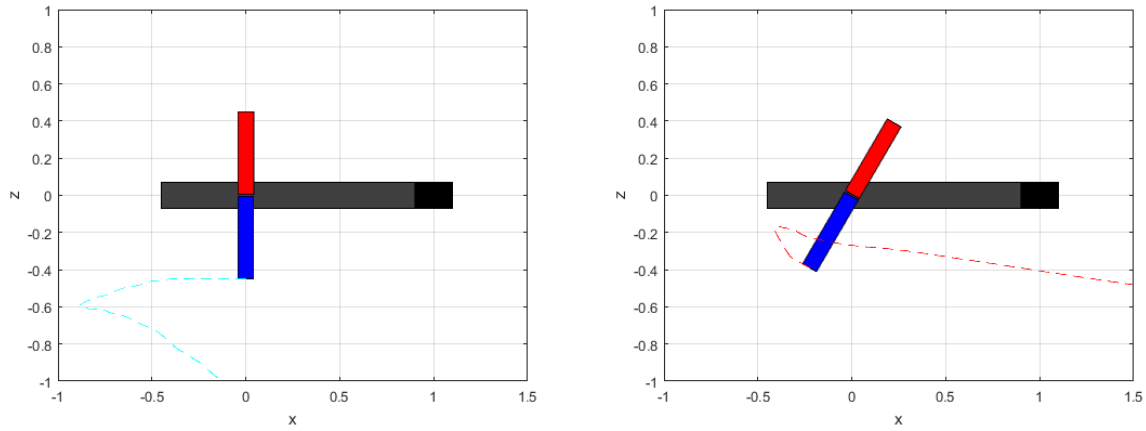

Figure 4-62 – Georgia Tech plate trajectories at azimuth release = 90° (Left) & 120° (Right)

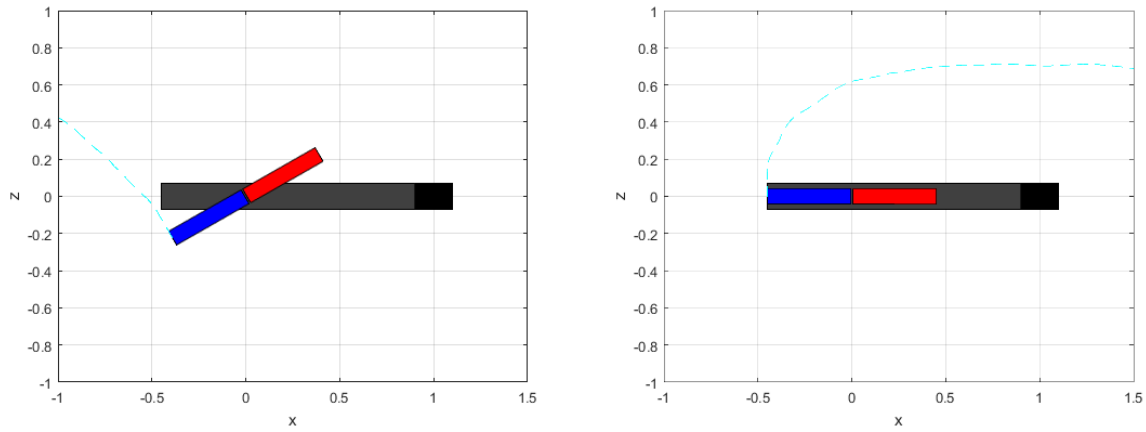

Figure 4-63 – Georgia Tech plate trajectories at azimuth release = 150° (Left) & 180° (Right)

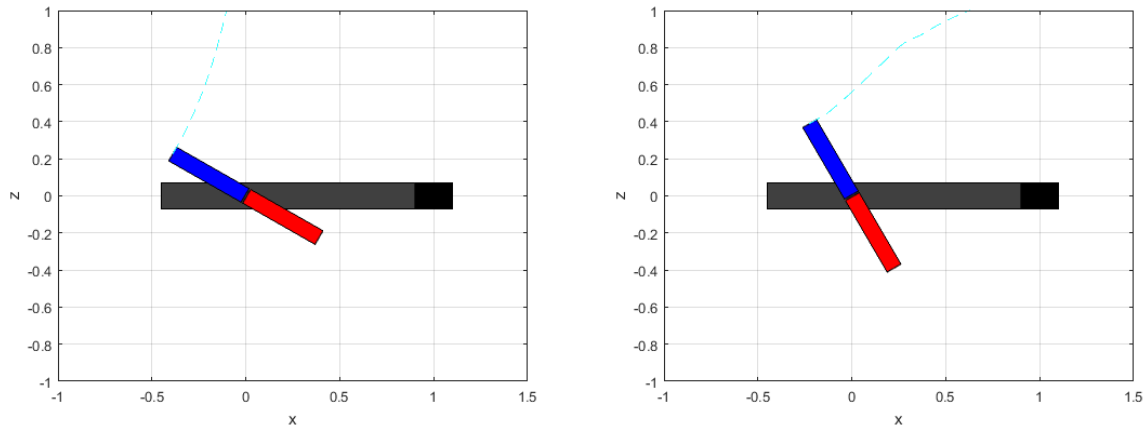

Figure 4-64 – Georgia Tech plate trajectories at azimuth release = 210° (Left) & 240° (Right)

In the next quadrant of release points, the ice piece is observed to travel away from the blades in the lateral direction (z-direction) when released at 30° and 90°. The impact of the

forward velocity becomes substantial at release points 60° and 90° as seen by their respective trajectories. The ice piece is thrown in front of the helicopter but is soon caught up with. Since the lateral shaft angle contributes to an immediate descent in the ice piece in these trajectories, this could lead to the ice impacting the other blade, fuselage or the tail as shown in Figure 4-61 (Right).

The significance of the forward flight velocity is further highlighted in release points 120° - 240° where the ice piece is driven in the +x direction. Once again, when released at 120° the ice is viewed to impact the helicopter. However, at release points 180° - 240° it can be considered to be the safest release points as the ice is thrown in the lateral direction and driven away from the helicopter.

4.2.5.3 Semi-Circular Shell trajectories in Forward Flight – Details

SCS trajectories were experimented on the Georgia Tech case to identify the differences in paths compared to the rectangular plate trajectories. A release point of azimuth = 90° was chosen to explain the details of the trajectory as it demonstrates the capability of the code to handle complex changes in flow field. When released in front of the helicopter, the longitudinal velocity of the ice piece is in the opposite direction of the flow field's forward velocity direction. This is illustrated in Figure 4-65 (Left) which highlights the initial trajectory. The ice piece has a (-) x-velocity initially. This is soon reversed as the ice piece is displaced behind the helicopter. Following the drastic changes in velocities, the ice piece reaches a region of steady flow velocity very soon as seen in Figure 4-65 (Right). The ice piece's velocity soon converges to the flow field velocity as shown in Figure 4-66. The change in x-velocity direction shows that the ice piece that is initially launched in front of the helicopter is soon caught up with. The continuous increase in x-displacement illustrates that the helicopter in forward velocity is moving further away from the ice piece's location.

As in the previous cases, the ice fragment's angular velocities are initialized to zero. However, the moments experienced by the ice piece induce angular motion as shown in Figure 4-67. Nevertheless, the ice piece soon reaches a steady-state angular motion as illustrated in the last 0.05 s of the simulation in Figure 4-68. Figure 4-69 focuses on the final 0.005 s of the trajectory to highlight the periodic angular motion.

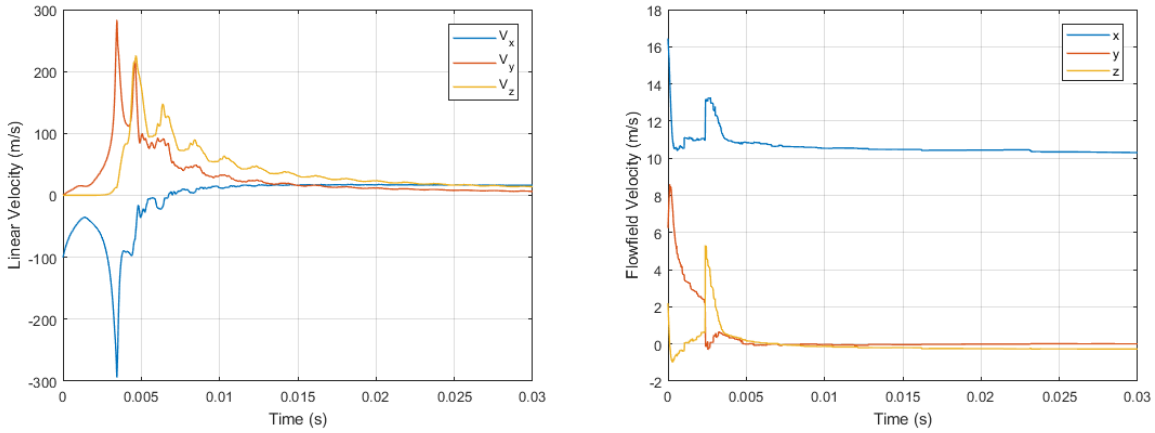

Figure 4-65 – SCS trajectory in forward flight – 0 – 0.03 s – (Left) Linear velocity vs Time. (Right) Flow field velocity vs Time.

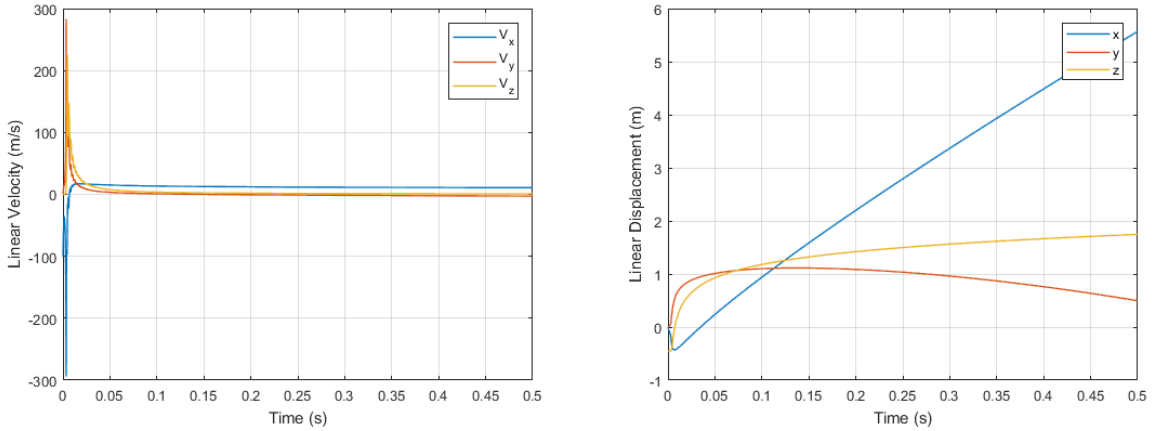

Figure 4-66 – SCS trajectory in forward flight – 0 – 0.5 s – (Left) Linear velocity vs Time. (Right) Linear Displacement vs Time.

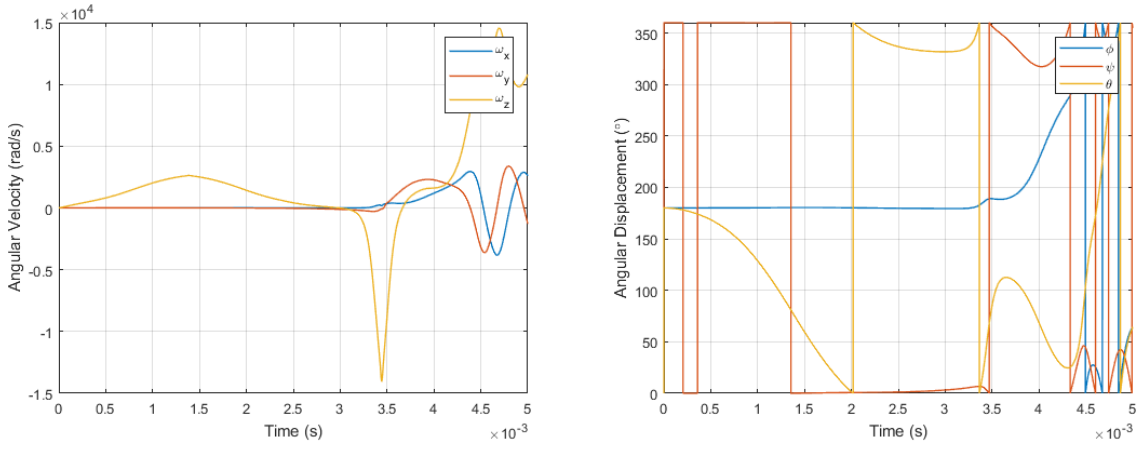

Figure 4-67 – SCS trajectory in forward flight – 0 – 0.005 s – (Left) Angular velocity vs Time. (Right) Angular Displacement vs Time.

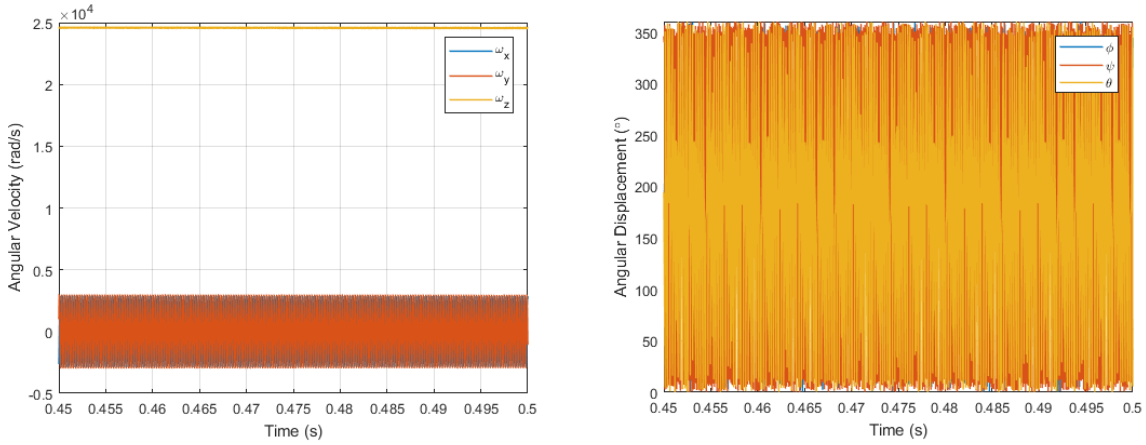

Figure 4-68 – SCS trajectory in forward flight – 0.45 – 0.5 s – (Left) Angular velocity vs Time. (Right) Angular Displacement vs Time.

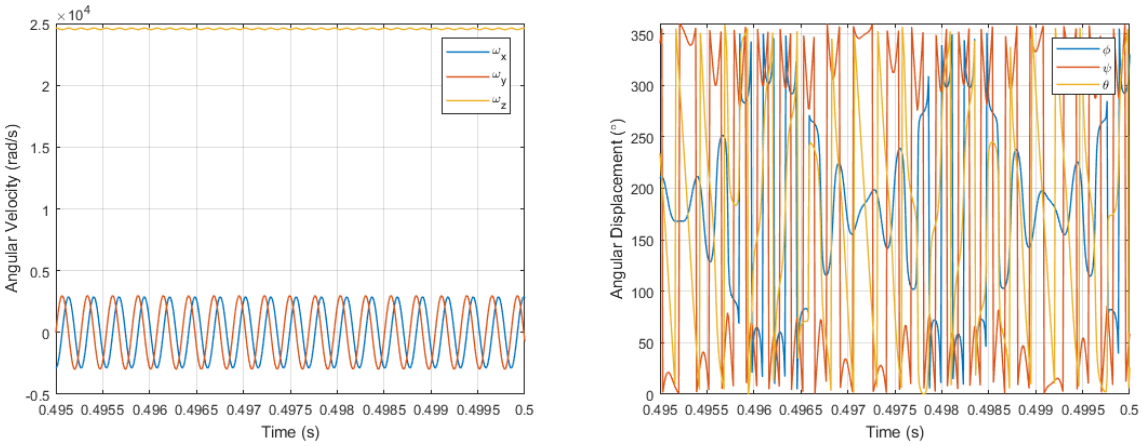

Figure 4-69 – SCS trajectory in forward flight – 0.495 – 0.5 s – (Left) Angular velocity vs Time. (Right) Angular Displacement vs Time.

4.2.5.4 Semi Circular Shell trajectories in Forward Flight – Possible Impact Zones

The possible impact zones in forward flight were analyzed using the SCS geometry to investigate the differences in impacts from the rectangular plate geometry. Trajectories were simulated at 60° release point intervals. The rotor flow field was continuously updated every 30°. Similar to what was observed in the plate trajectories in forward flight, the SCS geometry impacts the fuselage at similar release points. The SCS fragment is detected to impact the fuselage when released at 90°, 150° and 330°azimuth angles. Unlike the plate trajectories, the SCS geometry is found to travel further when thrown in front before the helicopter catches up to it. This is

interesting as it reduces the likelihood of collision because it gives more time for the ice piece to deviate from the path of the helicopter.

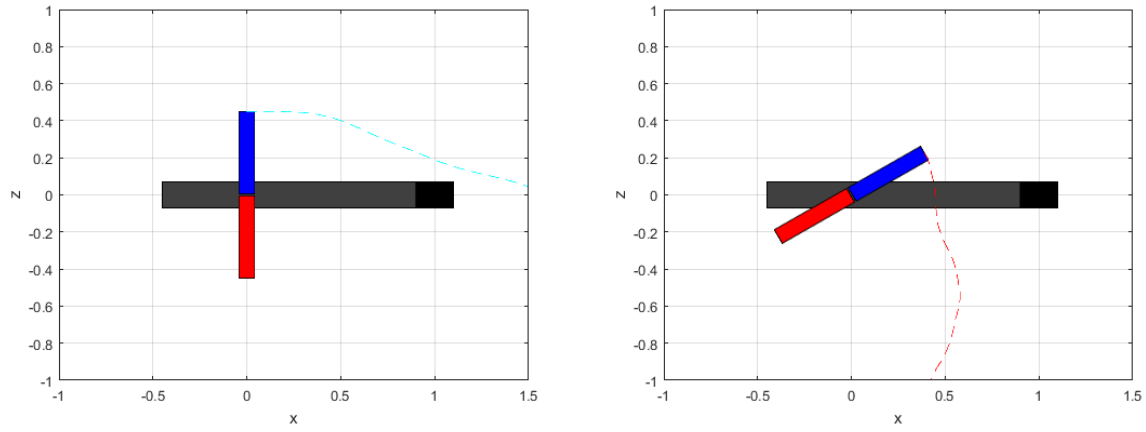

Figure 4-70 – Georgia Tech SCS trajectories at azimuth release = 270° (Left) & 330° (Right)

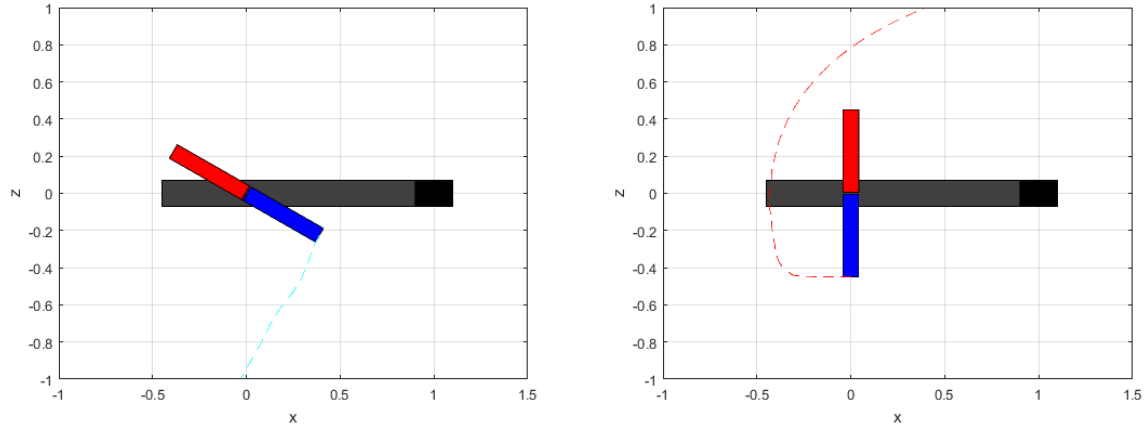

Figure 4-71 – Georgia Tech SCS trajectories at azimuth release = 30° (Left) & 90° (Right)

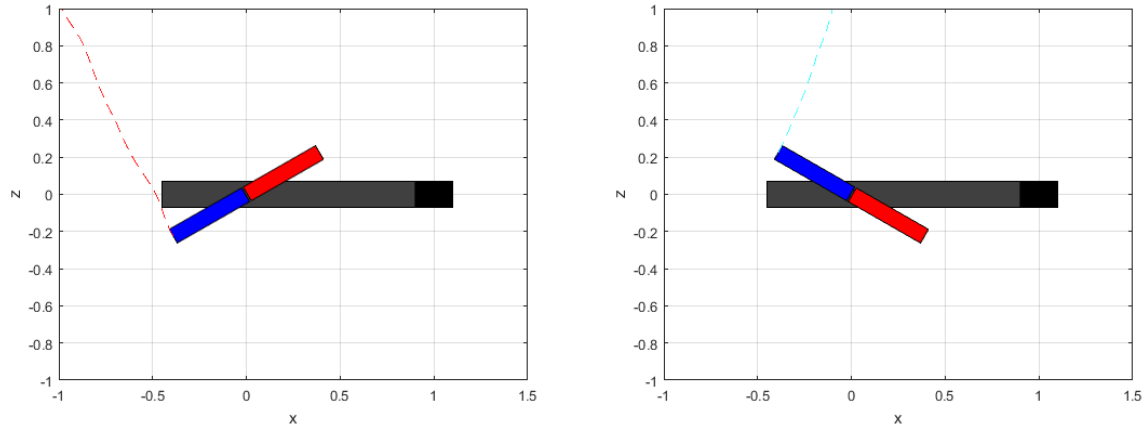

Figure 4-72 – Georgia Tech SCS trajectories at azimuth release = 150° (Left) & 210° (Right)

5 Conclusion

This thesis begins with a literature review conducted on existing ice shedding and shed ice trajectory techniques. Then, a methodology was proposed to evaluate shedding and possible trajectories. Following this, the developed frameworks were applied to test cases in hover and forward flight and the results were discussed.

The ice shedding module performed a force balance using a sectional approach to identify the shed-ice location along the blade and the shedding time. This considered the centrifugal, shear, tensile and aerodynamic forces acting on the ice piece to evaluate shedding. The module was validated with an experimental test case in hover conducted at Penn. State. Following this, the ice shedding technique was applied to the Georgia Tech case, a forward flight case, to demonstrate its ability to work successfully during various helicopter manoeuvres. The material properties and blade parameters are an input to the code and therefore is capable of simulating blades of various materials and designs.

The trajectory component simulated possible trajectories based on size, shape and release location of the ice piece. It was decided that an analysis of possible impact zones based on azimuth release points was preferred instead of one trajectory based on the calculated shedding time of the ice piece, as a small off-prediction in shedding time would lead to a significantly different trajectory. A 6-DOF model that simulated linear and angular motion of the ice piece was implemented. This used three forces and three moments acting on the ice piece at every iteration, together with the integration of the Newton and Euler equations to compute the resulting motion. The implementation of this was verified against several test cases. The shed-ice piece was modelled as a rectangular plate and a semi-circular shell. Their aerodynamic properties were validated against experimental and other numerical results. The code is developed such that other shape databases can easily be used. Like the ice shedding module, ice trajectories were effectively evaluated in hover and forward flight to demonstrate the versatility of the developed code.

Several advancements can be added to the ice shedding and trajectory modules. Effects due to blade motions is not considered in the current ice shedding model. The complex motions

of the blade which include flutter, cyclic pitch change, lead-lag motions could have an impact on the shedding time and location. Understanding these can help better predict shedding location and times. Ice is generally not allowed to accumulate until it naturally sheds in real life helicopters. Ice Protection Systems (IPS) are activated as soon as ice formation is detected. Hence, including a heat transfer module that can conduct heat transfer analysis between the IPS and accreted ice, and predict the resulting shed ice geometry and time can be extremely beneficial to IPS and helicopter manufacturers. This thesis only looked at a conventional helicopter configuration with one rotor. The ice shedding module can be applied to other configurations including tilt rotors, tandem helicopters and side by side rotors to predict ice shedding.

Currently the ice trajectory module consists of two aerodynamic characteristics databases. The databases of several other shapes can be added, and it would be interesting to develop a parametrization technique based on ice shape. Therefore, parametrizing the shapes such that the aerodynamics of a random ice shape can be quickly constructed based on data of existing shapes. This would avoid the need to create a database for every new shape investigated and it would provide more accurate trajectory paths. The ice trajectory module developed in this thesis is a one-way interaction between the ice piece and the flow field. Hence, only the flow field affects the trajectory, but the ice piece does not affect the flow field. It would be interesting to implement a two-way interaction of the flow field and shed-ice to investigate the impact of the ice shape on the flow field and the resulting trajectory. Although this can be extremely computationally intensive, it would serve as validation, as there are no detailed experimental trajectories conducted. Since this method would require a lot of computational resources, Reduced Order Modelling can be used to map a spectrum of possible impact zones based on a few trajectories. Lastly, other configurations involving multiple rotors can be analysed where the flow fields are more complex and consists of the possibility of shed-ice from one rotor traversing to hit another rotor.

As mentioned before, icing studies on helicopters are relatively recent. Hence, experimental data exist for certain applications but not for others such as trajectories. Icing codes are being developed at a fast pace and we are capable of computing 3-D rotor flow fields now.

The ultimate goal is to be able to compute 3-D rotor flow, drop and ice accretion, while considering blade motion and analysing for ice shedding, trajectories and heat transfer in a fully-coupled fashion.

6 References

[1] J. Martin, “The Adverse Aerodynamic Effects of Inflight Icing on Airplane Operation”, TP 185 - Aviation Safety Letter, 2009.

[2] E. W. Brouwers, “The Experimental Investigation of a Rotor Icing Model With Shedding”, Thesis, Pennsylvania State University, 2010.

[3] S. Zhang, “FEM Analysis of In-flight Ice Break-up”, Master Thesis, McGill University, 2012.

[4] L. Bennani, P.Villedieu and M. Salaun, “Two-Dimensional Model of an Electro-Thermal Ice Protection System”, in 5th AIAA Atmospheric and Space Environments Conference, San Diego, 2013, AIAA Paper 2013-2936.

[5] R. J. Scavuzzo, M. L. Chu and C. J. Kellackey, “Impact Ice Stresses in Rotating Airfoils”, AIAA Journal of Aircraft, vol. 28, no. 7, pp. 450-455, 1990.

[6] E. W. Brouwers, J. L. Palacio and E. C. Smith, “The Experimental Investigation of a Rotor Icing Model With Shedding”, Thesis, Pennsylvania State University, 2010.

[7] R. J. Scavuzzo, M. L. Chu and V. Ananthaswamy, “Influence of Aerodynamic Forces in Ice Shedding”, AIAA Journal of Aircraft, vol. 31, no. 3, pp. 526-530, 1994.

[8] H. Beaugendre, F. Morency, F. Gallizio and S. Laurens, “Computation of Ice Shedding Trajectories Using Cartesian Grids, Penalization, and Level Sets”, Modelling and Simulation in Engineering, Vols. 2011, Article ID 274947, 15 pages, 2011.

[9] G. S. Baruzzi, P. Lagacé, M. S. Aubé and W. G. Habashi, “Development of a Shed-Ice Trajectory Simulation in FENSAP-ICE”, SAE Aircraft and Engine Icing International Conference, Seville, Spain, 2007, SAE Technical Paper 2007-01-3360.

[10] N. Minhas and R. Khurram, “Ice Breakup, Shedding, and Impact Analysis for Helicopters”, in 39th European Rotorcraft Forum, Session: Aerodynamics, Moscow, pp. erf2013_040, 2013.

[11] H. Fouladi, “Computational Methods for Rotorcraft Icing”, PhD Thesis, McGill University, 2015.

[12] R. Yapalparvi, H. Beaugendre and F. Morency, “Calculation of Ice Chunk Trajectory Using Proper Orthogonal Decomposition”, in 4th AIAA Atmospheric and Space Environments Conference, New Orleans, 2012, AIAA Paper 2012-2676.

[13] D. L. Kohlman and R. C. Winn, “Analytical prediction of trajectories of ice pieces after release in an airstream”, 39th Aerospace Sciences Meeting, Reno, 2001, AIAA Paper 2001-0680.

[14] L. C. C. Santos, R. Papa and M. A. S. Ferrari, “A simulation model for ice impact risk evaluation”, 41st Aerospace Sciences Meeting, Reno, 2001, AIAA Paper 2003-30.

[15] M. Papadakis, H. Yeong and I. Suares, “Experimental and Computational Investigation of Ice Shedding from Aircraft Surfaces”, 44th AIAA Aerospace Sciences Meeting, Reno, 2001, AIAA Paper 2006-1010.

[16] D. Kelly, “Aerodynamics and Multibody Dynamics of Helicopter Rotors in Icing Conditions”, Master Thesis, McGill University, 2016.

[17] Y. Bourgault, W. G. Habashi, J. Dompierre and G. S. Baruzzi, “A finite element method study of Eulerian droplets impingement models”, International Journal for Numerical Methods in Fluids, vol. 29, no. 4, pp. 429-449, 1999.

[18] Y. Bourgault, H. Beaugendre and W. G. Habashi, “Development of a Shallow-Water Icing Model in FENSAP-ICE”, AIAA Journal of Aircraft, vol. 37, no. 4, pp. 640-646, 2000.

[19] H. Beaugendre, F. Morency and W. G. Habashi, “FENSAP-ICE’s Three-Dimensional In-Flight Ice Accretion Module: ICE3D”, AIAA Journal of Aircraft, vol. 40, no. 2, pp. 239-247, 2003.

[20] M. Nathoo, W. G. Habashi and M. Fossati, “Stitching and Deformation of Non-overlapping Meshes for Unsteady Rotorcraft Aerodynamics”, 55th AIAA Aerospace Sciences Meeting, Grapevine, 2017, AIAA Paper 2017-0582.

[21] X. Xian, L. Chu, R. Scavuzzo and S. Srivatsan, “An experimental evaluation of the tensile strength of impact ice”, Journal of Materials Science Letters, Vols. 1205-1208, no. 10, p. 8, October 1989.

[22] G. Fortin and J. Perron, “Ice Adhesion Models to Predict Shear Stress at Shedding”, Journal of Adhesion Science and Technology, vol. 26, no. 4-5, pp. 523-553, 2012.

[23] M. Papadakis, H. Yeong and I. Suares, “Experimental and Computational Investigation of Ice Shedding from Aircraft Surfaces”, 44th AIAA Aerospace Sciences Meeting, Reno, 2001 AIAA Paper 2006-1010.

[24] Z. Zhan, “Towards Real-Time CFD Simulation of In-Flight Icing”, PhD Thesis, McGill University, 2016.

[25] D. N. Mavris, N. M. Komerath and H. M. McMahon, “Prediction of Aerodynamic Rotor-Airframe Interactions in Forward Flight”, Journal of the American Helicopter Society, vol. 34, no. 4, pp. 37-46, 1989.

[26] M. Nathoo, “Mesh Stitching and Deformation for Helicopter Rotor Icing”, Master Thesis, McGill University, 2018.

[27] S. Murman, M. Aftomis and M. Berger, “Simulations of 6-DOF with a Cartesian Mesh”, 41st Aerospace Sciences Meeting, Reno, 2003, AIAA Paper 2003-1246.

7 Appendix

7.1 Appendix A – Runge-Kutta integration for a system of equations

$$\dot{P}^b = \frac{M_x^b}{I_{xx}} + \left(I_{yy} - I_{zz}\right)Q^b R^b \rightarrow e(t, P^b, Q^b, R^b)$$

$$\dot{Q}^b = \frac{M_y^b}{I_{yy}} + (I_{zz} - I_{xx})R^b P^b \rightarrow f(t, P^b, Q^b, R^b)$$

$$\dot{R}^b = \frac{M_z^b}{I_{zz}} + \left(I_{xx} - I_{yy}\right)P^b Q^b \rightarrow g(t, P^b, Q^b, R^b)$$

4-stage Runge-Kutta

$$j_1 = \Delta t \cdot e\left(t_n, P_n^b, Q_n^b, R_n^b\right)$$
$$k_1 = \Delta t \cdot f(t_n, P_n^b, Q_n^b, R_n^b)$$
$$l_1 = \Delta t \cdot g(t_n, P_n^b, Q_n^b, R_n^b)$$

$$j_2 = \Delta t \cdot e(t_n + \frac{\Delta t}{2}, P_n^b + \frac{j_1}{2}, Q_n^b + \frac{k_1}{2}, R_n^b + \frac{l_1}{2})$$
$$k_2 = \Delta t \cdot f(t_n + \frac{\Delta t}{2}, P_n^b + \frac{j_1}{2}, Q_n^b + \frac{k_1}{2}, R_n^b + \frac{l_1}{2})$$
$$l_2 = \Delta t \cdot g(t_n + \frac{\Delta t}{2}, P_n^b + \frac{j_1}{2}, Q_n^b + \frac{k_1}{2}, R_n^b + \frac{l_1}{2})$$

$$j_3 = \Delta t \cdot e(t_n + \frac{\Delta t}{2}, P_n^b + \frac{j_2}{2}, Q_n^b + \frac{k_2}{2}, R_n^b + \frac{l_2}{2})$$
$$k_3 = \Delta t \cdot f(t_n + \frac{\Delta t}{2}, P_n^b + \frac{j_2}{2}, Q_n^b + \frac{k_2}{2}, R_n^b + \frac{l_2}{2})$$
$$l_3 = \Delta t \cdot g(t_n + \frac{\Delta t}{2}, P_n^b + \frac{j_2}{2}, Q_n^b + \frac{k_2}{2}, R_n^b + \frac{l_2}{2})$$

$$j_4 = \Delta t \cdot e(t_n + \Delta t, P_n^b + j_3, Q_n^b + k_3, R_n^b + l_3)$$
$$k_4 = \Delta t \cdot f\left(t_n + \Delta t, P_n^b + j_3, Q_n^b + k_3, R_n^b + l_3\right)$$
$$l_4 = \Delta t \cdot g(t_n + \Delta t, P_n^b + j_3, Q_n^b + k_3, R_n^b + l_3)$$

$$j = \frac{1}{6}(j_1 + 2j_2 + 2j_3 + j_4)$$

$$k = \frac{1}{6}(k_1 + 2k_2 + 2k + k_4)$$

$$l = \frac{1}{6}(l_1 + 2l_2 + 2l_3 + l_4)$$

$$P_{n+1}^{b} = P_n^{b} + j$$

$$Q_{n+1}^{b} = Q_n^{b} + k$$

$$R_{n+1}^{b} = R_n^{b} + l$$

7.2 Appendix B – Rectangular plate Aerodynamic Database

Figure 7-1 to Figure 7-3 illustrate the variation of the three force coefficients and the three moment coefficients with angle of attack at various side slip angles for a rectangular plate. FENSAP simulations were conducted at angle of attack intervals of 5° and side slip angle intervals of 30°.

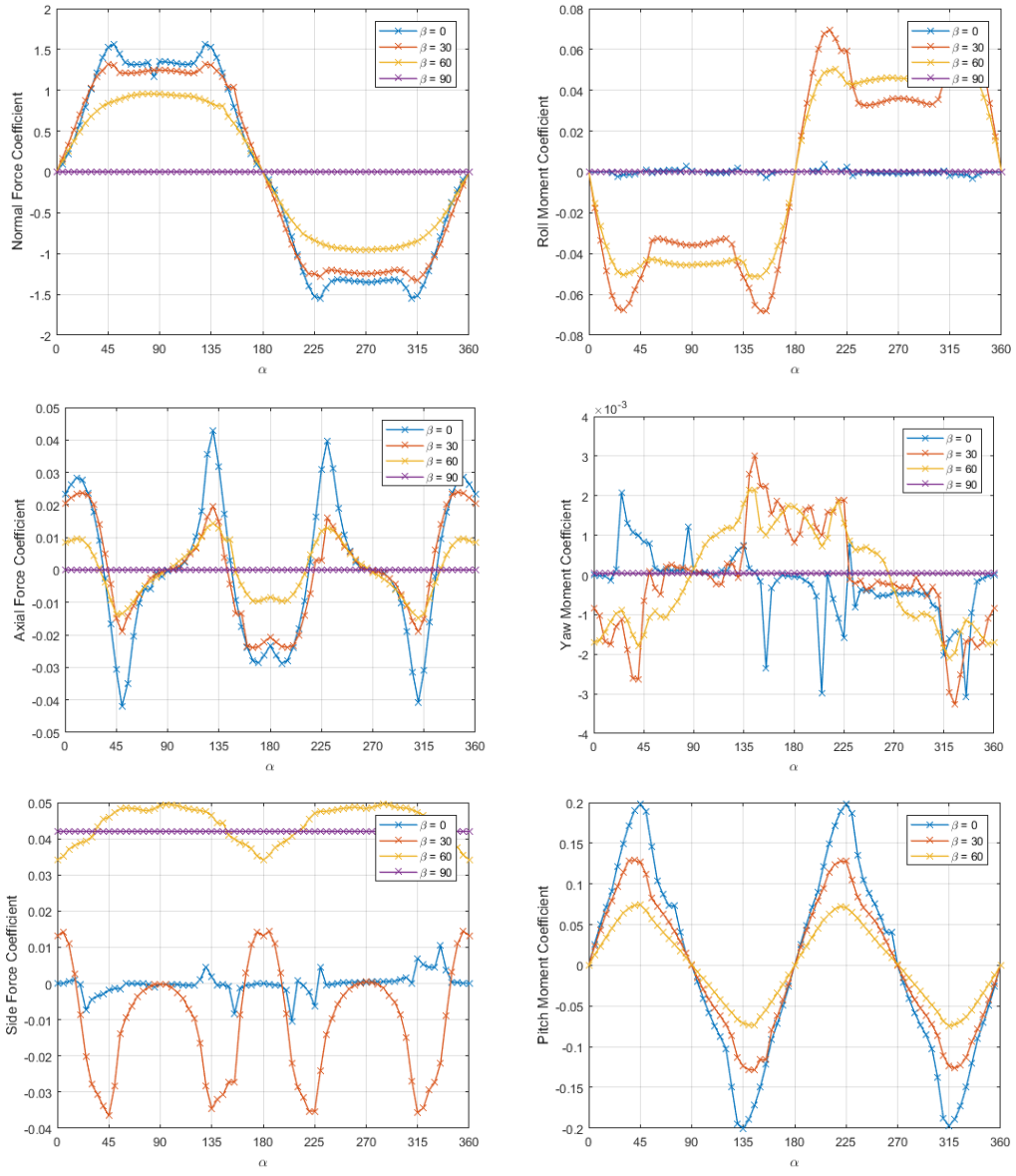

Figure 7-1 – Rectangular plate aerodynamic properties – (Top left) Normal Force Coefficient, (Top right) Roll Moment Coefficient, (Middle left) Axial Force Coefficient, (Middle right) Yaw Moment Coefficient, (Bottom left) Side Force Coefficient, (Bottom right) Pitch Moment Coefficient vs Angle of attack at Side slip angles 0°, 30°, 60° and 90°.

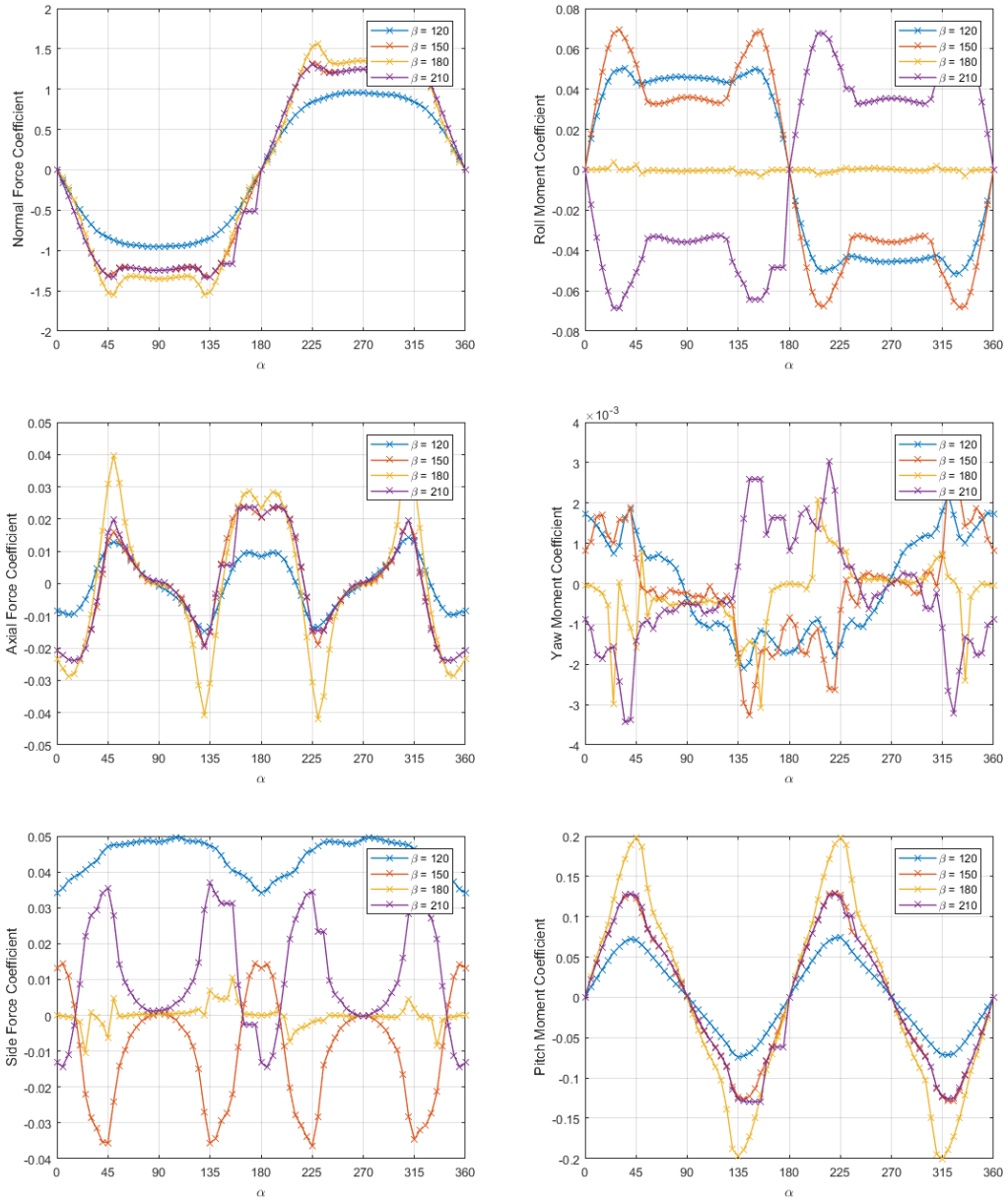

Figure 7-2 – Rectangular plate aerodynamic properties – (Top left) Normal Force Coefficient, (Top right) Roll Moment Coefficient, (Middle left) Axial Force Coefficient, (Middle right) Yaw Moment Coefficient, (Bottom left) Side Force Coefficient, (Bottom right) Pitch Moment Coefficient vs Angle of attack at Side slip angles 120°, 150°, 180° and 210°.

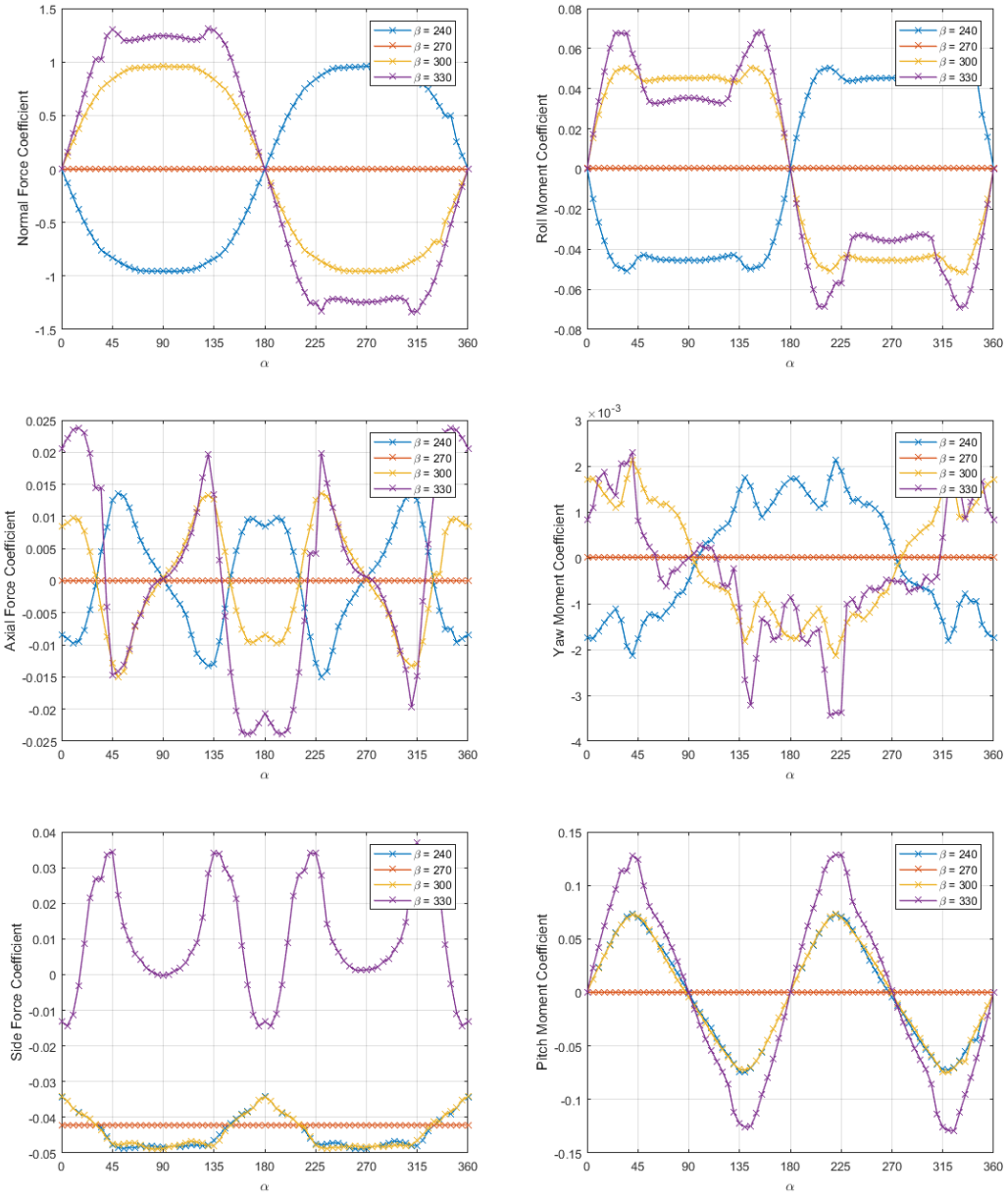

Figure 7-3 – Rectangular plate aerodynamic properties – (Top left) Normal Force Coefficient, (Top right) Roll Moment Coefficient, (Middle left) Axial Force Coefficient, (Middle right) Yaw Moment Coefficient, (Bottom left) Side Force Coefficient, (Bottom right) Pitch Moment Coefficient vs Angle of attack at Side slip angles 240°, 270°, 300° and 330°.

7.3 Appendix C – Semi Circular Shell Aerodynamic Database

Figure 7-4 to Figure 7-6 illustrate the variation of the three force coefficients and the three moment coefficients with angle of attack at various side slip angles for a rectangular plate. FENSAP simulations were conducted at angle of attack intervals of 5° and side slip angle intervals of 30°.

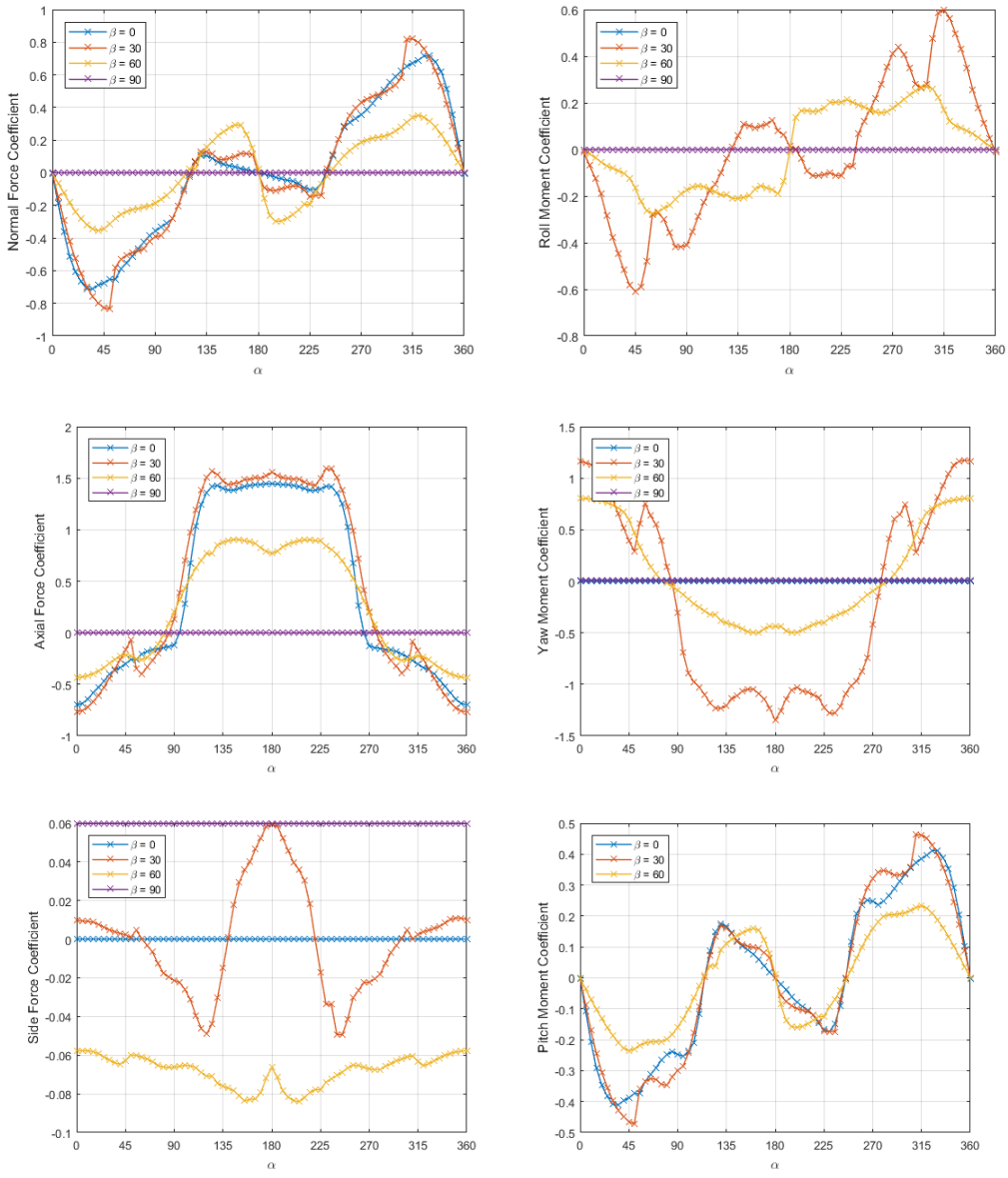

Figure 7-4 – Semi Circular Shell aerodynamic properties – (Top left) Normal Force Coefficient, (Top right) Roll Moment Coefficient, (Middle left) Axial Force Coefficient, (Middle right) Yaw Moment Coefficient, (Bottom left) Side Force Coefficient, (Bottom right) Pitch Moment Coefficient vs Angle of attack at Side slip angles 0°, 30°, 60° and 90°.

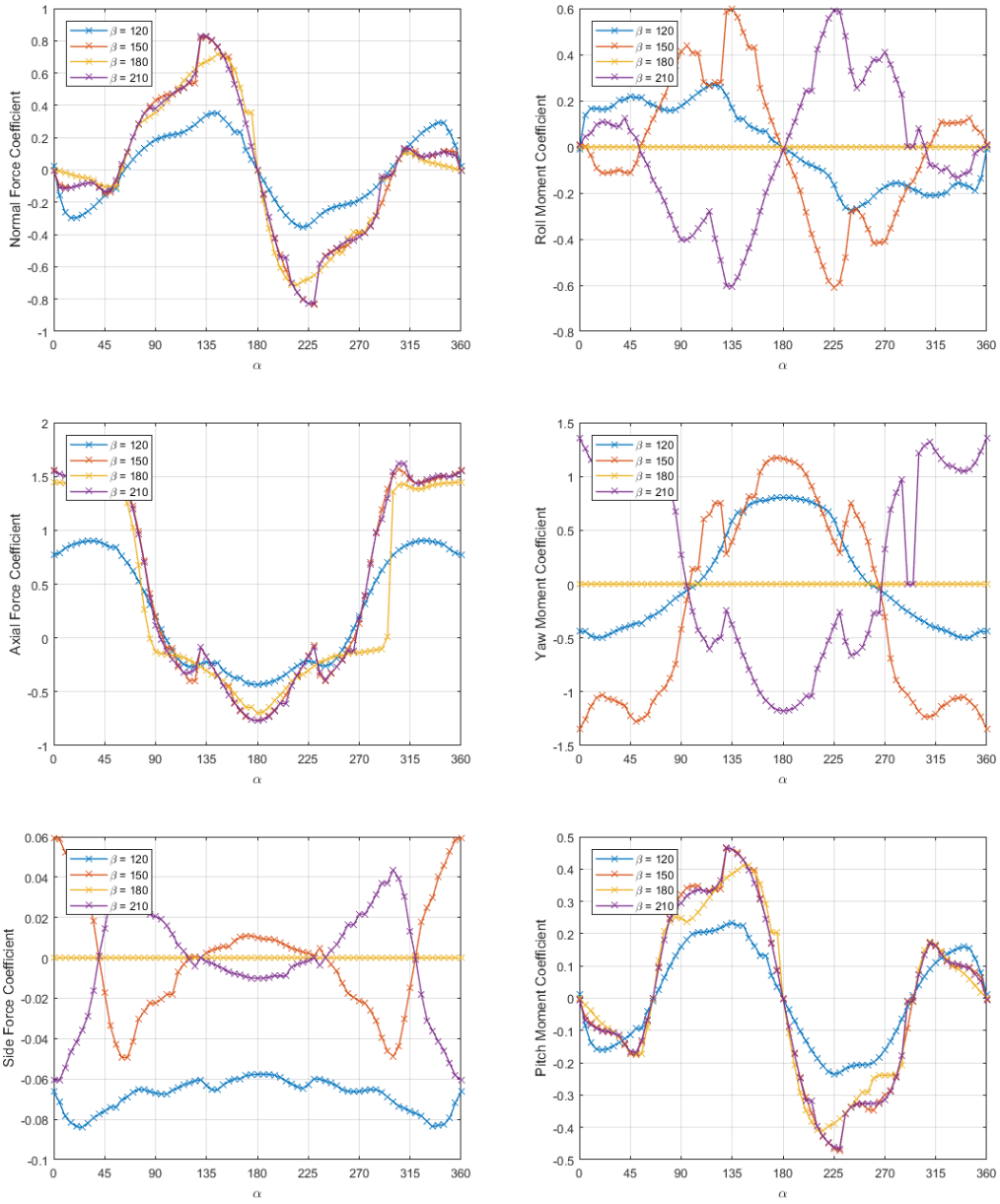

Figure 7-5 – Semi Circular Shell aerodynamic properties – (Top left) Normal Force Coefficient, (Top right) Roll Moment Coefficient, (Middle left) Axial Force Coefficient, (Middle right) Yaw Moment Coefficient, (Bottom left) Side Force Coefficient, (Bottom right) Pitch Moment Coefficient vs Angle of attack at Side slip angles 120°, 150°, 180° and 210°.

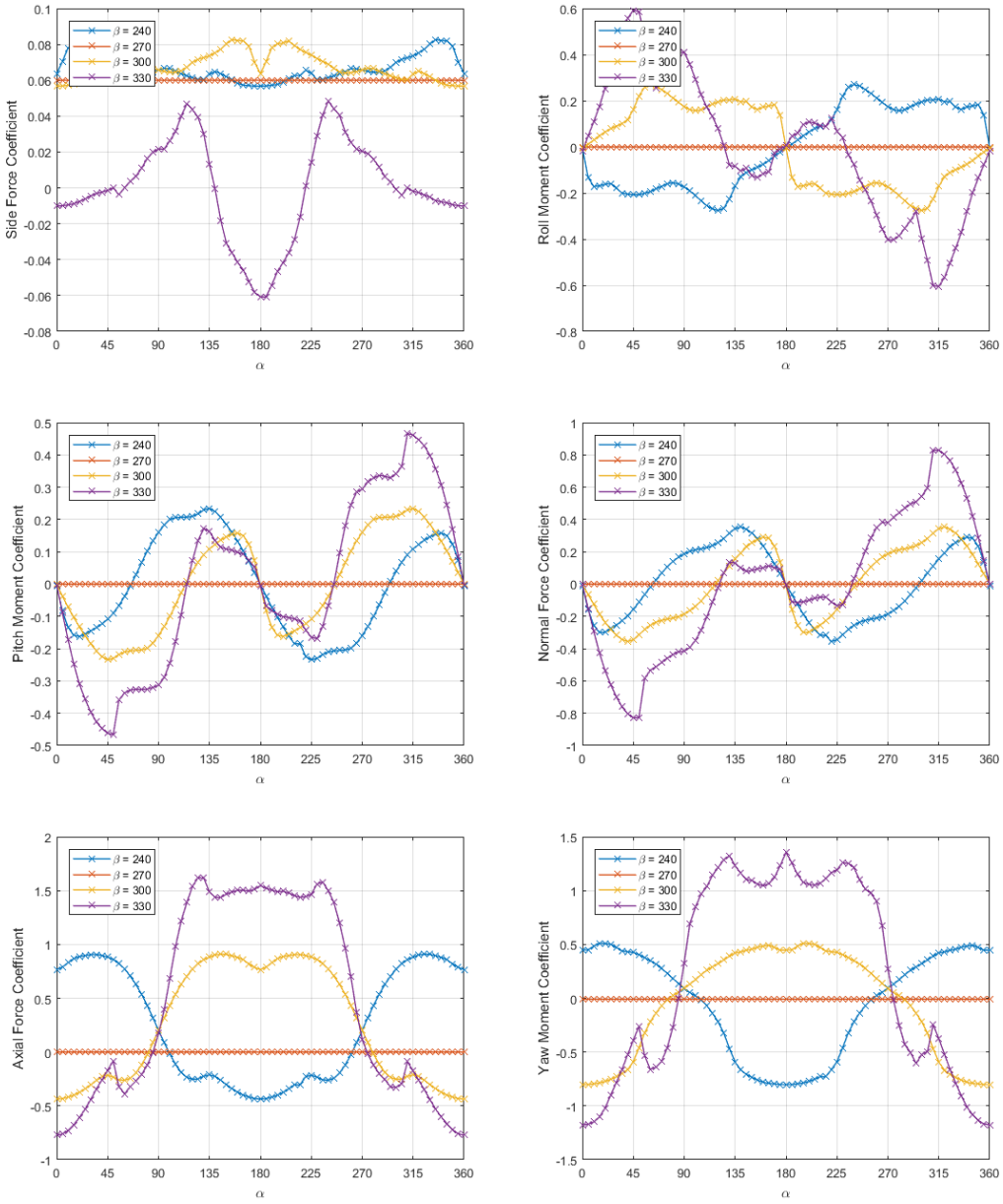

Figure 7-6 – Semi Circular Shell aerodynamic properties – (Top left) Normal Force Coefficient, (Top right) Roll Moment Coefficient, (Middle left) Axial Force Coefficient, (Middle right) Yaw Moment Coefficient, (Bottom left) Side Force Coefficient, (Bottom right) Pitch Moment Coefficient vs Angle of attack at Side slip angles 240°, 270°, 300° and 330°.